FACULTY OF SCIENCE
UNIVERSITY OF COPENHAGEN

MASTER'S THESIS
60 ECTS

Continuous Flow and Discrete Measurements of the Water Isotopes in an Firn Core from Greenland

Yongbiao Weng

Centre for Ice and Climate
Niels Bohr Institute
Faculty of Science
University of Copenhagen

Supervisor:
Bo Møllesøe Vinther
Trevor James Popp
Centre for Ice and Climate,
University of Copenhagen

Submitted: 1st June 2014

Abstract

This thesis presents discrete and continuous flow measurements of the water isotopes in a firn core from Northeast Greenland Ice Stream (NEGIS). Discrete samples are cut with a 5 cm resolution, and the continuous flow is obtained with an approximate 5 mm resolution by continuous melting the firn core. Samples are measured with Infra-Red Cavity Ring-Down spectroscopy. Techniques of each type of measurement are described, including the different calibration procedures leading to the final results. For the data processing of the continuous flow measurements, semi-automatic methods of extracting the useful isotope signal and generating the depth scale are required and developed.

The results from continuous flow measurements have been compared to the discrete samples. Comparison shows an overall agreement and an comparable precision level of both measurements, which indicates a good reliability of the continuous flow measurements. Given that the continuous measurements have both high measuring speed and high resolution, this approach has great potential. The results also indicate a reliable long term stability of the analytical system, considering only two times of calibration have been performed for the whole continuous measurements of 28 days. A small remaining deviation compared to the discrete measurements may still due to slight instrumental drifts though.

The high resolution obtained by the continuous flow approach can be useful for reconstructions of climate change in the past. However, the diffusion imposed both in the snow and firn layers of the ice sheet and during the measurements limits the available resolution. In the last part of the thesis, the study of a firn diffusion model developed by Johnsen (1977, 2000) is carried out to address the diffusion process in the NEGIS firn core.

Resumé

Dette speciale præsenterer både diskrete og kontinuærte målinger af vandets isotop-indhold i en firn-kerne boret i Northeast Greenland Ice Stream (NEGIS). De diskrete prøver er skåret i 5 cm opløsning mens de kontinuerte målinger har en opløsning på ca. 5 mm. Disse målinger udføres ved kontinuert at smelte firn kernen. Prøverne er målt vha. Infra-rød kavitets afringnings spektroskopi. Tekninken bagved begge typer af malinger er beskrevet, herunder de forskellige kalibreings rutiner, der leder til de endelige resultater. For data-processeringen af de kontinuerte målinger har det været nødvendigt at udvikle en semi-automatisk metode til at ekstrahere brugbare isotop-signaler på en dybde-skala.

Resultaterne baseret på de kontinuerte målinger er blevet sammenlignet med de diskrete målinger. Sammenligningen viser en generelt god overensstemmelse og sammenlignelig præcision for de to målinger, hvilket indikere en god pålidelighed for de kontinuerte målinger. Da de kontinuerte målinger både er hurtige at lave og er i høj opløsning, så har denne metode et stort potentiale. Resultaterne indikerer også en pålidelig stabilitet over lange tidsrum, idet kun to gange kalibreringer er blevet udført på 28 dage. Der er dog stadig mindre tilbageværende afvigelser sammenlignet med de diskrete data. Disse afvigelse kan stadig skyldes instrument-drift.

Den høje opløsning, som kan opnås vha. den kontinuerte målemetode kan være en hjælp for rekonstruktioner af fortidens klima. Den diffusion, som der sker i sneen of firnen på iskappen, samt den diffusion der sker i selve målingen sætter imidlertid grænser for opløsningen. I den sidste del af specialet studeres en firn-diffusion model udviklet af Johnsen (1977, 2000) for at adressere diffusions-processerne i NEGIS firn-kernen.

Contents

Acknowledgements

It has been a luck in my life to have come across Denmark. I really enjoyed the studying atmosphere here. I have learned a lot in the past two years. I would first like to thank my supervisor Bo Møllesøe Vinther, who has explained me so many questions. He has ideas that make complicated things easy to understand. And his patience and easy-going style always make me feel free to ask any tiny questions. I am grateful that he has helped me plan my thesis structures and "pushed" me forward to the deadline. Thanks to him, we have also enjoyed trips and dinners in our isotope group and we always had fun. I would like to thank Trevor James Popp being my co-supervisor. He has instructed me a lot at the thesis beginning. He and Anne-Katrine have introduced me to the isotope lab and helped me to integrate into this group. Vasileios has guided me a lot since this thesis is related to his phD work. He is a specialist on water isotope, both technically and theoretically. I can always get good ideas from him.

And I will thank all the CIC members to make it such an amazing place to study. I thank for Paul to show me the CFA lab and make fun outside the study time, and Anders for caring my work and answering my questions. All the master students that we have shared the same ceiling and discussed our everyday topics, especially thanks to Iben and Maria for being accompany at the hard-working weekends.

Chapter 1

Introduction

Climate change has become a major environmental problem that faces human society today. The climate system is complex. A wise approach to better understand the climate system is to study the climate history. Fortunately, the past climate variabilities have been recorded in many natural archives (ocean and lake sediments, tree rings, fossil pollens, stalagmites, and corals, etc). By retrieving the past climate records from the natural archives, we can gain knowledge of climate change mechanisms and have more confidence to predict the climate change in the future.

Firn/Ice cores

As snow accumulates on polar and alpine ice caps and ice sheets, it lays down a record of the environmental conditions at the time of its deposition. Information concerning these paleoclimate conditions can be extracted from firn/ice cores drilled through the ice sheets and ice caps. The firn/ice core records stand out among other records as having the following advantages: high stratigraphical integrity; high temporal resolution; the only direct sequence of atmospherically deposited chemical substances (Andersen et al. 2001).

As the second largest ice sheet in the world and the largest in the Northern Hemisphere, the Greenland ice sheet plays an important role in the global climate system. Great attention has been drawn to Greenland and several valuable deep ice cores have been drilled in the last half century (Johnsen et al. 1972; Dansgaard et al. 1982; GRIP members 1993; Dansgaard et al. 1993; Grootes and Stuiver 1993; NGRIP members 2004; NEEM members 2013). The deep ice core projects that have been carried out in Greenland are listed in Table 1.1. Their locations are shown in Figure 1.1. The Greenland deep ice core records can reflect climate changes that affected the whole Northern Hemisphere and have revealed in high detail the abrupt climate changes (24 D/O cycles registered by Dansgaard et al. (1993)) during the last glacial period.

Numerous firn cores and shallow ice cores have also been drilled in Greenland (Langway et al. 1985; Clausen et al. 1988; Clausen and Hammer 1988). They are usually drilled for three aims: to select scientifically favorable site for drilling a deep ice core; to gain better understanding of the structure and composition of the ice sheet to improve the

Table 1.1: Deep ice cores that have been drilled in Greenland ice sheet.

Ice core	Year	Depth [m]
Camp Century	1963-1966	1390
Dye3	1979-1981	2035
GRIP	1989-1992	3029
GISP2	1989-1993	3053
NGRIP	1996-2004	3090
NEEM	2008-2012	2540

interpretation of the deep ice core; and to reveal a short time scale climate history.

The majority of Greenland deep ice cores have been drilled along the central ice divide, with the aim of accessing the oldest ice record of the climate, whereas there have been few ice core-based studies of Northeast Greenland due to the inaccessibility and more complex ice dynamics.

Northeast Greenland Ice Stream (NEGIS)

The Northeast Greenland Ice Stream (NEGIS) is the largest ice stream in Greenland and it is the only ice stream that extends far inland (Fahnestock et al. 1993, 2001; Joughin et al. 2001). It was first identified in 1993 using synthetic aperture radar (SAR) imagery (Fahnestock et al. 1993). The onset of the streaming flow is at the central ice divide, and the ice stream terminates in three large outlet glaciers. The location and structure of NEGIS is shown in Figure 1.1. The onset of the ice stream on the ice divide is likely caused by strong basal melt due to regionally high geothermal flux (Fahnestock et al. 2001; Petrunin et al. 2013).

NEGIS has principle importance for studying the mass balance of the Greenland ice sheet. The Greenland mass loss is accelerating, and about 50% of the net loss has been attributed to increased ice stream discharge (van den Broeke et al. 2009). Due to its great inland extent, NEGIS may also facilitate the rapid inland respond to ocean-induced coastal thinning. Therefore, to better understand the mechanisms governing the ice stream discharge and to better estimate its climate response, a focused study of NEGIS becomes essential.

As an action to approach the above purpose, a 67 m firn core (NEGIS firn core) was drilled in the summer of 2012. The drilling site is approximately 150 km downstream from the onset of the stream flow (75°37.61′ N, 35°56.49′ W). A detailed study of both geophysical and glaciochemical data from NEGIS has been presented in Vallelonga et al. (2014). This thesis will focus on the study of water stable isotope data from the NEGIS firn core.

Water stable isotopes

The climate indicator from ice cores most commonly referred to is without doubt the δ^{18}O signal. The δ^{18}O signal has long been known as a temperature proxy that reflects the

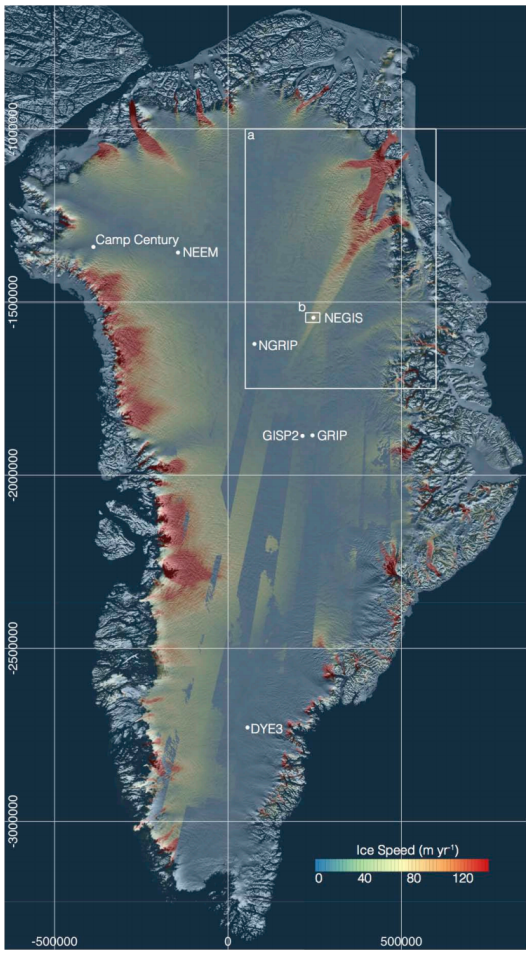

Figure 1.1: Locations of Greenland ice core drilling sites and the Northeast Greenland Ice Stream (NEGIS). Velocities from interferometric synthetic aperture radar data are shown in color (Joughin et al. 2010). Projection is polar stereographic relative to WGS84 ellipsoid with central meridian at 45°W and standard parallel at 70°N. (Figure from Vallelonga et al. (2014)).

cloud temperature at which the local precipitation forms (Dansgaard 1953, 1954, 1964). The basis for this interpretation is related to the physical properties of the oxygen and hydrogen isotopes.

Naturally occurring oxygen has three stable isotopes: ^{16}O (natural abundance 99.759%), ^{17}O (0.037%), and ^{18}O (0.204%). Naturally occurring hydrogen also has three isotopes: ^{1}H (99.985%), ^{2}H or D (0.015%), and ^{3}H or T (radioactive). The vast majority of water molecules in the nature is $H_2{}^{16}O$, with $H_2{}^{18}O$ and $HD^{16}O$ being the two forms next in line. Both $H_2{}^{18}O$ and $HD^{16}O$ molecules are heavier than the standard $H_2{}^{16}O$ molecules. Molecules with heavier isotopes are more stable due to the higher dissociation energy that is required to break the hydrogen bond between the molecules (Clark and Fritz 1997), e.g. more energy is needed to break the D-H bond than the H-H bond. It results in the

fact that the volatility of $H_2{}^{16}O$ is higher than those of the heavy isotopic components. This causes fractionation in each evaporation and condensation process, that is to say, compared to $H_2{}^{16}O$ the heavier water molecules evaporate slower from a water surface and form precipitation faster from a cloud.

During the poleward transportation of water vapor, such isotope fractionation continues this preferential removal of the heavier isotope, leaving the water vapor increasingly depleted in $H_2{}^{18}O$ and $HD^{16}O$. Because condensation is the result of cooling, the greater the fall in temperature, the lower the heavy isotope concentration will be. Isotope concentration in the condensate can thus be considered as a function of the temperature at which condensation occurs. For instance, during cold conditions (e.g. during winter or in a cold climatic period), the air masses that arrive in Greenland have cooled more on the way, i.e. have formed more precipitation, thereby the remaining vapor is more depleted in heavy isotopes (corresponding to lower $\delta^{18}O$ values). Such a rain-out process is illustrated in Figure 1.2.

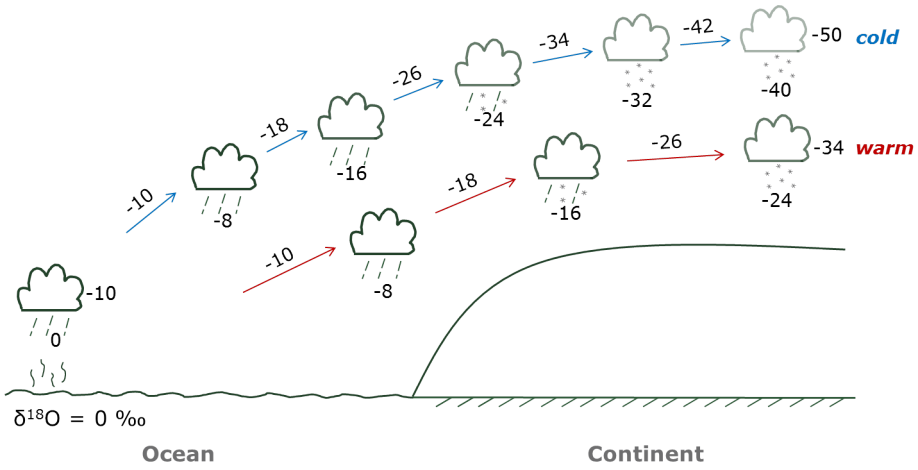

Figure 1.2: The rain-out processes for the water vapor that arrive in Greenland, in cold and warm conditions, respectively. The depletion of ^{18}O is given as $\delta^{18}O$ values of the cloud and precipitation. The amount of water that has rained out of the cloud is illustrated by the number of times that precipitation forms on the way. Fractionation plays a role at each time the precipitation forms, thus the remaining vapor in the cloud becomes more depleted. In cold conditions, more precipitation forms due to the lower temperature, thus the final deposited precipitation has a lower $\delta^{18}O$ value compared to that in the warm conditions.

Therefore the heavy isotope concentration in the precipitation deposited on the Greenland ice sheet can be used as a proxy for Greenland temperature, provided the water vapor evaporated from the source has a constant heavy isotope concentration all the time. This assumption is likely to be supported as the subtropical part of the North Atlantic Ocean is suggested to be the dominating moisture source for the Greenland precipitation (Johnsen et al. 1989).

The heavy isotope concentration is usually a very small number, and its absolute value is difficult to measure. Take $H_2{}^{18}O$ as an example, there is only 2‰ $H_2{}^{18}O$ in natural water, and in Arctic precipitation the amount of $H_2{}^{18}O$ is reduced by about 40‰ out of the 2‰. Thus the differences of the heavy isotope concentration in the precipitation are very small. To improve accuracy and to obtain convenient numerical values, the isotopic measurements are usually expressed in terms of the δ values, which is defined as:

$$\delta = \frac{R_{sample} - R_{standard}}{R_{standard}} \cdot 1000‰,$$

where R_{sample} and $R_{standard}$ are the ratios of the heavy molecules ($H_2{}^{18}O$ or $HD^{16}O$) relative to the light molecules ($H_2{}^{16}O$) for the measured sample and the standard, respectively; and δ represents the deviation of the R_{sample} to the $R_{standard}$. The standard water is referred to the Vienna Standard Mean Ocean Water (VSMOW) defined by the International Atomic Energy Agency (IAEA).

Measuring isotopic ratios

The isotopic concentration ratios (R_{sample}) can be measured either according to the mass differences or the spectral properties of the isotopologues. One typical and traditional method is to perform the discrete samples via an Isotope Ratio Mass Spectrometer (IRMS). While high precision and accuracy can be achieved with this method, the samples preparation and measuring remains an elaborate process. For instance, an 2-3 km long ice core can yield tens of thousands of samples and requires several years to complete the measurements.

Besides, with the IRMS method, water molecules need to be converted to a different gas prior to the measurement, e.g. CO_2 equilibration method for $\delta^{18}O$ analysis (Epstein 1953) and reduction of water to hydrogen gas for δD analysis (Bigeleisen et al. 1952; Gehre et al. 1996). As a result, the isotopic concentration ratios of $^{18}O/^{16}O$ and $D/^1H$ are not simultaneously analyzed. Improvements have been made to pyrolyze the water molecules to CO and H_2 instead (Begley and Scrimgeour 1997; Gehre et al. 2004), but still in a discrete and indirect mode.

At the same time, laser spectroscopy at the near- and mid-infrared regions had been successfully applied for the measurement of various molecules in the gas phase and the Near-Infrared Cavity Ring-Down Spectrometer (NIR-CRDS) also became commercially available (Kerstel et al. 1999; Iannone et al. 2009). A major advantage of this technique is the ability to directly and simultaneously measure both $^{18}O/^{16}O$ and $D/^1H$ ratios in the optical cavity. Additionally, the Continuous Flow Analysis (CFA) has been well developed to measure the chemical impurities in the ice core in high resolution by continuously melting the ice core (Sigg et al. 1994; Kaufmann et al. 2008). A combination of these two techniques provides a great potential to improve the measurements of water isotopic concentration ratios in respect of both time-saving and resolution.

The combination of the two techniques has been applied and evaluated by Gkinis et al.

(2010, 2011), which have presented promising results. This thesis owes much to this inspiring work and will in further details continue to compare the discrete and the continuous flow measurements of the water isotope record on a new firn core from Northeastern Greenland.

Outline of the thesis

The thesis is structured in the following manner:

Chapter 2 presents the discrete measurements of the water isotopes in NEGIS firn core. The techniques of NIR-CRDS is introduced. The data of the measurements are calibrated, and the results presented and discussed.

Chapter 3 presents the continuous flow measurements of the water isotopes in NEGIS firn core. The CFA system and its coupling with CRDS system are introduced. The data processing of the raw results from continuous flow measurements has been a challenge, which includes to perform a proper VSMOW calibration, to extract the useful isotope signals, and to generate a correct depth scale. Related issues have been discussed.

Chapter 4 presents the comparisons of the two series of measurements. The precision, resolution, and the data agreement has been discussed.

Chapter 5 addresses the diffusion of the water isotopes in the NEGIS firn core based on the model introduced by Johnsen (1977, 2000). The derivation of the model has been followed through in details.

Chapter 6 presents the discussion and the main conclusions of this thesis.

The mathematical fundamentals that are closely related to this thesis are given in **Appendix A** and **B**.

Chapter 2

Discrete Measurements

2.1 Samples preparation

After the drilling in the field, the firn core was logged and stored in sections called "bags". Each bag is typically 0.55 m. The bag length can be used to construct the depth scale of the core in the later time. The firn core was longitudinally cut into five segments, as shown in Figure 2.1.

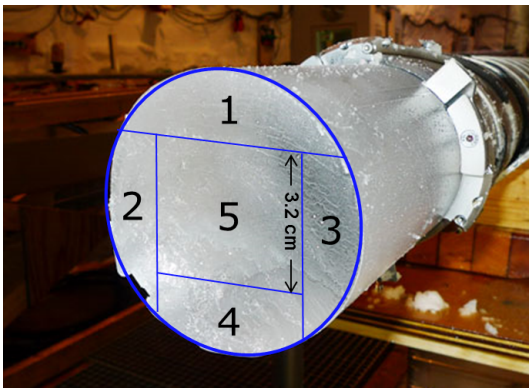

Figure 2.1: A sketch of the cutting plan for the NEGIS firn core. First, segment 1 was cut to expose a fresh ice surface that is ready to conduct ECM measurements (see Section 2.5). This was done in the field. After transported to the freezer in Copenhagen, the left main part of the core was cut into 4 longitudinal segments. The central part, segment 5, was used to conduct CFA analysis which include measurements of impurities, chemistry, and continuous water isotopes (see Section 3.1.1). Segments 2, 3 and 4 were stored in the freezer for future use. Segment 1 was cut into 5 cm samples to be used for discrete water isotope measurements. For the NEGIS shallow core, the diameter of the core is 7.4 cm. The cross section of segment 5 is a 3.2 cm×3.2 cm square surface.

The NEGIS core consists of 121 bags: 2 overlapping surface snow pistons, 0 - 0.55 m and 0.5 - 1.05 m respectively; and 119 firn core bags, 1.1 - 66.3 m. There is a 0.05 m gap in

sampling between the snow pistons and the firn core. The last firn core bag is only 0.3 m long (66.0 - 66.3 m). All the snow pistons and the firn core were measured in a resolution of 0.05 m for the discrete isotope record. Due to the very loose structure of the snow pistons and the top firn core, only bag 7 - 121 were measured for the continuous isotope record.

2.2 NIR Cavity Ring Down Spectrometer

The discrete samples were measured on a Picarro L2120-i Near-Infrared Cavity Ring-Down Spectrometer (NIR-CRDS) using the high throughput Picarro-A0212 vaporizer. The latter is superior to the more standard high precision Picarro-A0211 vaporizer regarding memory effects (Vallelonga et al. 2014).

Laser spectroscopy at the near and mid infrared regions has been demonstrated as an alternative to the traditional Isotope Ratio Mass Spectrometers (IRMS) for water isotope analysis, presenting numerous advantages (Kerstel et al. 1999, 2005, 2006; Brand et al. 2009; Gkinis et al. 2010, 2011). The basic principles of Cavity Ring-Down Spectroscopy is introduced as follows. Most small gas-phase molecules (e.g., H_2O, CO_2) have a unique near-infrared absorption spectrum due to rotational and vibrational transitions (Kerstel et al. 2005). At sub-atmospheric pressure, this consists of a series of narrow sharp lines, each at a characteristic wavelength which is well-known. The concentration of any species of interest can be detected by measuring the strength of this absorption. The resulting spectra are highly sensitive to isotopic substitution of the molecule, thus being able to permit distinction between different isotopologues. For further description on optical techniques for isotope ratio infrared spectrometry one can refer to Kerstel et al. (2005).

The experimental procedure of CRDS from Picarro Inc. (Gupta et al. 2009) as utilized for the water isotope measurements here, is briefly described as follows. A beam from a single-frequency laser diode enters a cavity with three high reflectivity mirrors. The three mirrors are set in specific angles so as to keep the reflected laser light circulating in the cavity, reaching a path length of kilometers. A fast photo detector senses the small amount of light leaking through one of the mirrors to measure the light intensity. At the very beginning when the laser is on, the cavity quickly fills with circulating laser light. It is abruptly turned off when the photo detector detects a threshold level. Then the light intensity in the cavity will exponentially decay, due to scattering, reflection, and absorption losses from the target gas molecules. This decay, or "ring down", is measured in real-time by the photo detector. A straight forward schematic of Picarro CRDS measurement is shown in Figure 2.2.

The light signal at the photo detector is given by:

$$I(t, \lambda) = I_0 e^{-\frac{t}{T(\lambda)}} \tag{2.1}$$

where I_0 is the transmitted light intensity at the time the laser is switched off and $T(\lambda)$ is the ring down time constant for a given wavelength, λ. The decay rate $R(\lambda, C)$ is proportional to the optical losses inside the cavity and is a sum of the empty-cavity decay

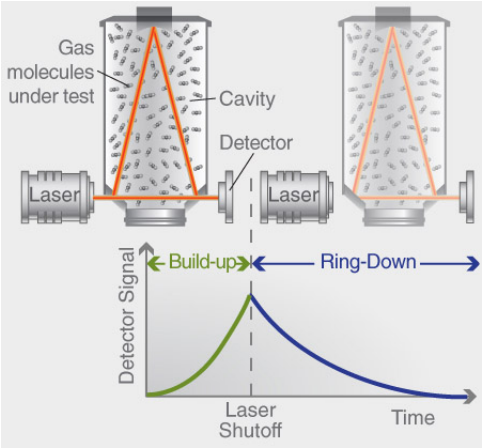

Figure 2.2: Schematic of Picarro CRDS analyzer showing how a ring down measurement is carried out (http://www.picarro.com/technology/cavity_ring_down_spectroscopy).

rate and a factor dependent on the sample absorption:

$$R(\lambda, C) = \frac{1}{T(\lambda)} = R(\lambda, 0) + c\alpha(\lambda) \tag{2.2}$$

where $R(\lambda,0) = \frac{1}{T_0(\lambda)}$ is the empty-cavity decay rate and c is the speed of light. And $\alpha(\lambda)$ is the sample absorption:

$$\alpha(\lambda) = \epsilon(\lambda)C \tag{2.3}$$

where $\epsilon(\lambda)$ is the extinction coefficient and C is the molar concentration. So the sample absorption can be obtained by taking the difference between the decay rates of an empty cavity ($C = 0$) and a cavity containing a sample:

$$\alpha(\lambda) = \frac{1}{c}\left(R(\lambda, C) - R(\lambda, 0)\right) \tag{2.4}$$

$R(\lambda, C)$ and $R(\lambda, 0)$ can be found by an exponential fit (least squares) of the "ring down" shape recorded by the photo detector. Since the sample absorption and the extinction coefficient are known, the molar concentration of the sample can be easily calculated:

$$C = \frac{\alpha(\lambda)}{\epsilon(\lambda)} \tag{2.5}$$

In this way, the absorption spectra of different isotopologues will be resolved by measuring through a series of frequencies. The change of frequency is done quickly by switching laser beams in an order of microseconds.

2.3 Measurements

The firn core and two snow pistons were sampled with a resolution of 5 cm for dual (δ^{18}O, δD) stable isotope analysis. For the overlapping part of the two snow pistons, the sample

from the deeper snow piston was analyzed. A total of 1325 samples were collected from the surface down to 66.3 m, with a 5 cm gap in sampling between snow pistons and firn core. The samples were systematically melted in dry airtight (tobacco) containers and frozen in 5 ml plastic containers. Then 1.5 ml of each melted sample was pipetted into a 2 ml vial. All samples were kept in a refrigerator to avoid evaporation between sampling and measurement. Thereafter samples were measured on Picarro L2120-i NIR-CRDS. Each measurement run consisted of three in-house standards (see Table 2.1) and other 39 discrete samples. To minimize the memory effect from the last injection, each standard was injected 12 times and only the last 5 injections were used. Each discrete sample was injected 4 times and only the last 3 injections were used.

2.4 VSMOW calibration

Results are reported with respect to VSMOW (Vienna Standard Mean Ocean Water) and normalized to the VSMOW – SLAP (Standard Light Antarctic Precipitation) scale. This is done by calibrating the values of the three in-house standards measured for each measurement run. The isotopic composition of the standards was precisely measured on traditional Isotope Ratio Mass Spectrometry (IRMS) and calibrated with respect to VSMOW. These values from IRMS are referred as the expected values ("true" values). The standards were stored in amber glass bottles with silicon sealed caps to prevent evaporation. Two of the standards ("-22" and "-40") were used to estimate a two-point calibration line between measured and expected isotope values:

$$\delta_{VSMOW} = \alpha_{dis} \cdot \delta_{measured\_dis} + \beta_{dis} \tag{2.6}$$

And the third one ("NEEM") served as a quality control. The calibration line was then applied to calibrate the measured samples from the corresponding measurement run. In this way the measured isotopic ratios are normalized to the VSMOW - SLAP scale and are able to compare with other measurements results.

Table 2.1: Values of in-house water standards reported in ‰ with respect to VSMOW - SLAP scale.

Standard	δ^{18}O	δD
-22	-21.89	-168.7
-40	-39.79	-309.8
NEEM	-33.44	-257.3
VSMOW	0.00	0.0
SLAP	-55.5	-427.5

Considering the dependence of the NIR-CRDS system on humidity levels(Gkinis et al. 2010), the water concentration was kept between 19,000 - 20,500 ppmv (parts per million

by volume) during the measurement. The precision of the system is estimated by looking into the standard deviation of the three injections for each sample. If the deviation of one injection was higher than 0.1‰ for δ^{18}O and 0.5‰ for δD, this injection will be reconsidered and in most cases disregarded. So the overall precision was determined to be better than 0.1‰ for δ^{18}O and 0.5‰ for δD.

2.5 Dating

The timescale of the whole firn core was based on identified volcanic deposition strata and then counting of layers determined from CFA measurements (Vallelonga et al. 2014). For the top 3 m of the core, annual layer counting was based on the discrete δ^{18}O annual cycles because the compacted snow was not suitable for CFA analysis.

Volcanic deposition were identified by DEP (Dielectric Profiling) (Moore and Paren 1987; Moore and Maeno 1991) and confirmed by ECM (Electrical Conductivity Measurement) (Hammer 1980) and electrolytic conductivity measurements (Kjær et al. 2013). The primary idea is that, volcanic eruptions deposit acids in the ice core, and the acid's protons will enhance the ice's conductivity. In combination with historical records, the enhanced conductivity spikes can be interpreted in terms of recorded volcanic eruptions. It thus provides a handy tool for dating the ice core. Table 2.2 presents the main volcanic strata identified in this core (Vallelonga et al. 2014).

Table 2.2: Year and depth for the volcanic strata identified in NEGIS core.

Volcano	Year	Depth [m]
Katmai	1912	22.7
Tambora	1816	39.0
Unknown	1810	40.0
Laki	1783	44.3
Komagatake	1640	62.0

Annual layers between volcanic strata were counted based on the impurities measured from CFA (details see Section 3.1.1). Datetool2, a Matlab program developed by Rasmussen (Rasmussen 2006) was used here to collect the various parameters and match the annual layer markings (Figure 2.3).

The volcano-based estimate was in good agreement with the annual layers counting. There is no volcanic strata to be checked on for the end part of the core and the age before 1640 AD (Komagatake volcanic eruption) is of ±1 year uncertain. At last, the age at the bottom of the core is determined as 1607 AD with a precision of ±1 year (Vallelonga et al. 2014).

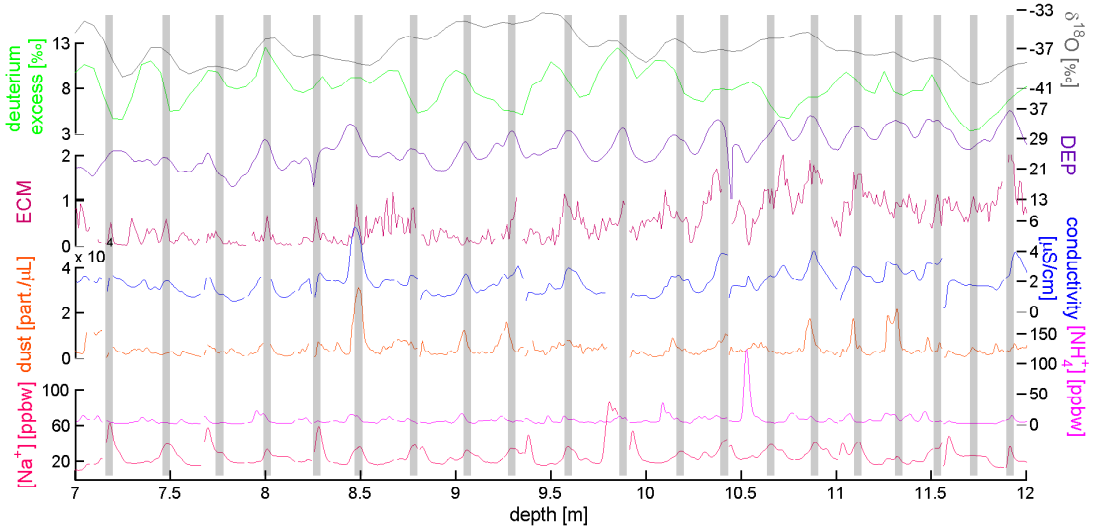

Figure 2.3: Example of NEGIS core dating at depth interval of 7-12 m. Grey bars indicate the annual year markings. The dating here is mainly based on DEP and Na^+ record. Note that below ∼8 m depth the $\delta^{18}O$ record becomes too diffused to reveal annual cycles.

2.6 Results

The results of the discrete measurements as well as the annual layer thickness are presented in Figure 2.4. Two immediate observations merit some further discussion.

First, the isotopic composition in the NEGIS core is strongly smoothed by diffusion. Hence, the layer counting based on $\delta^{18}O$ annual cycles is possible for the top ∼8 m of the core only. Due to the difference between diffusion velocities of $\delta^{18}O$ and δD, deuterium excess can still show annual cycles until ∼10 m depth (see Figure 2.3). The rapid decay of the annual cycle is because of the low annual accumulation rate at the NEGIS drilling site. In north eastern Greenland the annual precipitation rate is significantly lower than 0.2 m (Bales et al. 2001, 2009). Indeed the averaged annual layer thickness at NEGIS is only ∼0.11 m ice equivalent (i.e.). Assuming a same diffusion process, the annual isotopic signal in a thinner annual layer will be more highly diffused within the layer and also to a more extent diffused with the neighboring layers.

Second is that the $\delta^{18}O$ profile shows relatively light values from roughly 30 - 45 m, at which depth the annual layer thickness i.e. is anomalously high. Light values of water isotope ratios usually corresponds to a low precipitation rate at the local site, assuming the precipitation always comes from the same water source (Dansgaard 1964). Provided no dramatic shift of the local climate pattern had happened during this time period, the unmatch of $\delta^{18}O$ profile and annual layer thickness is very likely caused by the upstream topographic undulations and fast ice flow (Reeh et al. 1985). The perturbations of accu-

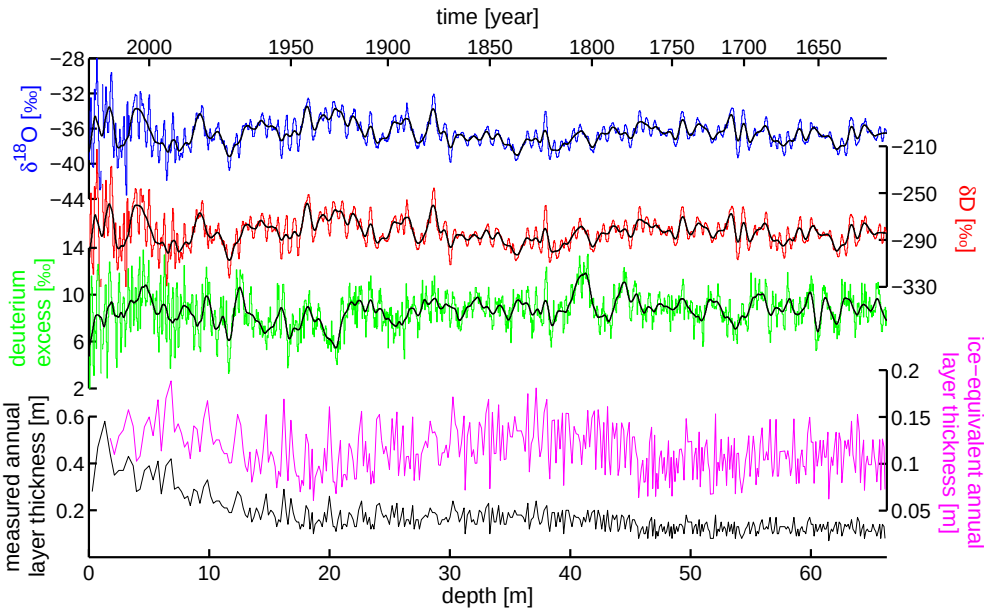

Figure 2.4: Results of water isotope discrete measurements of NEGIS core. Black lines indicate data after smoothing. Smoothing is based on the built-in Matlab "smooth" function with a method "lowess" (local regression using weighted linear least squares and a 1st degree polynomial model). At the bottom, the annual layer thickness both from measured and ice equivalent calibrated are shown. Note the anomalously high values from the ice-equivalent annual layer thickness in depth range of 30 - 45 m.

mulation rate can be explained as follows.

When the ice flow is over an undulated base, the basal elevation changes will cause undulations of the ice sheet surface. Within the same precipitation period, the relatively low valleys will be able to capture more snow than the relatively high hills in the later redistribution of snow caused by natural forces such as wind blowing. Thus the accumulation rate from valleys will be higher than that from the hills. Besides, the actual precipitation rate might also vary itself with distance. Though the core drilling site is usually chosen to be on a flat surface, the (fast) ice flow can introduce the upstream variations of accumulate rate to the drilling site. The variations from a further distance in upstream will affect a deeper part of the ice core from drilling site. And the ice stream with a faster flow will bring in the variations from a longer distance. Thus a full interpretation of the accumulation rate (annual layer thickness i.e.) profile will include temporal variations plus upstream variations of the accumulation rate in a considered distance. For the 30 - 45 m part of NEGIS core, the anomalously high values from the annual layer thickness i.e. can be explained as: this part of the core was originally deposited in a valley surface from the upstream some distance away. The upstream effects of surface topography can be illustrated in Figure 2.5.

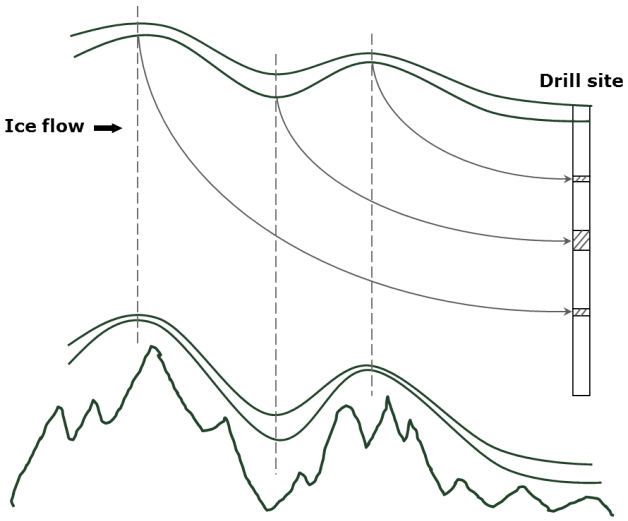

Figure 2.5: Indication of the upstream effects of surface topography.

Chapter 3

Continuous Flow Measurements

3.1 Experimental setup

3.1.1 Continuous Flow Analysis (CFA)

The Continuous Flow Analysis (CFA) has become a well-established method to obtain information about impurity contents in ice cores in high resolution. It has numerous advantages compared to the traditional discrete sampling methods, such as fast and efficient decontamination of the sample, high depth resolution, and time and labor savings. It can also be simply coupled with other techniques, such as greenhouse gas measurement (Schüpbach et al. 2009; Stowasser et al. 2012) and water isotope measurement as here. The CFA system has been refined and widely used over the past two decades (Sigg et al. 1994; Röthlisberger et al. 2000; Kaufmann et al. 2008; Bigler et al. 2011). A CFA system developed at the Center for Ice and Climate at University of Copenhagen is presented in Figure 3.1 and briefly described as follows.

An ice core bag is melted continuously at a speed of ∼4 cm/min (∼5 cm/min for the upper 20 m of NEGIS core) on a gold coated plate which is located in a cold freezer (–15°C). Only the inner part which was never in contact with ambient air is used and pumped into a warm lab, whereas the possibly contaminated water from the outer part is rejected. The melt water stream still contains air bubbles (approx. 10% of the total volume) from the enclosed air in the ice. The air is removed in a debubbler (for the deep ice core studies the air can be used for gas measurement (Stowasser et al. 2012)). Then the sample stream is split and passed into a number of other analysis systems for on-line analysis.

The final obtained records consist of electrolytic melt water conductivity, insoluble dust, sodium (Na^+), ammonium (NH_4^+), hydrogen peroxide (H_2O_2), calcium (Ca^{2+}), nitrate (NO_3^-), sulfate (SO_4^{2-}), and phosphate (PO_4^{3-}). The impurities come from different sources and thus yield different information about the climate system. Those impurities that have annual cycles can be used for identification of the annual layers in the ice (see Section 2.5). The following is a brief introduction of the impurities from Greenland ice cores.

Ammonium (NH_4^+) originates from biomass burning such as forest fire, anthropogenic emissions such as excreta, and soil and vegetation (Fuhrer et al. 1996). It usually shows

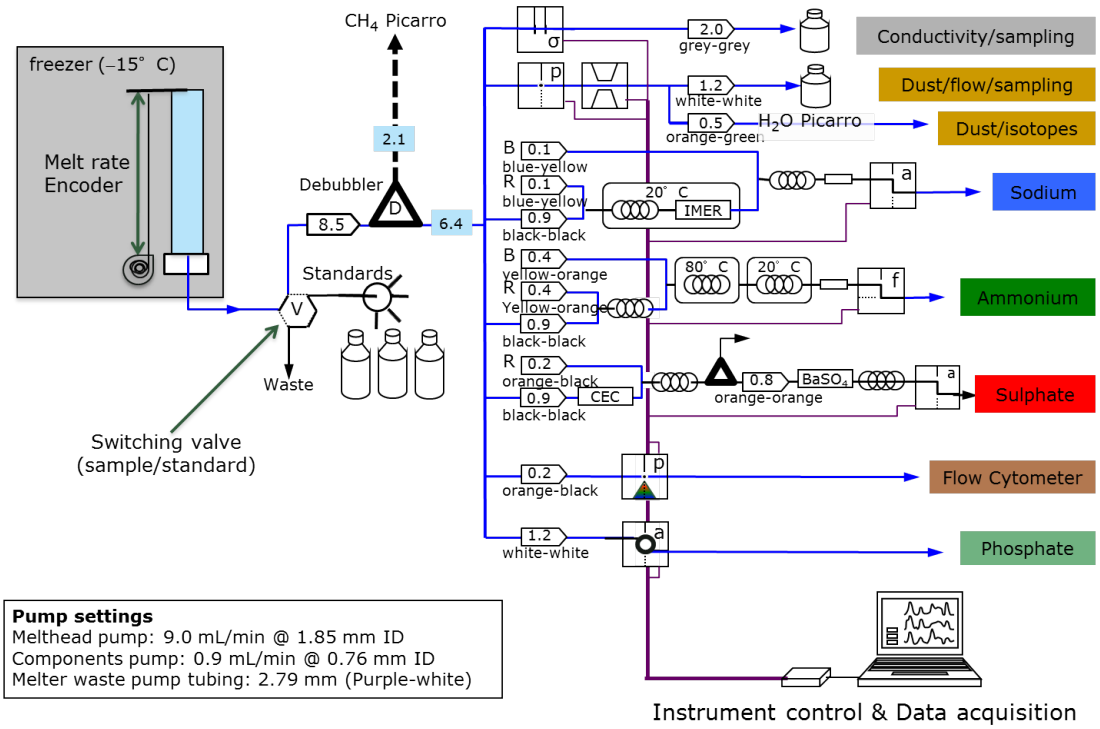

Figure 3.1: Schematic of the CFA system developed at the Center for Ice and Climate (modified from Bigler et al. (2011)). Not all of the components are measured on the NEGIS firn core. The flow rates here are not related to the NEGIS firn core, but indicates the approximate sample distribution.

an annual summer peak. North America is considered the main source area for Greenland ice cores due to the western atmospheric circulation pattern.

Sodium (Na^+) is mainly from sea-salts that derives from ocean sprays (Busenberg and Langway 1979) but also has other sources such as mineral dust. The sodium concentration usually has high values during colder periods.

Dust from Greenland ice cores originates almost entirely from deserts and dry areas in eastern Asia, such as Gobi desert (Svensson et al. 2000). The amount of dust that reached Greenland is much greater during the colder periods when the winds were stronger and that particle wash-out in the atmosphere was much less efficient.

Conductivity measured in the CFA system is a bulk signal of all ionic constituents, including both positive and negative ions. Note its difference to the ECM measurements where the amount of hydrion (H^+) is mainly measured.

3.1.2 Water isotope measurements

For the continuous flow water isotope measurements, a commercial water isotope spectrometer (NIR-CRDS), Picarro L1102-i (Crosson 2008), was coupled with the CFA system to obtain water isotope ratios. A sketch of the coupled system is given in Figure 3.2. It

follows the same approach as presented in Gkinis et al. (2010) and is briefly described in the following.

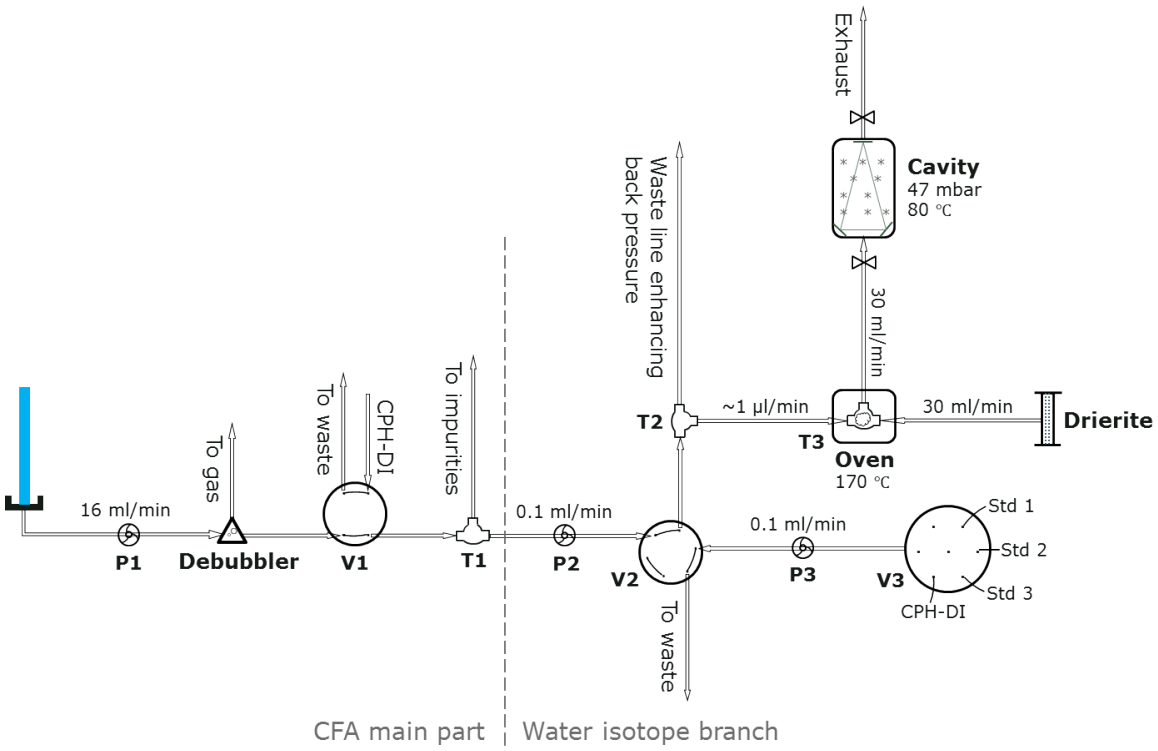

Figure 3.2: Block diagram of the CFA system coupled with setup for water isotope measurements (modified from Gkinis et al. (2011)).

After debubbling and distributing to impurities measurements (T1), melt water from CFA is pumped into the CRDS system through a peristaltic pump (P2). The total sample consumption for water isotope measurement is maintained to be $\sim$ 0.1 ml/min. The sample water is then passed through a tee-split (T2) and a capillary tube into the oven. The oven is set to 170°C regulated with a PID controller to acquire an immediate and 100% evaporation of the injected water. By tuning the waste line with different lengths and inner radius, one can adjust the pressure gradient between the inlet and waste port of the T2 tee-split and thus the flow rate to the oven.[1] In this way, the amount of the

[1]Assuming an impressible and laminar flow, an estimate of the pressure along a tube is given by the Hagen-Poiseuille law:

$$\Delta P = \frac{8\mu L Q}{\pi r^4},$$

where ΔP is the pressure drop along a tube, L is the length of the tube, r is the inner radius, μ is the dynamic viscosity, and Q is the volumetric flow rate.

Proper selection of length and inner radius for both the waste line and the capillary tube will balance the pressures of these two downstream sides of T2. Therefore, at a steady state, the flow through the

injected water to the oven can be maintained to be ~ 1 μl/min.[2]

Dry air at a flow rate of 30 ml/min constantly blows into the oven to mix with the water vapor, keeping the water concentration at the required level. At last, the mixing of water vapor and dry air passes into the cavity to complete the isotopic composition measurements. The cavity keeps a pressure of 47 $mbar$ by adjusting two proportional valves in a feedback loop up and down stream of the cavity, and maintains a temperature of 80°C.

A 6-port injection valve (V2) is used to switch between the sample from the CFA line and a set of local water standards. 4 water standards are measured for SMOW calibration (see Section 3.2.2). Another 6-port selection valve (V3) is used to switch between standards. By changing the pump speed of P3 thus changing the water concentration in the cavity, the sensitivity of the system can also be investigated and calibrated (Gkinis et al. 2010).

Note that the CRDS used here is a slightly older Picarro model compared to Picarro L2120-i used for discrete measurement. The difference of the instrument model may also have an influence on the interpretation of the difference obtained between the two types of data.

3.2 Data analysis

To obtain the isotope signals, the raw data need to be processed in the following steps as shown in Figure 3.3. First, before any further processing, two times of calibration are applied to refer the measured isotopic value to the same water concentration level and to the VSMOW scale. So the obtained isotope signals can be compared to the other existing isotope signals. Then, the isotope signals need to be extracted out from the background water signals. At last, the isotope signals are linked to the depth scale, thereby various climate information can be interpreted from the signals.

---

capillary tube, Q_c, will be obtained:

$$Q_c = Q_w \frac{L_w r_c^4}{L_c r_w^4} \approx Q_m \frac{L_w r_c^4}{L_c r_w^4},$$

where Q_w and Q_c are the flow through the waste and main line respectively. r_c and r_w are the inner radius of the capillary tube and the waste line, and has a typical value of 10 μm and 75 μm, respectively. The length of the capillary tube, L_c, is fixed. Therefore, the flow rate to the oven can be tuned by adjusting both the length of the waste line, L_w and the flow rate of the peristaltic pump (P2).

[2]A water concentration in the range of 17,000 - 22,000 ppmv in the optical cavity results in optimum spectrometer performance(Gkinis et al. 2010). With a dry air flow rate, $V_a = 30$ ml/min, and a water concentration, $C_w = 20,000$ ppmv, the required injection rate of liquid sample water, V_w, can be calculated as:

$$V_w = C_w(V_w + V_a)\frac{\rho_v}{\rho_w} \approx C_w V_a \frac{\rho_v}{\rho_w} \approx 0.5\ \mu L/min,$$

where ρ_w and ρ_v are the density of liquid water and water vapor respectively. V_w is of 10^4 orders smaller compared to V_a and thus can be neglected here. Calculation is assumed under standard temperature and pressure (STP).

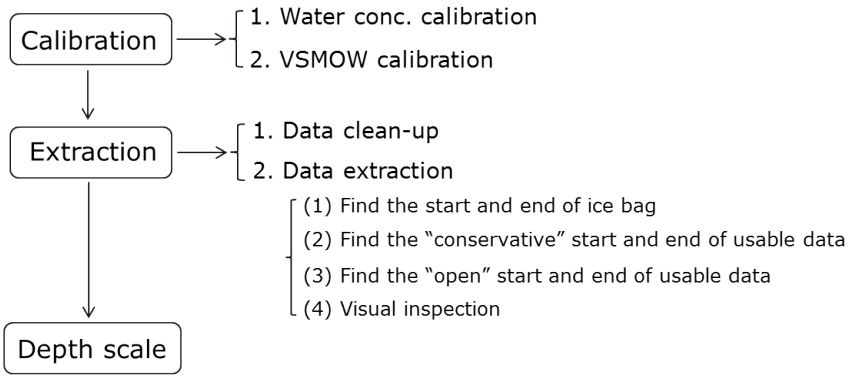

Figure 3.3: The flow chart of the data analysis steps for CFA flow measurements.

3.2.1 Water concentration calibration

The NIR-CRDS system has a dependence on the cavity humidity levels. To a good approximation, the δ^{18}O and δD signals show a linear response to differences in water concentrations around 20 000 ppmv (Brand et al. 2009; Gkinis et al. 2010). The raw data need to be corrected for the water concentration fluctuations in the optical cavity before any further processing. Here the same correction as described in (Gkinis et al. 2010) is performed:

$$\Delta\delta = a_i \cdot (R_{20} - 1) \tag{3.1}$$

where $R_{20} = \frac{[H_2O]}{20000}$, $a_{18} = 1.94‰$ and $a_D = 3.77‰$. Note that the coefficients are experimental and may only hold for this specific spectrometer.

3.2.2 VSMOW calibration

A difference exists between the expected values and the measured values from the spectrometer system. Therefore a calibration is needed to refer the measured values to the VSMOW scale. The same three standards previously described in discrete measurements (Table 2.1) were measured to calibrate the spectrometer system. Based on the same process, we can obtain a two-point calibration line for the continuous flow measurements:

$$\delta_{VSMOW} = \alpha_{cfa} \cdot \delta_{measured\_cfa} + \beta_{cfa} \tag{3.2}$$

Only two times of calibration were implemented for the whole series of continuous flow measurements presented here. One calibration was done before the start of the measurements and the other one was after the end of the measurements. The measurements of these two calibrations are presented in Figure 3.4. Three water standards, "-22", "-40" and "NEEM", were measured. The local deionized water ("CPH-DI": δ^{18}O= $-8.70 \pm 0.01‰$; δD= $-60.26 \pm 0.1‰$) is measured at the start and end of the measurements as a background value.

The three water standards are measured in an order of "-22" $\rightarrow$ "NEEM" $\rightarrow$ "-40" $\rightarrow$ "NEEM" $\rightarrow$ "-22". It is measured from the standard of the heaviest value to the one of

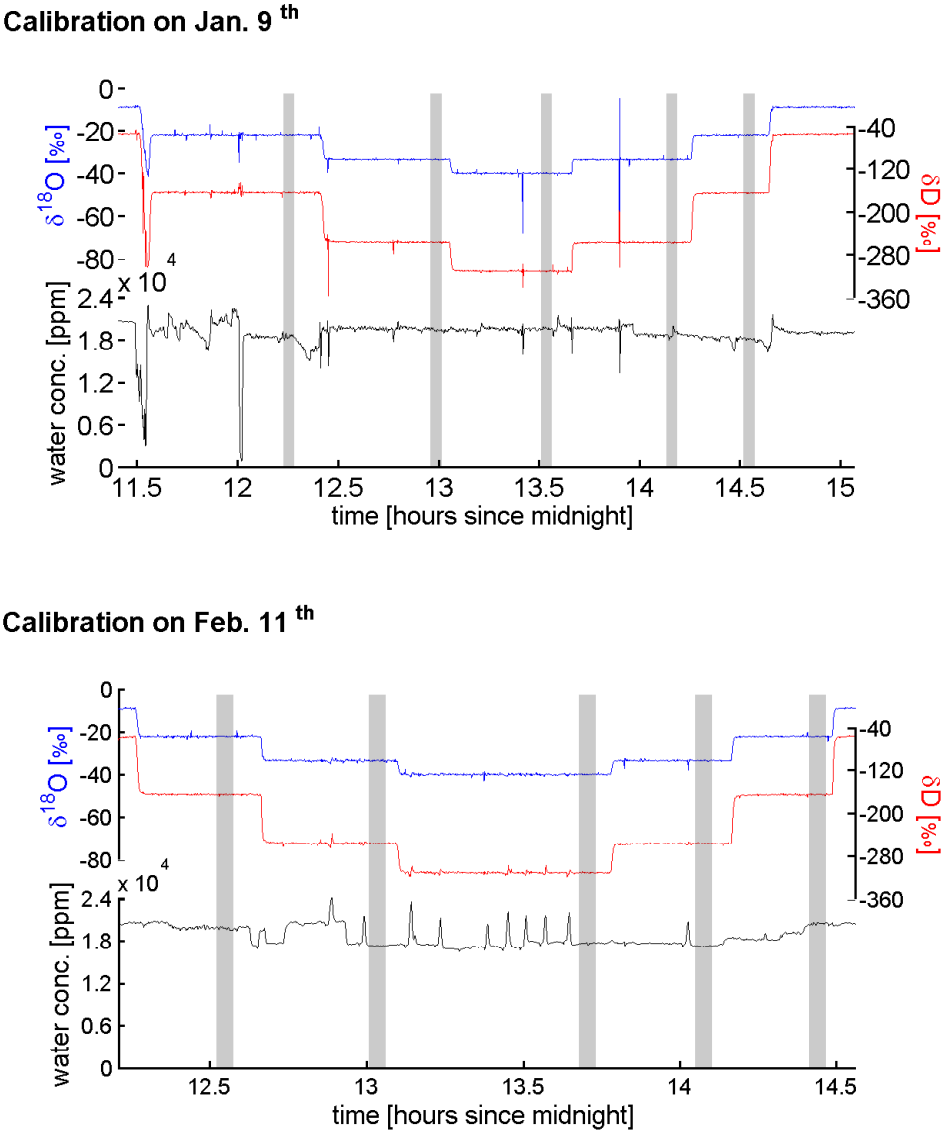

Figure 3.4: The δ^{18}O and δD of the three water standards and cavity water concentration during the measurements (Blue: δ^{18}O; Red: δD; Black: water concentration). Both of the calibrations from January and February are presented. The y-axis scales are set the same and one can see that the data from the calibration in February shows a better stability. Water concentration calibration is already processed. Grey bars indicate the selected data that are used to calculate the mean value of each standard.

the lightest and then back to the one of the heaviest again. Thus the standard of "-22" and "NEEM" are measured twice and an averaged value is used in the calibration. This will help to account for the possibly remained memory effects from the upstream standard of both heavy and light values. The data points that are used to estimate the measured value of each standard are carefully selected, in order to minimize the memory effects from the upstream standard as well as to avoid outliers likely caused by randomly interrupted water sample delivery (Gkinis et al. 2010). At last, only 30 data points close to the end of each standard measurements are chosen to be used. In this way, we get the measured values for the three water standards. Results are shown in Table 3.1.

Table 3.1: Measured isotopic values of the three water standards from calibrations in January and February (‰). The precision is given by one standard deviation. The finally used two-point calibration line is based on the total mean values of the two calibrations.

δ^{18}O

Standard	Jan.		Jan. mean	Feb.		Feb. mean	Total mean
-22	-22.24 ± 0.21	-22.24 ± 0.16	-22.24 ± 0.18	-22.16 ± 0.22	-22.25 ± 0.19	-22.21 ± 0.20	-22.22 ± 0.19
NEEM	-33.92 ± 0.17	-33.93 ± 0.17	-33.93 ± 0.17	-33.83 ± 0.27	-33.82 ± 0.19	-33.82 ± 0.23	-33.88 ± 0.20
-40		-40.35 ± 0.20			-40.19 ± 0.17		-40.27 ± 0.19

δD

Standard	Jan.		Jan. mean	Feb.		Feb. mean	Total mean
-22	-164.50 ± 0.63	-165.21 ± 0.57	-164.85 ± 0.60	-165.70 ± 1.13	-165.59 ± 1.04	-165.65 ± 1.09	-165.25 ± 0.85
NEEM	-255.96 ± 0.64	-256.50 ± 0.71	-256.23 ± 0.67	-256.93 ± 0.75	-256.82 ± 0.76	-256.87 ± 0.76	-256.55 ± 0.72
-40		-310.75 ± 0.59			-311.33 ± 0.82		-311.04 ± 0.71

In the same way as described in the calibration for the discrete measurements, two of them ("-22" and "-40") were used to estimate the two-point calibration line and the third one ("NEEM") serves as a quality control. The obtained calibration lines from both January and February are presented in Figure 3.5. The coefficient of determination for all the calibration lines is high (R^2 ≈0.9999). To give an indication of the accuracy obtained by the system, the offset of the calibrated value ($\delta^{18}O_c$, δD_c) and the expected value ($\delta^{18}O_e$, δD_e) for "NEEM" is calculated. The offset is 0.0017‰, 0.0103‰ for δ^{18}O and -0.2297‰, -0.2407‰ for δD, for January and February calibration, respectively.

From Figure 3.4, it seems that the measurements for the calibration in February are more stable and reliable compared to those in January. However, the variations between two measurements are comparable with the one standard deviation or even smaller (Table 3.1). Thus the variations would be acceptable within the precision level of the measurements. One can also gain confidence for both of the data from the comparable results of two calibration lines (Figure 3.5). It is always preferable to use the calibration data from the same or the closest time span to calibrate the data. Since one calibration here is carried out at the beginning of the experiment and the other one at the end, it is more convincing to take the average values of the two data sets for calibrating the whole NEGIS core measurements.

The final two-point calibration lines based on the average values of two calibrations ("Total mean" in Table 3.1) are presented in Figure 3.6. The offset for "NEEM" is 0.0064‰

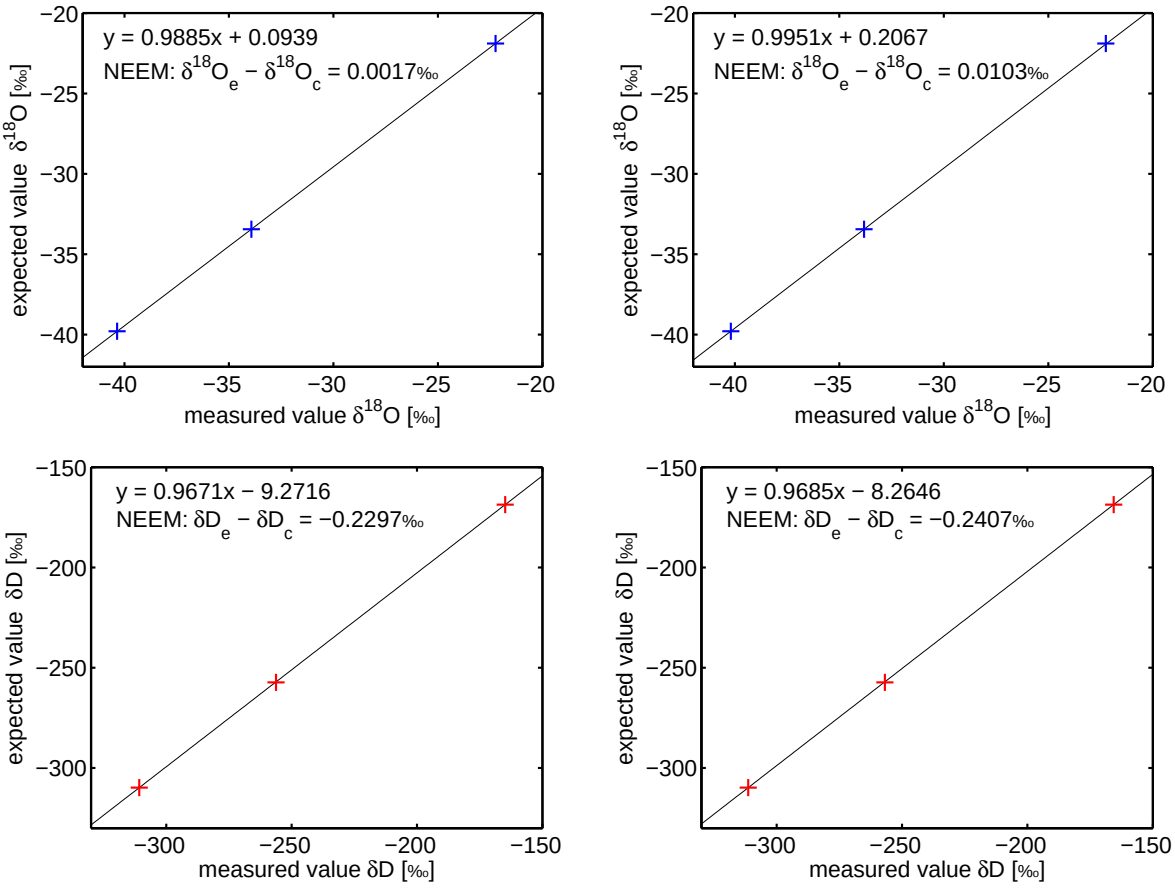

(a) Calibration on Jan. 9^{th}

(b) Calibration on Feb. 11^{th}

Figure 3.5: Two-point calibration lines estimated from January and February calibrations, respectively. Two water standards, "-22" and "-40" are used to calculate the linear coefficients and the third one, "NEEM", is used to check the fitting quality.

for δ^{18}O and -0.2344‰ for δD. The calibration lines are then applied to calibrate the samples from measured values of the spectrometer to the VSMOW - SLAP scale and hence the isotopic ratios are able to compare with the discrete measurement results.

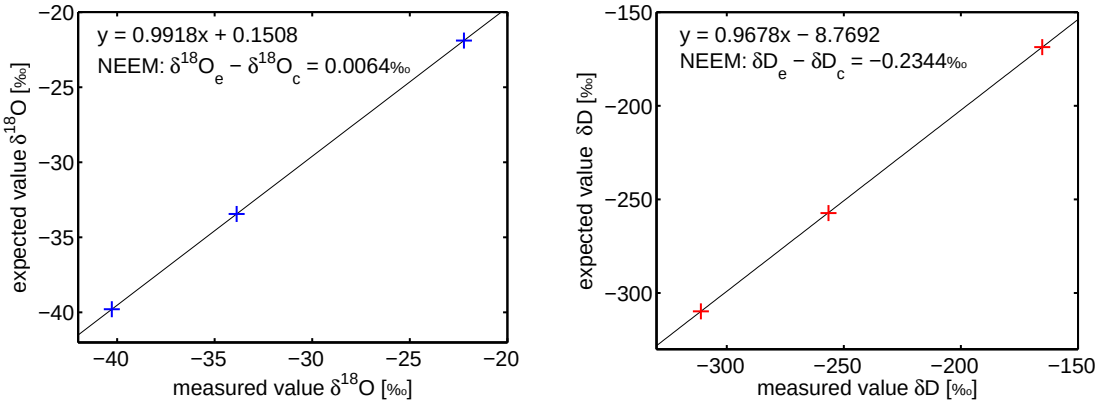

Figure 3.6: The final two-point calibration lines estimated from the average values of January and February calibrations. Two water standards, "-22" and "-40" are used to calculate the linear coefficients and the third one, "NEEM", is used to check the fitting quality.

3.2.3 Extract isotope signals

Between the consecutive melting of two ice bags, a flow of water (here "CPH-DI" is used) is kept measuring as a background signal, in order to keep the spectrometer measuring at a roughly constant water concentration level (∼20 000 ppmv). So the very first measurements consist of signals from both ice sample water and background water. The signals from background water are not wanted here. The only reason for them to be necessary in the measurements is to fill up the measurement gaps between ice bags. Therefore they have to be removed for the final results.

Considering the diffusion, signals from the transition of the two waters have to be properly removed as well. Even though the switch is quick, the background water and ice sample get diffused all the way in the transfer lines: from delivery in the tube to the measurement in the cavity. The top of Figure 3.7 indicates the diffusion process at the beginning of ice melting. If it was before (or without) diffusion, the transfer from background water to ice sample would be clear. Then it would be very easy to determine the boundary. But with diffusion starts, the two water will mix into each other. Assuming the length for diffusion is the same on both sides, the initial transfer boundary would suppose to be where the strongest mixing finds. Therefore, the start point of the ice sample is selected here as the minimum of $\Delta\delta^{18}$O and the end point as the maximum.

The method for selecting the usable isotope data could be to manually look into every ice bag and decide the cutting points by eye; or in an automatic way to run script codes and then to check by eye. Here the latter semi-automatic method is applied. For the future

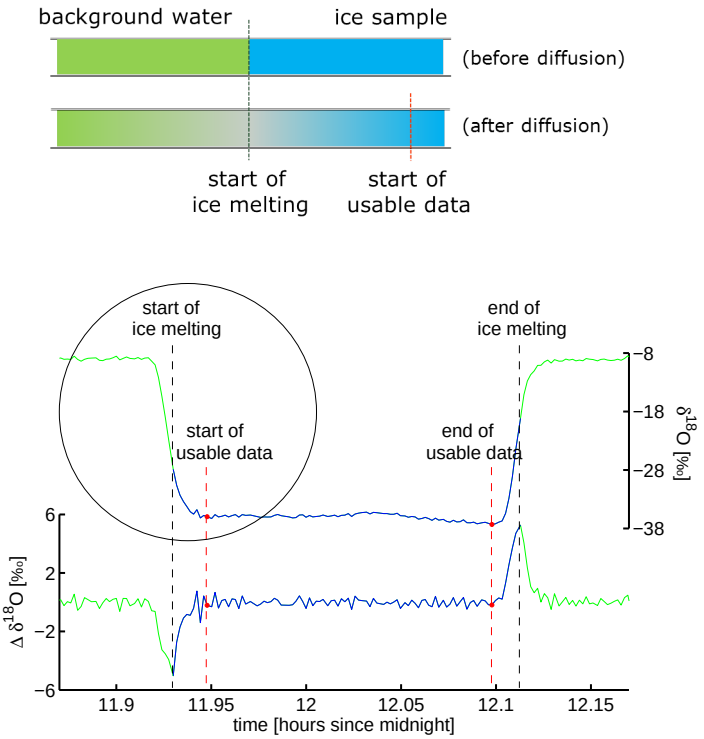

Figure 3.7: Indication of the start and end for both ice melting and the usable isotope data. Blue line indicates the melted ice bag. Green line indicates the background water. The determination of the start is indicated at the top. Because of the diffusion, the beginning part cannot be used for data analysis. The same applies for the end.

continuous measurement of deep ice cores, running a proper script could save much more time. In the following part, the measurements of 5 ice bags (bag 17 - 21, depth interval 8.8 m - 11.55 m) are presented as an example to show how the data extraction works.

1) Data clean-up

A manual cleanup of the raw data is done before any further processing (Figure 3.8). The irregular parts of the data are removed in order to avoid the interruptions during running script later. The irregular parts here are normally caused by some unpreventable problems, i.e., melting problems or interrupted sample delivery.

2) Extraction

First, the start and end point of each melted ice bag is determined by looking into the distinct change from background water to ice sample (Figure 3.9). The extrema of $\Delta\delta^{18}$O, i.e., the differences between the two consecutive δ^{18}O signals, are located approximately in the middle of the transition and are thus treated as the expected start and end point for each ice bag. Then, a small part of data at both the beginning and the end of each measured ice bag have to be excluded because of the diffusion and memory effects. After this, the first version of the usable isotope data will be obtained.

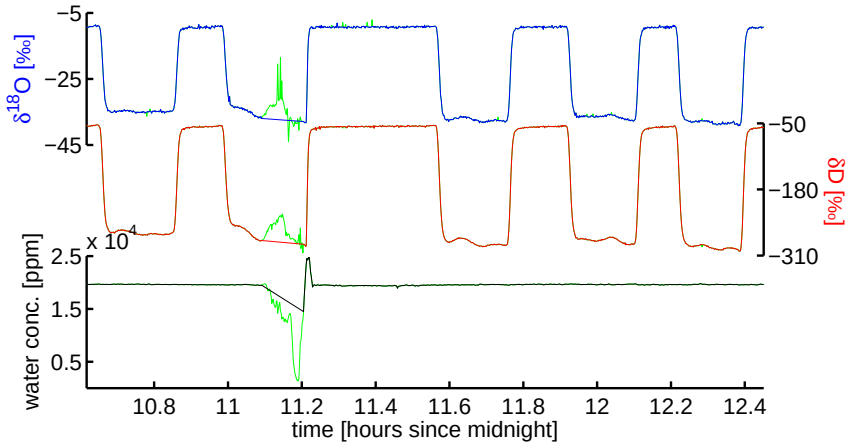

Figure 3.8: Raw data from measurements of 5 bags (bag 17 - 21, depth interval 8.8 m - 11.55 m) and cavity water concentration during the measurements (Blue: δ^{18}O; Red: δD; Black: water concentration). Green line indicates the removed sections caused by melting problems or interrupted sample delivery. "CPH-DI" water is measured between two consecutive measurements as a background signal.

A semi-automatic method was developed to do the extraction step. Basically, a Matlab script was written to find the logically approximate start and end points for each ice bag. Thereafter a check and adjustment by eye gave the final results. Take ice bag 20 as an example (Figure 3.10). The detailed steps for the extraction are explained as follows.

(1) To find the start and end of the ice bag

This is done by checking the extrema of $\Delta\delta^{18}$O. Since they are where the gradient from one water to another is the biggest, these extrema are defined as the start and end point of the ice bag.

(2) To find the "conservative" start and end of the usable isotope data

This is done by checking the ambient data points of the extrema found in step (1) to find the first data point that comes above zero after the start point and the first one that comes below zero before the end point. These two data points indicate the start of domination from the ice sample water and the background water, respectively. This may in some cases exclude too much information, since the $\Delta\delta^{18}$O signals from only ice sample water can also vary between negative and positive within itself. Therefore these two data points are only regarded as conservatively estimated and are so-called the "conservative" start and end. The next step will be to reasonably broaden this conservative interval.

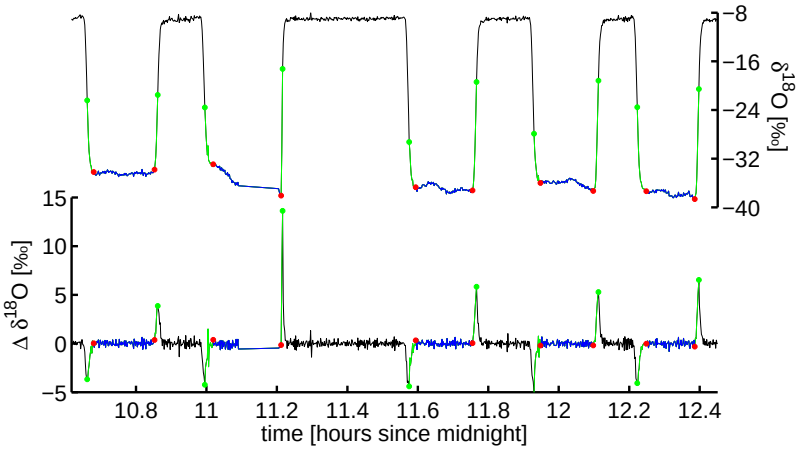

Figure 3.9: Data selection from the δ^{18}O signals of bag 17 - 21 after cleanup. The beginning and end of melting (green dots) for each ice bag is determined by the extrema of the δ^{18}O signal differences. Data from the transition part between background water and sample water (green line) are discarded due to sample dispersion and memory effects. The finally selected start and end points for the usable isotope data are indicated by red point and the retained data are indicated by blue line.

(3) To find the "open" start and end of the usable isotope data

The mean (M_c) and the standard deviation (σ) of this conservative interval are calculated. Then the first data points that are within $M_c \pm 3\sigma$ can be found at both start and end. $\pm 3\sigma$ is considered here so as to include enough more data points for the manual adjust later. It will include some uncertain data points that may have been mixed with the background water and therefore are so-called the "open" start and end. All the steps from (1) to (3) are logical and can be done within a Matlab script.

(4) To visually inspect and manually adjust the "open" start and end to a proper point

This is done by going back to the δ^{18}O record to see if the value of the start and end points fit smoothly with the neighboring ice bags. The available data from discrete measurements are also used for a double check (Figure 3.10 (right)).

The final determined point is usually located in between the "conservative" point from step (2) and the "open" point from step (3). But in many cases, like bag 19 - 21 that are

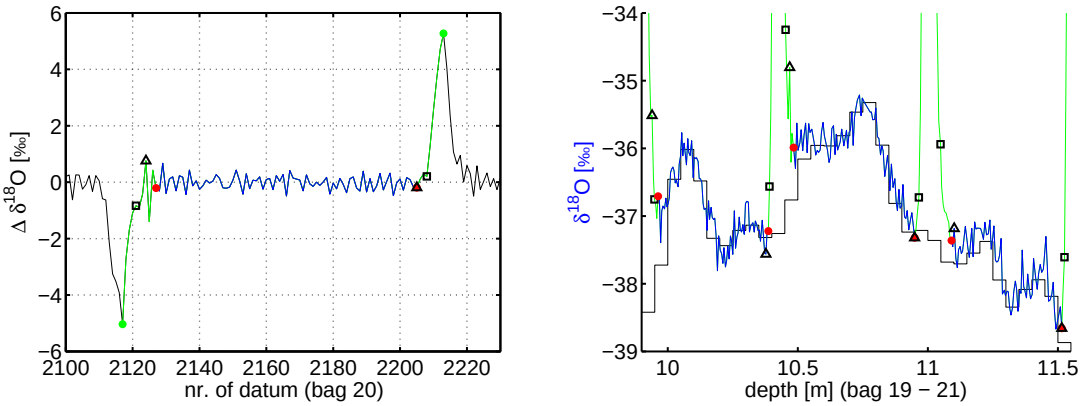

Figure 3.10: Bag 20 is presented as an example of data extraction in details (left) and the δ^{18}O of bag 19 - 21 is presented to show how the results look like corresponding to the different selected points (right). Green dots are the extrema of $\Delta\delta^{18}$O, indicating the start and end of measuring ice bag. Triangles indicate the first data points that come above zero after the start or below zero before the end, regarded as the conservative start and end points. Squares indicate the first data points that are within $M_c \pm 3\sigma$. Red dots indicate the final selected points after adjusting by eye. For bag 20 and 21, the red dot and the triangle overlapped at the end of the bag. Results from discrete measurements (black line in the right figure) are also shown here for a double check.

shown here, it is most likely to be found within the conservatively estimated interval. This tendency is found stronger especially in the determination of the start points. This is more obvious if we look into the gaps (amount of datum) between the start/end of the usable data and the start/end of the "conservative" interval (Figure 3.11 (right)). The determined start points tend to be within this interval with a mean value of ∼2.6 data points or ∼0.3 cm; while the determined end points show a general good consistence. It indicates that the co-called "conservative" point is actually not conservative enough, at least for the start points. Diffusion still plays an important role after the downstream sample starts to dominate in the δ^{18}O signals. It also seems that the sample from the downstream is more affected by diffusion than that from the upstream. This could be mathematically explained if we try to fit the diffusion process with a scaled version of the cumulative distribution function (CDF). The distribution is more like a positive skew distribution (skewness to the right) rather than a normal distribution (Gaussian distribution). This will be discussed further in detail in Section 4.2.

To prevent from diffusion, some part of data at the transitions are removed. Therefore, there is a gap between the start of an ice bag and the start of usable isotope data as well as for the end (Figure 3.11 (left)). The average gap at the start is ∼11 data points and at the end ∼6 data points. The spectrometer records each data point about every 6.5 - 8.5 s. Considering the overall melting speed for the whole measurements is about 4.2 cm/min, the average lengths of ice missed at the start and end are approximately 5 cm and 3 cm

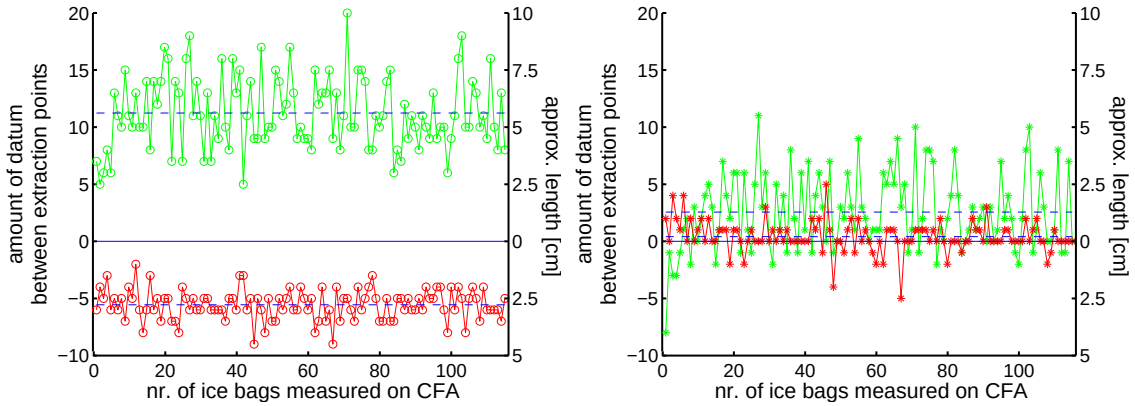

Figure 3.11: The gaps between the start/end of the ice bag and the start/end of usable data (Left: green circles for the gaps between start points and red circles for the gaps between end points); and the gaps between the start/end of usable data and the "conservative" start/end (Right: green stars for the gaps between start points and red stars for the gaps between end points). Blue dash lines indicate the average value of the gaps. The y-axis scales are set the same for the convenience of comparison.

respectively. A future possibility for a fully-automatic way to extract usable isotope data could be to develop a script to cut off 5 cm after the melting start and 3 cm before the melting end uniformly for all the bags.

3.2.4 Generating depth scale

The extracted isotope data can be interpretable in context only when it is put on the right depth scale. As mentioned in Section 3.1.1, only the clean part of the ice core is needed for the CFA system in order to measure the impurities of the ice core. Thus, all the breaks within ice bag as well as the two ends need to be cut off to prevent contamination. In most cases, the ice bag melted in the CFA system is not intact, but consists of several pieces (Figure 3.12). Where and how long the missing parts are, unfortunately, cannot be seen from the output signals of measurements. They are, however, recorded down on the cutting notes while cutting ice bags (example see Figure 3.13). To build a correct depth scale for the whole ice core, all gaps must be put back into the measured data correctly.

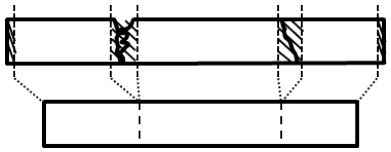

Figure 3.12: Breaks within the ice bag and the two ends are cut off to prevent contamination. The actually melted ice bag is a reunion of the remains.

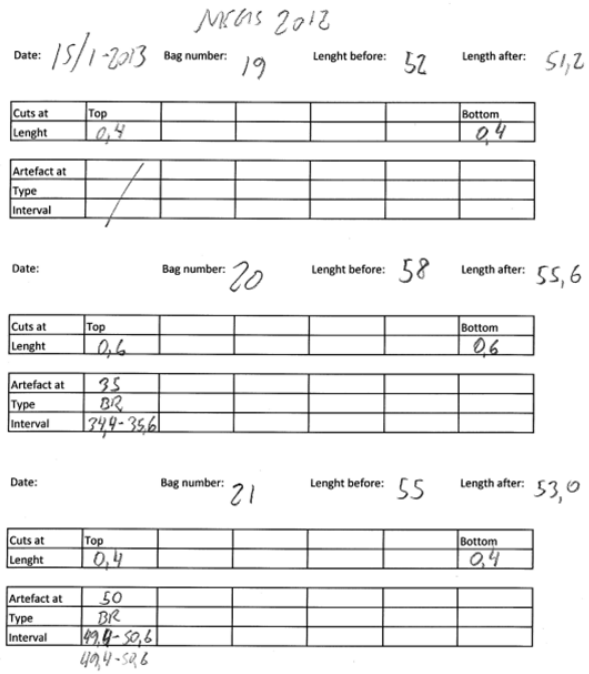

NEGIS 2012

Date: 15/1-2013 Bag number: 19 Lenght before: 52 Length after: 51,2

Cuts at	Top					Bottom
Lenght	0,4					0,4

Artefact at						
Type						
Interval						

Date: Bag number: 20 Lenght before: 58 Length after: 55,6

Cuts at	Top					Bottom
Lenght	0,6					0,6

Artefact at	35					
Type	BR					
Interval	34,4-35,6					

Date: Bag number: 21 Lenght before: 55 Length after: 53,0

Cuts at	Top					Bottom
Lenght	0,4					0,4

Artefact at	50					
Type	BR					
Interval	49,4-50,6					

49,4-50,6

Bag nr.	Cut start	Cut end	Cut length	Ice interval
19	0	4	4	0
19	516	550	34	512
20	-30	-24	6	0
20	314	326	12	338
20	544	550	6	218
21	0	4	4	0
21	494	506	12	490
21	546	550	4	40

Figure 3.13: An example of cutting notes. The information of the removed ice is recorded down in situ. It is later transfered to a digital version so as to be read by the script. Note the big value of cut length for bag 19 and negative values of cut start and cut end for bag 20. It is because bag 19 and bag 20 are irregular bags, with original bag length of 52 cm and 58 cm respectively. The missing 30 cm in bag 19 is considered as being cut off; while the extra 30 cm in bag 20 is shifted into a negative scale. These are for the convenience of running a script later on.

This can be done by matching the melting time recorded by the melt rate encoder next to the melting setup of CFA (top left corner in Figure 3.1) with the time recorded by spectrometer. An optical encoder is connected to a wire that is attached to a weight on top of the sample core to record the melted ice length. The encoder measures the movement in counts per second and 25 counts correspond to 1 mm. It records data normally every second. Combining the melting length recorded by the encoder and the cutting position and length from the cutting notes, one is able to build in the missing parts of each bag. It is straight forward, though, some issues that have arisen during the processing are discussed as follows.

Location of the melting start and end

Incorrect selection of the sample start and end could cause an obvious offset of the built depth scale. It is easy to mistake the start and end point for the bag melting by following a selecting indicated in Figure 3.14 (top). One may easily choose such a way by a first view of the data since from the figure the sample signals seem to have immediately appeared after the "melting start" point selected here; and the background water signals start to be introduced after the selected "melting end" point here. However, such a way of selecting results in an apparent offset of the built depth scale compared to the discrete measurements, as illustrated is Figure 3.14 (bottom). For the NEGIS core, the general offset is about 3.2 cm downward.

Chappellaz et al. (2013) has used such a similar approach to analyze a continuous flow methane record from NEEM ice core and found a few centimeters shift of the depth scale downward. The offset could disappear if one chose to select the bag melting start and end points in a way that is illustrated in Figure 3.7. In fact, the correct selecting is straight forward, as being already described in Section 3.2.3. In addition, looking back into the incorrect selecting, one may easily argue why to exclude all the mixing part of signals at the end but at the same time to include all the mixing signals at the beginning.

Irregular ice bags

The NEGIS firn core was cut in the field, logged and stored in so-called "bags". Each bag is normally 55 cm for the convenience of handling. In some cases, one bag might be just a bit (1-3 cm) less than 55 cm. It would not be recommended to cut off so small a piece of ice from the next bag and put it at the end, as in this way it would generate more contamination and thus a waste of usable ice sample. In other cases, a small extra tail (1-3 cm) might also be kept for the same consideration. For all the cases above, the next bag would be cut same length longer or shorter (Figure 3.15).

Encoder and depth

Thanks to the melt rate encoder, both the melting speed and melting time can be recorded and thus the length of the melted ice can be calculated. Though, there are two issues worth to be noticed for processing the data. One is that the recording time step

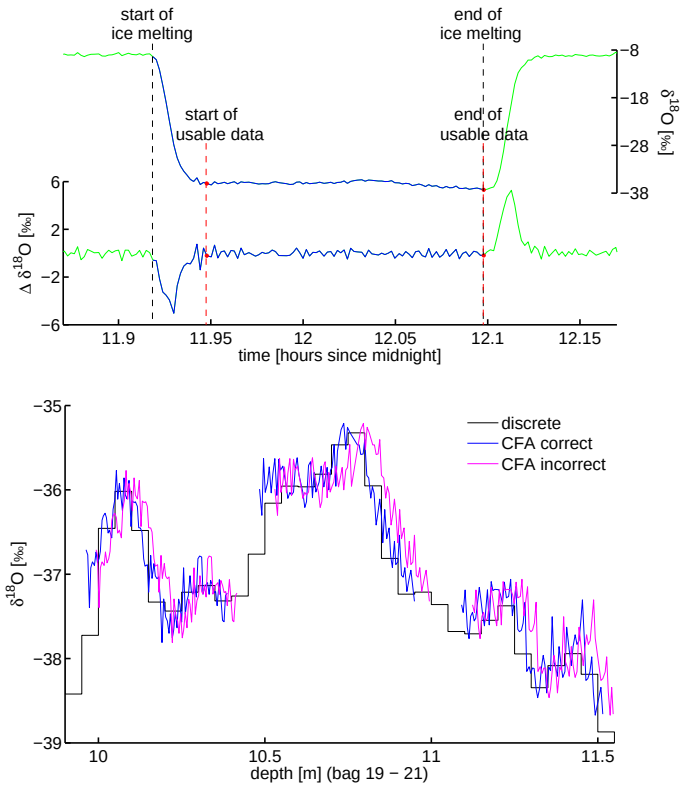

Figure 3.14: Incorrect selection of the sample start and end (top) causing an obvious offset of built depth scale (bottom). Bag 19 - 21 is shown as an example. The general offset is about 3.2 cm downward.

might be irregular instead of one data point every second. In the few cases where the timing steps are way too large, such as 10 s and 23 s, it will not be able to find the corresponding time value from encoder for the data point recorded in spectrometer. This is because the timing step for the spectrometer is about 6.5 - 8.5 s and the way used to calculate the melted ice length is to match the same recorded time by the encoder and the spectrometer. As the melting of ice still continues normally for this case, the problem will be solved by simply interpolating the time interval into seconds. The other problem is that the encoder string or melt copper could have been stuck, bumped up and down during the melting. The reason is that the melting setup cannot be guaranteed perfectly stable and still, and there can also be problems with melting plate. The different situations that have occurred in this study are presented in Figure 3.16. It could result in zero or negative values for the melted ice length and thus twists on the final depth profile. Since it reflects the errors from outside the melting process but not the actual ice length, it will be manually cleaned before data processing.

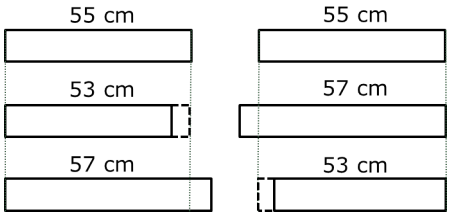

Figure 3.15: Indication of irregular ice bags.

After all the above issues are clarified, a Matlab script is made to build the depth scale. The depth for the start and end of each bag is known to be fixed. The start of the breaks within each bag are considered to be where the melted ice length from the encoder meets the length recorded on the cutting notes. Then the length of the break is added into the depth scale before generating the depth for the next data point. Bag 17 - 21 are presented here (Figure 3.17) as an example of the results.

3.3 Results

After the extraction and transfer to the depth scale, the final results from continuous flow measurements of the whole NEGIS core are presented in Figure 3.18. Results from discrete measurements are also presented here for comparison. First, it can be seen that the two measurements agree well with respect to both the signal trend and depth scale. It therefore confirms the accuracy of the calibrations as well as estimated depth scale for the continuous flow measurements. Second, one can see that, continuous flow measurements have higher resolution. It thus shows more detailed information and can be an advantage especially for the abrupt climate change studies. Though, differences between discrete and continuous flow measurements do exist. The comparison further in detail will be presented in Chapter 4.

Measurements devices cannot be assumed to be in a stable status all the time and instrument drift therefore needs to be considered (Werle 2011). The system stability can be quantified by calculating the Allan variance (described in details by Gkinis, 2010, the same NIR-CRDS system was used). Allan variance (Allan 1966) describes the variance of the mean of a series of measurements for different integration times. In the theoretical case of a zero-drift system, increasing integration time would unboundedly decrease the variance and, thus, the standard deviation of the measurements. However, actually existing instrument drifts will limit this decrease. Therefore, frequent system calibration needs to be implemented in order to guarantee the accuracy of the data.

However, as mentioned previously, only two times of calibration were carried out and only one averaged calibration line was applied throughout the whole NEGIS core measurements. Though, it is noteworthy that the data comparison shows a satisfying agreement between the discrete and the continuous flow measurements. It indicates that, the NIR-CRDS system used for water isotope analysis, at least the one presented here, can perform

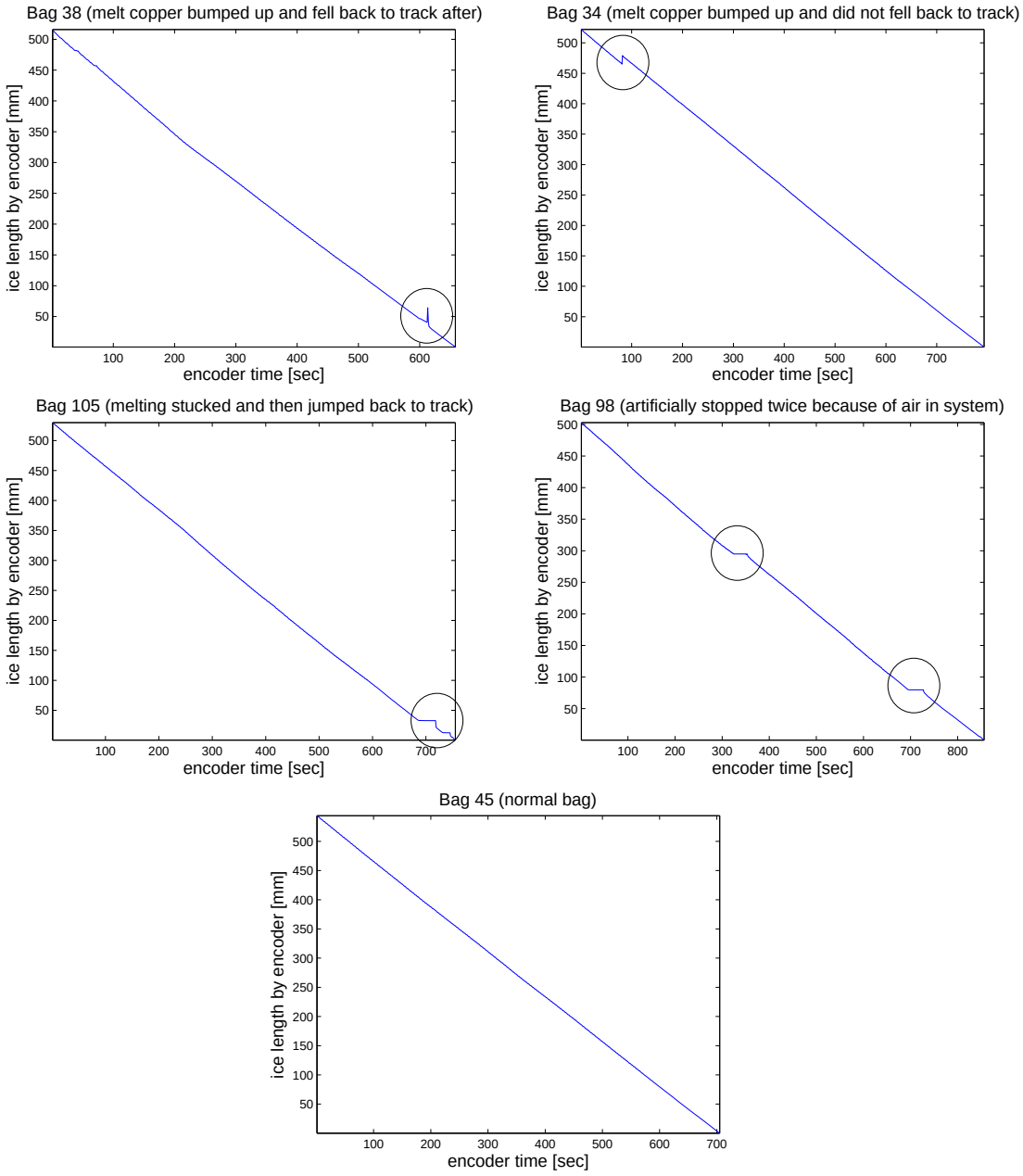

Figure 3.16: Situations where melting problems happened with encoder string or melt copper in the melting setup reflected on the ice melting profiles.

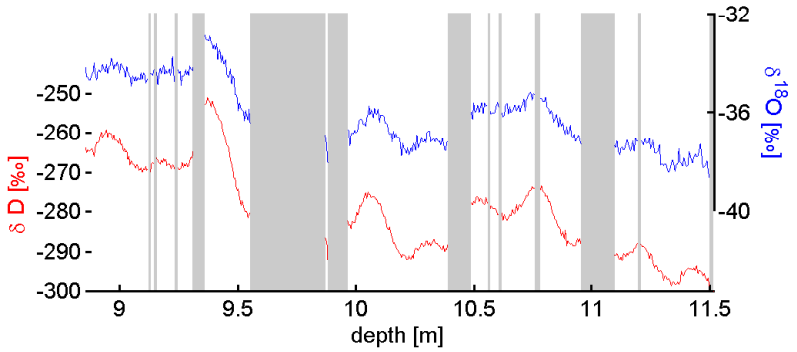

Figure 3.17: δ^{18}O and δD on depth scale for bag 17 - 21. Grey bars indicate the locations and widths of missing data, which consist of breaks in the firn core and removed sections caused by melting problems.

with good stability for a time length of 28 days.

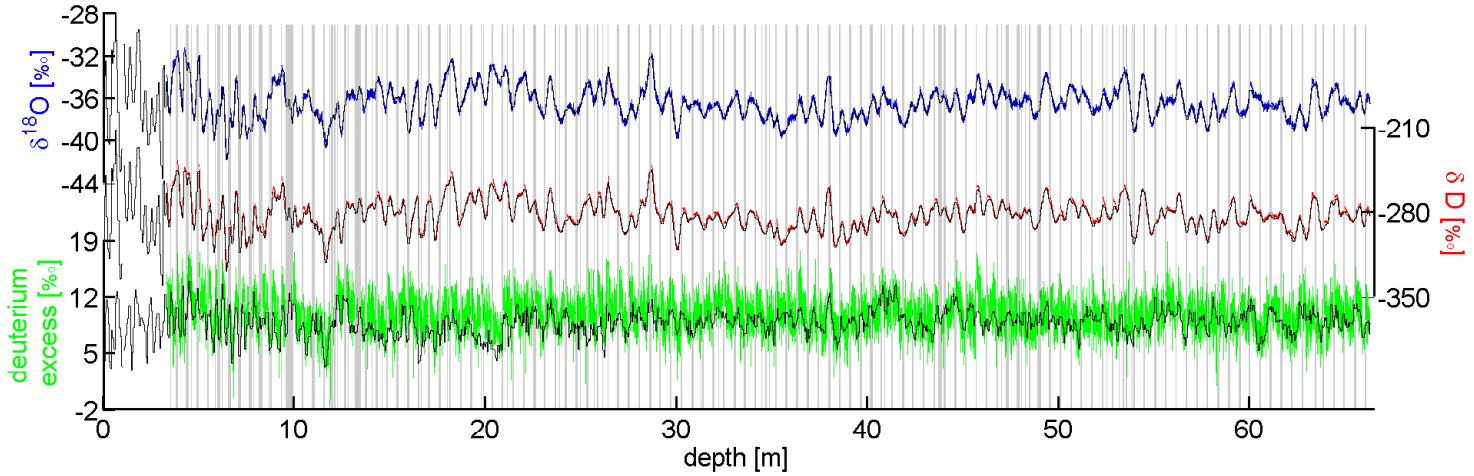

Figure 3.18: Results from continuous flow measurements for the whole NEGIS core. (Blue: δ^{18}O; Red: δD; Green: deuterium excess). Grey bars indicate the positions and widths of the missing data. Results from discrete measurements are also presented (black lines) for comparison.

Chapter 4

Comparison of Discrete and Continuous Flow Measurements

4.1 Measurement precision - noise level

The precision of the discrete measurements is determined to be better than 0.1‰ for δ^{18}O and 0.5‰ for δD, as mentioned in detail in Section 2.4. For the continuous flow measurements, a first-hand estimation of the precision can be obtained by looking into the deviation of the water standards measured for the calibration. It shows that the overall precision is about 0.2‰ for δ^{18}O and 0.8‰ for δD (Table 3.1).

Another way to obtain the precision is to estimate the noise level of the measurements from the spectral analysis of the time series. Here the Maximum Entropy Method (MEM) for spectral analysis is implemented (see Appendix A for more on MEM). A fast algorithm for calculating the coefficients of MEM is introduced by Andersen (1974) and is applied here for running calculations on computer. The standard deviation of the time series based on one-side calculation is defined as:

$$\sigma^2 = \int_0^{f_c} \mid \hat{\eta}(f) \mid^2 \mathrm{d}f \tag{4.1}$$

where f_c is the Nyquist frequency which is determined by the sampling step, and $\mid \hat{\eta}(f) \mid^2$ can be estimated by a linear fit on the high frequency part of the spectrum (Figure 4.1, 4.2).

The time series is required to be sampled at a uniform period of step Δt in order to apply MEM. Here an uniform depth step Δd is used instead of the time step Δt. Thus the unit of frequency becomes [cycles/m] instead of [cycles/year]. Δd is estimated from the depth scale resolution. For the discrete measurements, Δd is fixed to be 0.05 m. For the continuous flow measurements, Δd is depending on the melting speed and the recording time step of spectrometer. An overall average of all the sampling intervals is $\sim$0.005 m. Thus, to acquire a time series with uniform sampling step, the data from continuous flow measurements were interpolated into a new-built depth scale with an uniform sampling

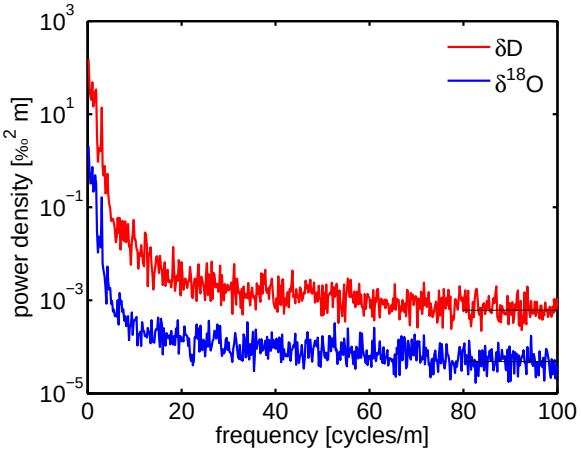

Figure 4.1: δ^{18}O and δD power spectra density (using MEM) for the continuous flow measurements. Noise level is estimated by a linear fit (black line) on the high frequency part of the spectrum ($f \geq 80$). The uniform depth step is $\Delta d = 0.005$ m, and the order for MEM is $m = 1500$. The estimated deviations are: $\sigma_{18} \approx 0.07‰$, $\sigma_D \approx 0.25‰$.

step, $\Delta d = 0.005$ m. Before interpolating, the missing data due to the ice breaks and cut ends were partly given by the 5 cm discrete measurements at the same depth.

The annual layer thickness (λ) changes notably (from 0.58 m to 0.07 m) for the NEGIS firn core (see Figure 2.4) due to the densification process. The power spectral density for the whole core will also generate peaks at the frequencies that correspond to those different annual layer thicknesses. The frequencies vary mostly from 2 to 10 [cycles/m], thus are within the Nyquist frequency intervals ($f_c = 10$ cycles/m for a sampling step of 0.05 m and $f_c = 100$ cycles/m for 0.005 m). That is to say, the power spectral density will also reflect the noise information from the variation of annual layer thickness; the effect is unavoidable and will be distinct with a sampling step comparable to the annual layer thickness variation. Therefore the noise level, which is the measurement noise plus the noise from annual layer thickness variation, will become larger. Hence, to estimate the measurement noise level more reliably for the discrete measurements, analyzing an interval with an overall constant annual layer thickness will be a better choice.

Figure 4.1 and 4.2 shows the results of spectra analysis using MEM for the continuous flow and the discrete measurements respectively. For the continuous one, MEM is applied to the whole core. For the discrete one, MEM is also applied to two intervals, 20 - 40 m and 46 - 66.3 m, where the annual layer thickness is more constant.

Overall, the estimates from MEM power spectra analysis show that: the precision for the continuous flow measurements is about 0.07‰ for δ^{18}O and 0.25‰ for δD; the precision for discrete measurements is better than 0.05‰ for δ^{18}O and 0.23‰ for δD. The result shows that the continuous flow measurements have a precision level close to that of the discrete measurements.

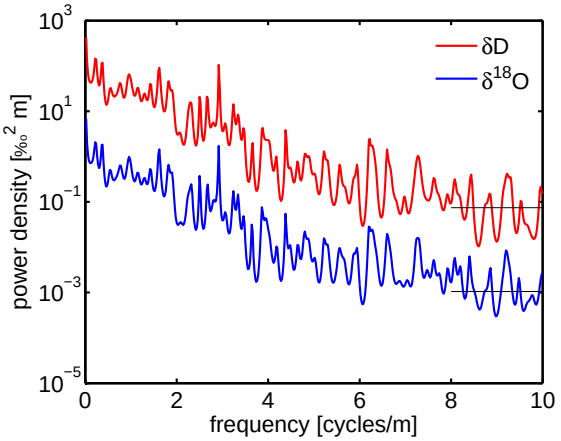

(a) Discrete: 0 - 66.3 m. $\lambda = 0.16 \pm 0.07[1\sigma]$ m
$\Delta d = 0.05$ m , $m = 150$
$f \geq 8$: $\sigma_{18} \approx 0.10‰$, $\sigma_D \approx 0.86‰$

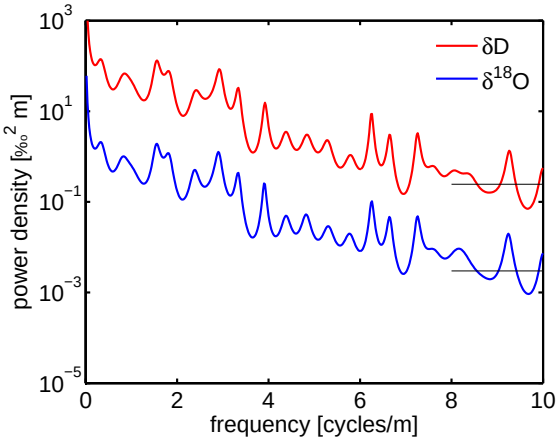

(b) Discrete: 0 - 20 m. $\lambda = 0.23 \pm 0.09[1\sigma]$ m
$\Delta d = 0.05$ m , $m = 50$
$f \geq 8$: $\sigma_{18} \approx 0.17‰$, $\sigma_D \approx 1.57‰$

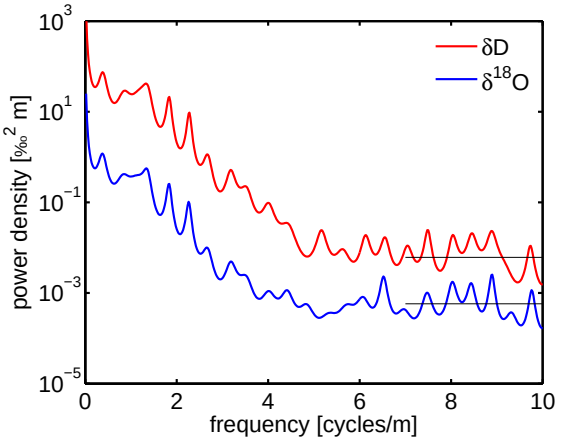

(c) Discrete: 20 - 40 m. $\lambda = 0.17 \pm 0.03[1\sigma]$ m
$\Delta d = 0.05$ m, $m = 50$
$f \geq 7$: $\sigma_{18} \approx 0.08‰$, $\sigma_D \approx 0.25‰$

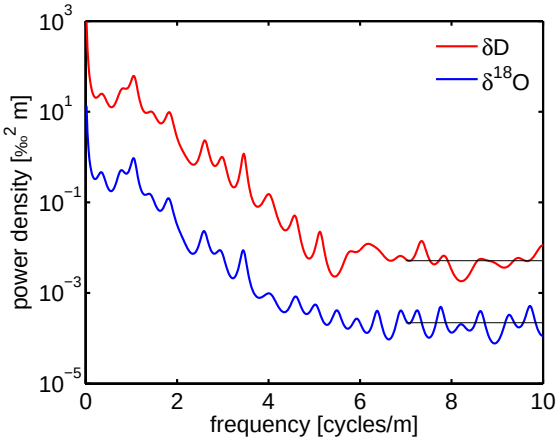

(d) Discrete: 46 - 66 m. $\lambda = 0.12 \pm 0.02[1\sigma]$ m
$\Delta d = 0.05$ m, $m = 200$
$f \geq 7$: $\sigma_{18} \approx 0.05‰$, $\sigma_D \approx 0.23‰$

Figure 4.2: δ^{18}O and δD power spectra density (using MEM) for the discrete measurements. Noise level is estimated by a linear fit (black line) on the high frequency part of the spectrum ($f \geq 8$ or $f \geq 7$). The y-axis scales are set the same. A comparison of (b), (c), and (d) shows the decrease of the noise level (and the increasing diffusion effect as well, see Section 5.2).

4.2 Measurement resolution

The resolution for the discrete measurements is determined to be 5 cm due to its way of sampling. In discrete mode, the firn core is cut into 5 cm sections and each section is melted and measured as one isotopic signal. Diffusion takes place during sample preparation and exists only within the 5 cm section. Diffusion does not exist through the experimental system, where the memory effects from previous analyses are taken account of.

For the continuous flow measurements, the firn core is continuously melted. Diffusion takes place all the way through the experimental setup: from the delivery in the tube, to the evaporation and mixing with dry air flow in the oven, and to the analysis in the cavity. Every signal in the continuous sample flow is smoothed when analyzed by the system. Thus a limit exists to the measuring resolution of the continuous flow mode.

To quantify the diffusion and to estimate the resolution of continuous flow measurements, the stepwise response approach is performed. This approach is to investigate the response of the experimental setup to a stepwise change in the water isotopic signal. Such a stepwise change can be found in the isotopic transitions during the switch between background water and sample water at valve V1 (Figure 3.2) for every bag measurement or during the switch between the water standards at V2 during the calibration. However, they account for slightly different diffusion processes due to the different water sample delivery path. Here the stepwise change from switching V1 is analyzed since it is from the real process of melting ice.

In the theoretical case of zero diffusion and memory effects, the change between two isotopic signals can be described by a scaled version of the Heaviside unit step function H(t) as:

$$\delta(t) = (C_2 - C_1)H(t) + C_1 \tag{4.2}$$

where $H(t) = \begin{cases} 0, & t < 0 \\ 1, & t \geq 0 \end{cases}$, C_1 and C_2 are the two water isotopic signals. The measured signal $\delta_m(t)$, which is smoothed by the diffusion, can be described as the convolution of $\delta(t)$ with a smoothing function G(t):

$$\delta_m(t) = (\delta * G)(t) = \int_{-\infty}^{\infty} \delta(\tau)G(t-\tau)\mathrm{d}\tau \tag{4.3}$$

Figure 4.3a shows the sample transition part from the beginning of sample bag 21. When the melting of the firn sample starts, the water isotopic signal drops from the CPH-DI background water to the firn sample. For the convenience of data fitting, the original data is reversed and normalized to 0 - 1 scale. As one has already noticed during the isotope data extraction in Section 3.2.3 that, the isotopic signal from the later coming water is generally more diffused compared to the previous one. It can also be seen here from both Figure 4.3a and 4.3b that a longer tail exists on the right side of the distribution. This could be explained as an effect from one-direction delivering, where the later coming water sample is driven from behind to the forth, hence more water could be pushed into the previous water. Due to the existed skewness, a cumulative distribution function (cdf) of a

lognormal distribution is chosen here to fit the normalized data (black line in Figure 4.3a):

$$\delta_{model} = \frac{1}{2} + \frac{1}{2} erf\left(\frac{ln(t) - \mu}{\sqrt{2}\sigma}\right) \tag{4.4}$$

The values of μ and σ are estimated by the least mean squares method.

The derivative of the measured signal $\frac{\delta m}{\mathrm{d}t}$ gives the response of the experimental setup to a scaled version of the δ_{Dirac} pulse:

$$\frac{\mathrm{d}\delta_m}{\mathrm{d}t} = \frac{\mathrm{d}\delta_m}{\mathrm{d}t} * G = (C_2 - C_1)\delta_{Dirac} * G \tag{4.5}$$

The response of the system to a δ_{Dirac} pulse, i.e. the derivative of the normalized step response as well as the derivative of cdf fit is shown in Figure 4.3b.

To visualize the temporal resolution of the system, the ratio $\frac{S_t}{S_{t=0}}$ is calculated for $t \geq 0$ (Figure 4.3c), considering that the impulse occurs at $t = 0$. One can see that the effect of the δ_{Dirac} pulse on the measured signal is below 20% after 40 s of its introduction. Beyond the point of 40 s, the effect from the impulse comes to the level comparable to the measurement noise. Therefore, the optimal temporal resolution of the system is set to be 40 s. Considering an overall melting speed of 4.4 cm/min for this part of the firn core, the spatial resolution of the system is estimated to be ∼2.93 cm.

While the normalized impulse response is modeled by a lognormal cdf fit to account for the skewness here, it can also be well approximated by the cdf of a Gaussian (normal) distribution function. A forward Gaussian cdf fitting based on the same dataset is failed due to the apparent unsymmetry of the distribution shape. However, it fits well with a Gaussian cdf model where the values of mean and standard deviation are estimated from the lognormal cdf fit[1] (red curves in Figure 4.3). Therefore, the impulse response of the system can be well approximated by a Gaussian type filter described as:

$$G(t) = \frac{1}{\sigma_{cfa}\sqrt{2\pi}} e^{-\frac{t^2}{2\sigma_{cfa}^2}} \tag{4.6}$$

where $\sigma_{cfa} = 18.52 \pm 0.44$ s $[1\sigma]$ is the diffusion length term (in unit of time) and is calculated with the least mean squares method. Considering an overall melting speed of 4.4 cm/min for this part of the firn core, the diffusion length of the system will be $\sim 1.36 \pm 0.032$ cm $[1\sigma]$.

[1]The mean and standard deviation of the variable are calculated as:

$$mean = e^{\mu + \frac{\sigma^2}{2}},$$

$$std = (e^{\sigma^2} - 1)e^{2\mu + \sigma^2},$$

where μ and σ are the mean and standard deviation of the variable's natural logarithm and can be obtained from the lognormal cdf fit.

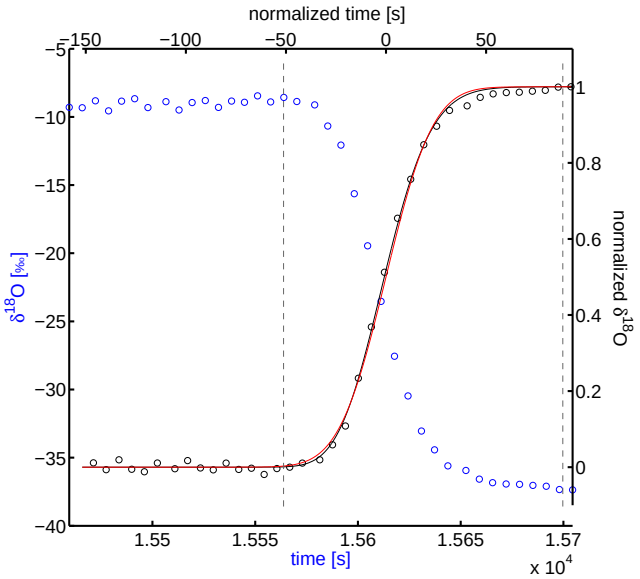

(a) Original (blue circle) and normalized (black circle) response to a stepwise change of isotopic signal.

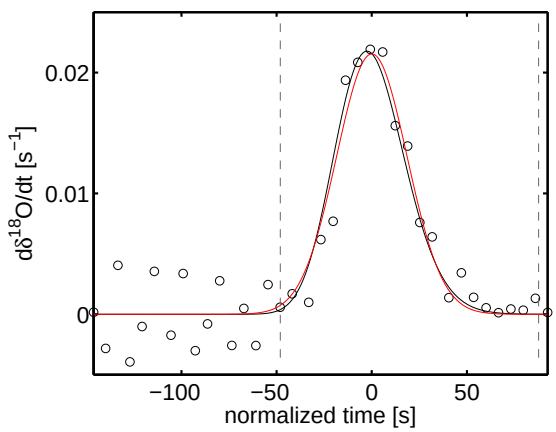

(b) The derivative of the normalized step response and of the corresponding cdf fit.

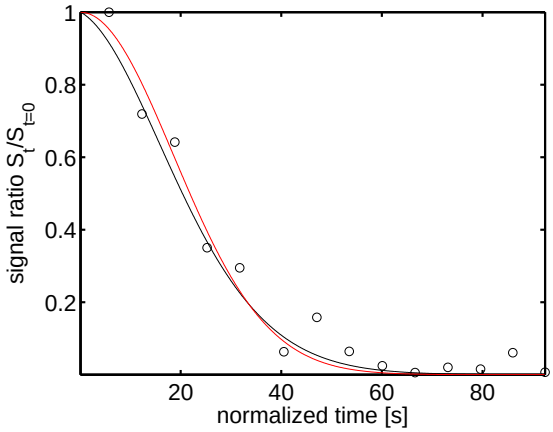

(c) The ratio of signal amplitude S_t at time t and the impulse amplitude $S_{t=0}$.

Figure 4.3: Analysis of the stepwise response of the analytical system. All the x axes are with respect to the measurement time. Black circles represent the normalized raw data. Dashed vertical lines indicate the data interval used for fitting. Black curves correspond to the lognormal cdf fit. Red curves are the Gaussian cdf model, where the values of mean and standard deviation are estimated from lognormal cdf fit.

Both the lognormal and the Gaussian distribution function well fit the impulse of the system. In the following, the Gaussian filter approximation will be applied since it has a significant advantage to simplify the diffusion process as well as the subsequent calculations.

It should be noted that the step response approach is based on the signal step introduced from the switching of valve V1. Thus it only accounts for the smoothing that takes place in the analysis system, while the smoothing that takes place in the melting system and the debubbler unit from the upstream is excluded (see Figure 3.2). This step response approach has been followed in the past to estimate the resolution of the CFA chemistry measurements and its shortage has been discussed as well (Sigg et al. 1994; Rasmussen et al. 2005).

4.3 Results agreement

There exist a difference between the results from discrete measurements and those from continuous flow measurements. And there could be many factors that have contributed to this difference. A main contributor that first comes to one's mind would be the calibration. Due to the different measuring modes, the calibration was done separately for each measurement run during the discrete measurements, while only two times of calibration were applied throughout the continuous flow measurements.

The parameters, including water concentration, measured values of the standards, slope and intercept of the calibration line, and the offset of "NEEM" (between expected value and calibrated value), are averaged for every measurement run in the discrete measurements. Water concentration for the discrete measurements are not calibrated to 20,000 ppmv, but rather to be kept in a range of 19,000 - 20,500 ppmv. The measured values of the three standards vary from one run to another. The calibration line based on these standards has different slopes and intercepts, and has been applied to calibrate each run.

All of the above factors that vary for each discrete measurement run, however, have a constant value applied to the whole continuous flow measurements. Due to the different calibration processes, it would not be a surprise when the results from these two different measuring modes come out with a difference. On one hand, one would suspect that one of the calibrations from the discrete measurements was not carried out properly, in which case, the local difference would be explained by the distinct change of the parameters. On the other hand, if one could hardly observe an evident correlation between the differences of the results and the variations of the parameters, there would be a big possibility that the problem is located in the two calibrations of the continuous flow measurements.

All the parameters for discrete measurement runs are presented in Figure 4.4 together with the differences of the isotopic signals between the two results. To be more convincing, the results from continuous flow measurements are averaged in the same 5 cm intervals as that of the discrete samples. Figure 4.4 shows that variations of the parameters do exist and sometimes the variations are even significant. For instance, both "NEEM" offset and the intercept of calibration line drop significantly at run 3; the δ^{18}O jumped to a higher level while the δD had a big drop at run 7; and the significant drop of the δ^{18}O only at

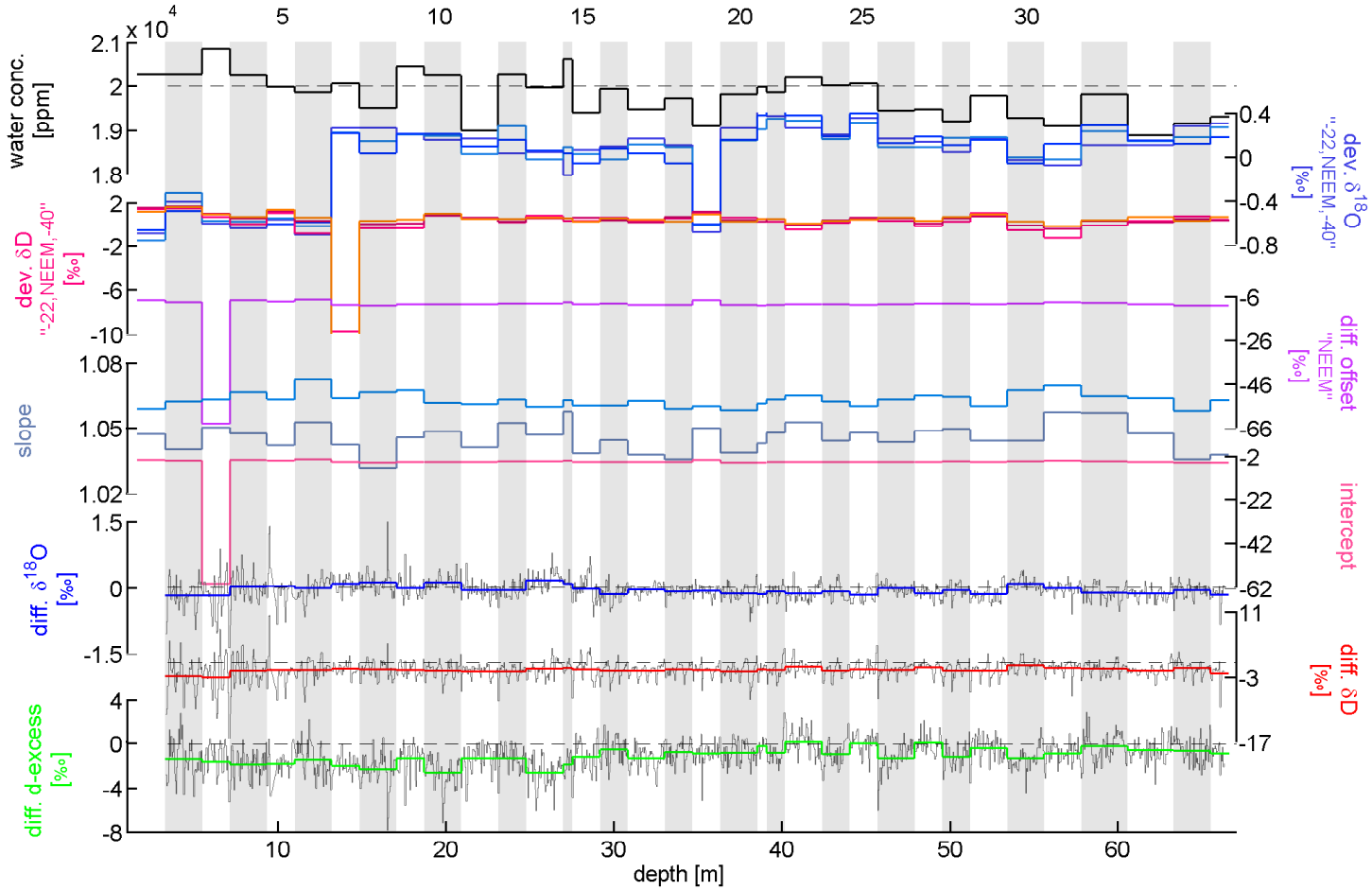

Figure 4.4: Differences between the discrete measurements and the 5-cm averaged CFA measurements of the whole NEGIS core. The parameters for discrete measurements are averaged for every measurement run. Here "diff." is defined as the difference between the discrete record and the corresponding CFA record, e.g., diff.$\delta D = \delta D_{discrete} - \delta D_{CFA}$. "dev." is defined as the deviation of the measured isotopic signal (before calibration), e.g., dev.$\delta D = \delta D - \bar{\delta D}$. Dotted lines indicate the zero values level (except 20,000 ppm for water concentration).

run 19.

However, it is hard to observe apparent correlations between the variations of these parameters and the differences of the signals. The δ^{18}O from continuous flow measurements show an overall higher value except at the depth of ∼18 - 28 m. The δD from continuous flow measurements show an higher value all through the measurements. The deuterium excess, which is closely related to the variation of δD, shows a similar plot as δD. The large variations of all three isotopic signals above ∼10 m probably due to the poor quality of the melting for the top part of the firn core by CFA system. The relative standard deviation (RSD) [2] can serve as a measure of quality assurance. The RSD values for δ^{18}O, δD, and deuterium excess are 0.65%, 0.88%, and 19.24%, respectively, which reveals a relative big difference of the deuterium excess signals.

The differences between the results can be easily illustrated on a cluster plot. Figure 4.5 shows that most of the δD and deuterium excess results from continuous flow measurements shift to higher values. It strongly suggests the differences between the two results are caused by a global error. A plot of the relationship between the δD and $\delta^{18}O$ signals from both measurements confirms this suggestion. The average relationship between the δD and $\delta^{18}O$ in natural meteoric waters which have not undergone excessive evaporation is given by:

$$\delta D = 8\ \delta^{18}O + 10,$$

which is the so-called Global Meteoric Water Line (Craig 1961) and is referred as a baseline of global precipitation. The annual precipitation at high latitude in the Northern hemisphere has been observed that it fits the meteoric line Dansgaard (1964). Figure 4.5d shows the δD-δ^{18}O relationship based on the continuous flow measurement results has an apparent shift from the baseline, which means the results may not accurately reflect the true precipitation signal. The error is probably induced from the two calibrations of continuous flow measurements. Even though the performance of the spectrometer is rather stable through the 28 days of measurements, the comparison has suggested that, the instrumental drifts still remain significant effects on the calibrations.

The instrumental drifts can be seen on the power spectrum by comparing the noise level of δD and δ^{18}O signals. The power spectral density of both measurements from using MEM is shown in Figure 4.6. The data from continuous flow measurements are averaged for each 5 cm, in the same resolution with that of the discrete samples. Three depth intervals from surface to the firn core bottom are presented. The relative flat high frequency part

[2]The relative standard deviation (RSD) is the absolute value of the coefficient of variation and is often given as a percentage:

$$RSD = \left|\frac{s}{\bar{x}}\right| \cdot 100\%,$$

where s is standard deviation σ for one data set or root mean square deviation (RMSD) of two data sets. RMSD is defined as:

$$RMSD = \sqrt{\frac{\sum_{n=1}^{N}(x_{1,n} - x_{2,n})^2}{N}}.$$

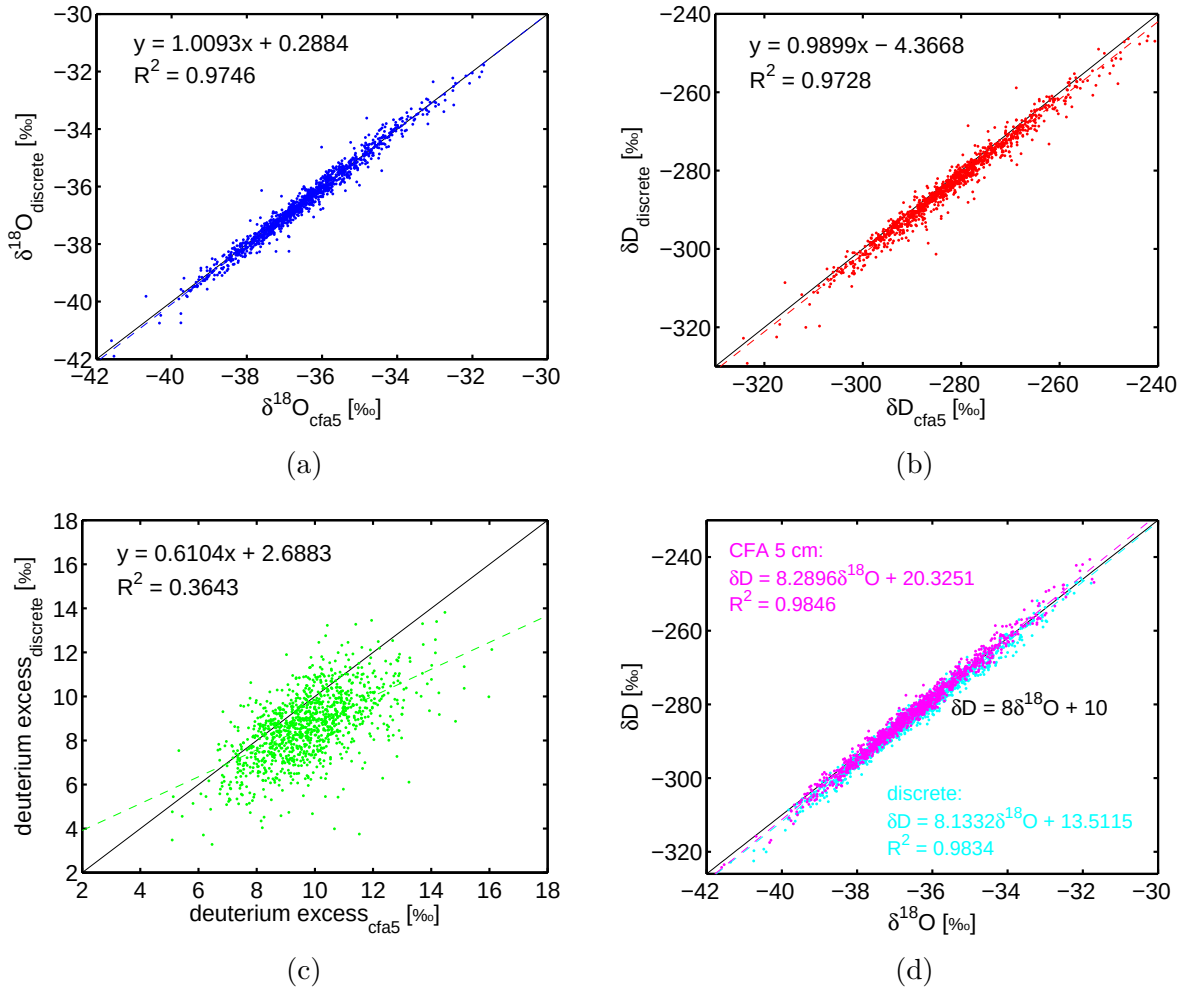

Figure 4.5: Comparison of the results from the discrete measurements and the 5-cm averaged CFA measurements. Black lines on plot (a), (b), and (c) indicate the identity line: y = x. Black line on plot (d) indicates the Global Meteoric Water Line. Color dashed lines indicate the linear fit of the data.

of the power spectrum is regarded as the measurement noise. The depth reflects the time of the measurement, since the melting of the firn core starts from surface and ends at the bottom. As time goes by, an apparent increase of the noise level for the continuous flow measurements has been observed, especially in the case of δD signals. [3]

The discrete measurements perform calibration each time the spectrometer measures samples. The instrumental drifts thus stay at a negligible level. However, in the case of continuous flow measurements, no calibrations have been conducted during the whole measurements of 28 days. Instrumental drifts can thus arise to an notable level after a long running term. Though the results show an general good agreement, the increased noise caused by instrumental drifts will somehow limit our confidence to acquire an accurate interpretation on the signals.

[3]The data analysis has revealed a different response of the δD and δ^{18}O to the drifts. This may be considered an interesting phenomenon in other relative studies, e.g. techniques to improve the performance of spectrometer in the future.

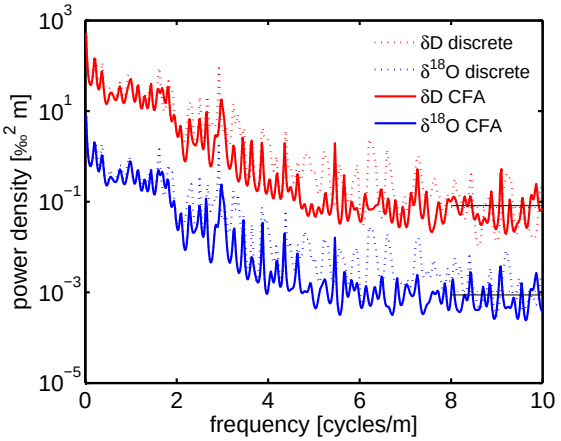

(a) NEGIS: 0-66.3 m
Discrete: $\sigma_{18} \approx 0.10‰$, $\sigma_D \approx 0.86‰$
5-cm CFA: $\sigma_{18} \approx 0.09‰$, $\sigma_D \approx 0.9‰$

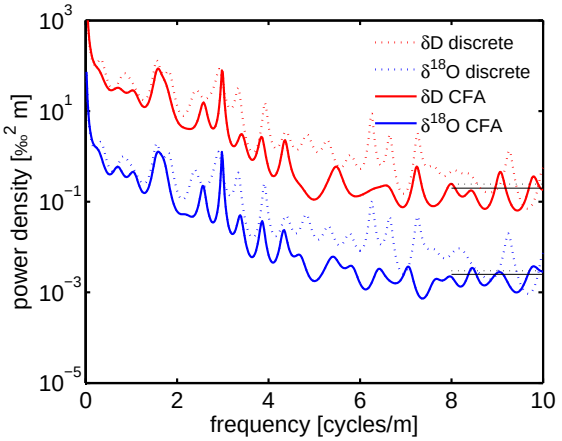

(b) Discrete: 0-20 m
Discrete: $\sigma_{18} \approx 0.17‰$, $\sigma_D \approx 1.57‰$
5-cm CFA: $\sigma_{18} \approx 0.16‰$, $\sigma_D \approx 1.41‰$

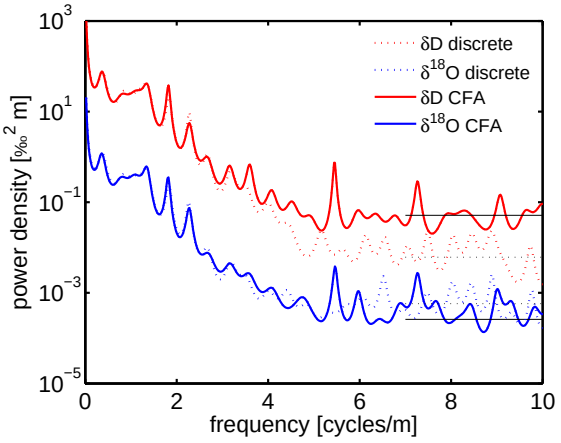

(c) Discrete: 20-40 m
Discrete: $\sigma_{18} \approx 0.08‰$, $\sigma_D \approx 0.25‰$
5-cm CFA: $\sigma_{18} \approx 0.05‰$, $\sigma_D \approx 0.72‰$

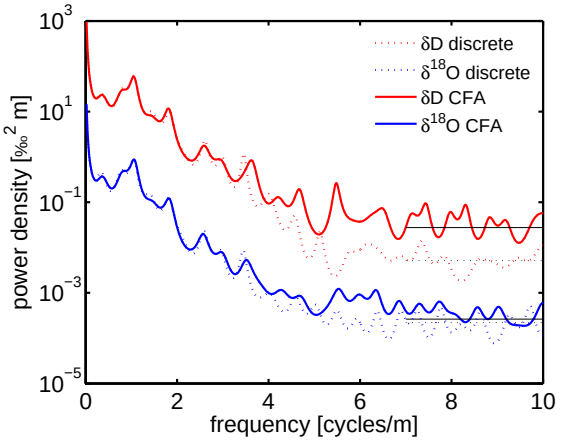

(d) Discrete: 46-66 m
Discrete: $\sigma_{18} \approx 0.05‰$, $\sigma_D \approx 0.23‰$
5-cm CFA: $\sigma_{18} \approx 0.05‰$, $\sigma_D \approx 0.53‰$

Figure 4.6: Comparison of δ^{18}O and δD power spectra density (using MEM) for the discrete and the continuous flow measurements. All the used parameters are the same as described in Figure 4.2. The δ signals from continuous flow measurements (CFA) are averaged in 5 cm. The power spectrum shows that the noise level of δD signals from the continuous measurements becomes apparently higher below 20 m compared to that of the discrete, while the noise level of δ^{18}O signals generally stays comparable to that of the discrete.

Chapter 5

Stable Isotope Diffusion

Water isotope signals are significantly smoothed by diffusion process after snow deposition. After deposition, the snow is transformed into firn and compressed to ice through a densification process that gradually reduces the thickness of the annual layers. Before reaching the density where the pores are closed off, substantial mixing of water vapor molecules takes place via the open pores between the ice grains. Exchange of water vapor molecules with the local ice matrix also takes place but is a slower process. Figure 5.1 illustrates all the potential molecular mixing that could take place in the firn. The water isotope signals will be affected both by the compression and the smoothing caused by the mixing and exchange of water vapor molecules. The annual cycles are attenuated and can disappear entirely. For the NEGIS firn core, the δ^{18}O annual cycles are observed for the top $\sim$8 m of the core only. Below the firn layers, diffusion in solid ice, which depends on ice flow and the diffusivity of the solid ice, continues to smooth the remaining isotope signals but with a general weaker effect. The diffusion in solid ice will not be discussed here since the NEGIS core is a firn core.

5.1 Firn diffusion model

Models of firn diffusion that assume the mixing of water molecules in the vapor phase as the dominant diffusion process have been widely developed (Johnsen 1977; Whillans and Grootes 1985; Cuffey and Steig 1998; Johnsen et al. 1999, 2000). The formulation of the diffusion modelling here is based on the work presented in Johnsen (1977) and Johnsen et al. (2000).

The diffusion process is driven by isotopic gradients vertically along the firn layers. Assuming a coordinate system with a vertical z-axis and an origin that follows a sinking horizontal layer, the smoothing of the isotopic signals with time can be described as:

$$\frac{\partial \delta}{\partial t} = \Omega(t)\frac{\partial^2 \delta}{\partial z^2} - \dot{\varepsilon}_z(t) z \frac{\partial \delta}{\partial z} \tag{5.1}$$

where $w(t)$ is the diffusivity coefficient depending on temperature and firn density, $\dot{\varepsilon}_z(t)$ is the vertical strain rate which is assumed to be uniform within the firn layer. On the

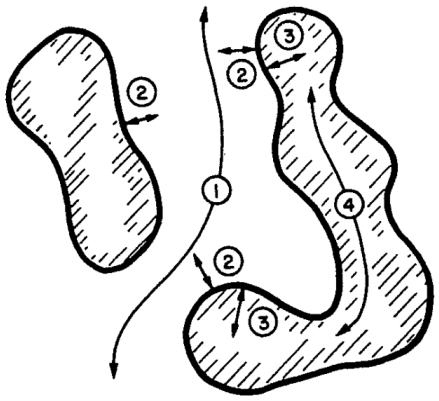

Figure 5.1: Ice grains and pore space, showing potential molecular pathways: ① vapor-vapor; ② vapor-ice surface; ③ ice surface-ice interior; ④ through ice matrix. Isotopic diffusion is dominated by ①, ②, and ③ acting together (figure from Whillans and Grootes (1985)).

right side of the equation, the first term represents the diffusion effect according to Fick's second law; the second term is added to take account of the effect from both compression ($-\dot{\varepsilon}_z(t)z$) and advection ($\frac{\partial\delta}{\partial z}$).

The solution of equation (5.1) will give the measured isotopic signal at depth z and time t as:

$$\delta(z,t) = \frac{1}{\sigma\sqrt{2\pi}} \int_{-\infty}^{\infty} \delta\left(z' e^{-\int_0^t \dot{\varepsilon}_z(\tau)\mathrm{d}\tau}, 0\right) e^{-\frac{(z-z')^2}{2\sigma^2}} \mathrm{d}z' \tag{5.2}$$

where $\delta(z',0)$ is the original isotopic signal at the time when the precipitation just deposited; and $z'e^{-\int_0^t \dot{\varepsilon}_z(\tau)\mathrm{d}\tau}$ accounts for the vertical compression of the original signal during the time period t.

As demonstrated by equation (5.2), the effect of diffusion is mathematically equivalent to a convolution of the initial isotopic signal $\delta(z',0)$ (taking the compression into consideration as well) with a Gaussian filter: $G(z) = \frac{1}{\sigma\sqrt{2\pi}} e^{-\frac{z^2}{2\sigma^2}}$. That is to say, the smoothed isotopic signal $\delta(z,t)$ at depth z is a weighted integration result of its ambient isotopic signal with a weight that is Gaussian distributed corresponding to the distance on both sides of depth z. The knowledge of the Gaussian filter has an importance in restoring the original isotopic profile. Once σ is known, a deconvolution filter can in theory be designed to apply on the smoothed isotopic signal and to restore the original one.

The standard deviation term σ of the Gaussian filter is introduced as the diffusion length to describe the smoothing effect. The diffusion length indicates the mean displacement of the water molecules in the vertical direction and is determined by the equation (Johnsen 1977):

$$\frac{\mathrm{d}\sigma^2}{\mathrm{d}t} - 2\dot{\varepsilon}_z(t)\sigma^2 = 2\Omega(t) \tag{5.3}$$

where the term $2\dot{\varepsilon}_z(t)\sigma^2$ accounts for the densification and ice flow and the term $2\Omega(t)$

accounts for the diffusive properties of the firn.

In order to solve equation (5.3), the vertical strain rate $\dot{\varepsilon}_z(t)$ and the diffusivity $\Omega(t)$ need to be known. Models of densification and ice flow are required and the deviations will be briefly introduced in the following. The deviation will follow the methodology of Vinther (2003), but give more details and emphasize results for the NEGIS firn core.

5.1.1 Firn densification

The transform of the precipitated snow into solid ice can be divided into three stages (Herron and Langway 1980). The first stage is from the initial snow density to a "critical density" of ∼550 kg/m^3. The densification rate is usually the most rapid and the mechanism is considered to be grain settling and packing. At this stage, the snow has been transformed into firn. The second stage is from the "critical density" until the interconnected air passages are closed off at a density of ∼804.3 kg/m^3.[1] At this stage, the firn has been transformed into ice. The third stage is below the pore-close-off zone, where the air bubbles captured in the ice can no longer be excluded and will be compressed until reaching the final density of ∼917 kg/m^3.

A semi-empirical model for the first two stages presented by Herron and Langway (1980) and slighted modified by Johnsen et al. (2000) will be used here. The model is based on the suggestion that in the firn densification the proportional change in air space is linearly related to the change in stress due to the weight of overlying snow. According to Schytt (1958), the general relation between depth (z) and density (ρ) is expressed as:

$$\frac{\mathrm{d}\rho}{\mathrm{d}z} = K\rho(\rho_i - \rho) \tag{5.4}$$

where K is a constant depending on temperature and accumulation rate at a given location and $\rho_i = 917$ kg/m^3 is the density of ice.

Using the data from multiple polar ice cores, Herron and Langway (1980) found an empirical expression as[2]:

$$\frac{\mathrm{d}\rho}{\mathrm{d}z} = \begin{cases} \dfrac{r}{\rho_i} \cdot k_0 A^{a-1}\rho(\rho_i - \rho), & \rho \le \rho_c \\ \dfrac{r^{\frac{1}{2}}}{\rho_i} \cdot k_1 A^{b-1}\rho(\rho_i - \rho), & \rho_c < \rho \le \rho_m \end{cases} \tag{5.6}$$

[1] The density at which the pore is closed off is 820 - 840 kg/m^3 according to Herron and Langway (1980). Here it is modified to be ∼804.3 kg/m^3, based on the calculation of tortuosity factor τ (see Section 5.1.4).

[2] In the paper of Herron and Langway (1980), the expression for densification rate is presented:

$$\frac{\mathrm{d}\rho}{\mathrm{d}t} = \begin{cases} k_0 A_w^a(\rho_i - \rho), & \rho \le \rho_c \\ k_1 A_w^b(\rho_i - \rho), & \rho_c < \rho \le \rho_m \end{cases} \tag{5.5}$$

where A_w is the accumulation rate in meters of water equivalent used by Herron and Langway (1980). The expression for $\frac{\mathrm{d}\rho}{\mathrm{d}z}$ in the thesis is obtained by rearranging the equation above with substitution $\frac{\mathrm{d}z}{\mathrm{d}t} = \frac{A\rho_i}{\rho}$ and $A_w = \frac{A\rho_i}{\rho_w}$, where A is the accumulation rate in meters of ice equivalent used in the thesis.

where $r = \frac{\rho_i}{\rho_w} = 0.917$; $\rho_c = 550$ kg/m^3 is the "critical density"; $\rho_m = 800$ kg/m^3 is the maximum density where Herron and Langway (1980) found the model in good agreement with observations. K is represented by k and A: A is the accumulation rate in meters of ice equivalent with a and b determined to be 1 and 0.5, respectively; k_0 and k_1 are Arrhenius-type rate constants depending only on local temperature T (in kelvin):

$$\begin{cases} k_0 = f_0 \cdot 11 \cdot e^{-\frac{10160}{RT}} \\ k_1 = f_1 \cdot 575 \cdot e^{-\frac{21400}{RT}} \end{cases} \tag{5.7}$$

where R is the gas constant (8.314 J mol$^{-1}K^{-1}$); f_0, f_1 are scaling factors introduced by Johnsen et al. (2000) in order to better fit the observed central Greenland density profiles ($f_0 = 0.85, f_1 = 1.15$ are used for central Greenland density profiles in Johnsen et al. (2000)). For the NEGIS firn core, $f_0 = 1.0, f_1 = 0.9$ are chosen as the optimum values.

Integration of equation (5.6) gives the density profile as:

$$\rho = \begin{cases} \rho_i \dfrac{R_0 e^{rk_0 z}}{1 + R_0 e^{rk_0 z}}, & R_0 = \dfrac{\rho_0}{\rho_i - \rho_0}, \quad \rho \le \rho_c \\ \rho_i \dfrac{R_c e^{r^{\frac{1}{2}} k_1 A^{-\frac{1}{2}} (z - z_c)}}{1 + R_c e^{r^{\frac{1}{2}} k_1 A^{-\frac{1}{2}} (z - z_c)}}, & R_c = \dfrac{\rho_c}{\rho_i - \rho_c}, \quad \rho > \rho_c \end{cases} \tag{5.8}$$

Here the upper bound of ρ_m is neglected because the maximum density for the NEGIS firn core is only 834.8 kg/m^3 and also that Vinther (2003) found the approximation could be used for densities larger than ρ_m as well. z_c is the depth at which $\rho = \rho_c$. z_c can be found from the density profile for $\rho \le \rho_c$ as:

$$z_c = \frac{1}{rk_0} ln \left(\frac{\rho_c(\rho_i - \rho_0)}{\rho_0(\rho_i - \rho_c)} \right) \tag{5.9}$$

The density model requires only three parameters: the mean annual temperature T (to determine k_0, k_1), annual accumulation rate A, and the initial (surface) snow density ρ_0.

For the annual mean temperature of the NEGIS drilling site, no direct available record is found. As a solution, the temperature is estimated from the temperature record of the NGRIP ice core drilling site, which locates approximately 150 km west of NEGIS drilling site and has an annual mean temperature of -31.5 °C (NGRIP members 2004). The elevation of the NEGIS and NGRIP drilling site is ∼2700 m and 2917 m, respectively. According to a general lapse rate of 0.6 °C/100 m, $T \approx -30$ °C for NEGIS drilling site is determined to be a reasonable estimate.

Figure 5.2 shows the measured and modeled density profile for the NEGIS firn core. With a measured surface density $\rho_0 = 300$ kg/m^3 around depth of 2 m, and an averaged annual mean accumulation rate $A = 0.11$ m i.e., the densification model is shown to be in good agreement with the observed data.

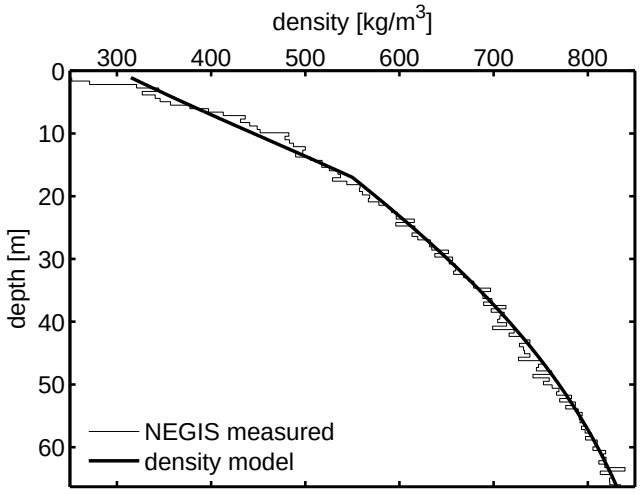

Figure 5.2: Measured and modeled density profiles for the NEGIS firn core. The parameters used for the density model are: $T = -30$ °C, $A = 0.11$ m i.e., $\rho_0 = 300$ kg/m^3.

5.1.2 Ice flow model

Simple models for ice flow in an ice sheet have been developed (Nye 1963; Dansgaard and Johnsen 1969). The flow is simplified to be two-dimensional and the ice sheet is considered to be in a steady state (the ice sheet thickness does not change with time). The basic assumption behind the model is that the horizontal velocity of the ice can be considered constant from the surface and down to a certain depth, and that it from there on decreases linearly with depth. The model is usually named "kink" model due to the shape of the horizontal velocity profile (or "D-J" model after Dansgaard and Johnsen (1969)).

The "kink" model with basal melting and sliding is illustrated in Figure 5.3. The horizontal velocity can be expressed as:

$$u(z) = \begin{cases} U \cdot x, & 0 \leq z \leq H - h \\ \left(1 - \dfrac{(z - H + h)(1 - f_b)}{h}\right) \cdot U \cdot x, & H - h < z \leq H \end{cases} \tag{5.10}$$

where u is the horizontal velocity, U constant, and x the distance from the ice divide; z is the depth with origin from the surface; H is the ice sheet height, h the "kink-height", and thus $H - h$ the "kink-depth", which is typically more than 1500 m; f_b is defined as the ratio between the bottom sliding velocity and the surface velocity, thus the bottom sliding velocity is equal to $f_b \cdot U \cdot x$.

The constant U is dependent on the model input and needs to be derived here. According to the ice sheet mass balance, in a steady state the ice accumulation must be equal to

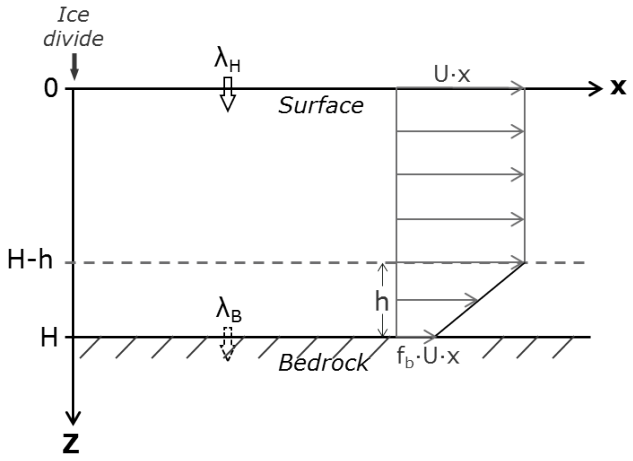

Figure 5.3: Schematic description of the ice flow model, with basal melting and sliding. λ_H is accumulation rate, and λ_B bottom melting rate.

the horizontal mass transport driven by the ice flow:

$$\begin{aligned}(\lambda_H - \lambda_B)x &= \int_0^H u(z)\frac{\rho}{\rho_i}\mathrm{d}z \\ &= \int_0^{H-h} Ux\frac{\rho}{\rho_i}\mathrm{d}z + \int_{H-h}^{H}\left(1 - \frac{(z-H+h)(1-f_b)}{h}\right)Ux\mathrm{d}z\end{aligned} \tag{5.11}$$

where λ_H is accumulation rate, and λ_B bottom melting rate; both of λ_H and λ_B are in meters of ice equivalent. The term $\frac{\rho}{\rho_i}$ is to take account of the densification process.

Letting H^* be the ice thickness in meters of ice equivalent and z^* the depth in meters of ice equivalent[3], equation (5.11) becomes:

$$(\lambda_H - \lambda_B)x = \int_0^{H^*-h} Ux\mathrm{d}z^* + \int_{H^*-h}^{H^*}\left(1 - \frac{(z^*-H^*+h)(1-f_b)}{h}\right)Ux\mathrm{d}z^* \tag{5.12}$$

Carrying out the integration and separating the term U, we will get:

$$U = \frac{\lambda_H}{H_e}, \qquad H_e = \frac{\lambda_H}{\lambda_H - \lambda_B}\left(H^* - \frac{h}{2}(1-f_b)\right), \tag{5.13}$$

where H_e is referred to as the effective ice thickness, the depth where the vertical velocity reaches zero if it was calculated with the constant horizontal velocity $U \cdot x$ all the way down through the ice sheet.[4]

[3] $H^* = \frac{1}{\rho_i}\int_0^H \rho(z)\mathrm{d}z;\ z^* = \frac{1}{\rho_i}\int_0^z \rho(z)\mathrm{d}z.$

[4] Here parameters λ_B, h, and f_b are unknown. Their values are usually chosen so as to assign well-established age-depth features (Dansgaard et al. 1993). In order to proceed the model, here the values from NGRIP ice core are adopted. It should be noticed that they are very likely to be different. However, the constant U is a small value in magnitude of 10^{-5}, with no significant influence in the results of $\dot{\varepsilon}_z$ (equation (5.19)) and w (equation (5.21)). Actually, ice flow effect can be neglected to simplify the firn diffusion model (Gkinis 2011).

5.1.3 Vertical strain rate

The vertical strain rate $\dot{\varepsilon}_z$ can be derived from the ice flow model. The strain rate is generally defined as the derivative of the strain with respect to time:

$$\dot{\varepsilon}_z(t) = \frac{\mathrm{d}\varepsilon}{\mathrm{d}t} = \frac{\mathrm{d}}{\mathrm{d}t}\left(\frac{\lambda(t) - \lambda}{\lambda}\right) = \frac{\mathrm{d}\lambda(t)}{\lambda \mathrm{d}t} \tag{5.14}$$

where $\lambda(t)$ is the annual layer thickness in meters of ice equivalent at time t and λ the original layer thickness.

As the ice sheet is assumed to be steady, an annual layer of thickness λ will sink by exactly its own thickness λ every year:

$$\lambda = w \cdot \tau_0, \qquad \tau_0 = 1 \text{ yr} \tag{5.15}$$

where $w = \frac{\mathrm{d}z}{\mathrm{d}t}$ is the vertical velocity in the ice sheet. Substituting the above relation into equation (5.14), we get:

$$\dot{\varepsilon}_z = \frac{\mathrm{d}w}{w\mathrm{d}t} = \frac{\mathrm{d}w}{w\mathrm{d}z}\frac{\mathrm{d}z}{\mathrm{d}t} = \frac{\mathrm{d}w}{\mathrm{d}z} \tag{5.16}$$

Considering the continuity equation for the steady state, we will have:

$$\frac{\mathrm{d}(\rho u)}{\mathrm{d}x} + \frac{\mathrm{d}(\rho w)}{\mathrm{d}z} = 0 \tag{5.17}$$

where the density ρ is dependent on the depth z, but independent on the horizontal distance x. After rearrangement, we get:

$$\frac{\mathrm{d}w}{\mathrm{d}z} = -\frac{\mathrm{d}u}{\mathrm{d}x} - w\frac{\mathrm{d}\rho}{\rho \mathrm{d}z} \tag{5.18}$$

Substituting $w = \frac{\mathrm{d}z}{\mathrm{d}t}$ into the equation above and combining equation (5.16), the expression for vertical strain rate is derived as:

$$\dot{\varepsilon}_z = -\frac{\mathrm{d}u}{\mathrm{d}x} - \frac{\mathrm{d}\rho}{\rho \mathrm{d}t} \tag{5.19}$$

where the first term on the right side of equation (5.19) accounts for the thinning due to ice flow; and the second term accounts for the thinning due to densification. The two terms will be given by the ice flow model and the densification model, respectively.

The vertical velocity w of the ice sheet is related to the vertical strain rate. w can be obtained by solving the first order linear differential equation (5.18):

$$w(z) = e^{-\int_0^z \frac{\mathrm{d}\rho}{\rho \mathrm{d}z''}\mathrm{d}z''}\left(\int_0^z -\frac{\mathrm{d}u}{\mathrm{d}x} \cdot e^{\int_0^z \frac{\mathrm{d}\rho}{\rho \mathrm{d}z''}\mathrm{d}z''}\mathrm{d}z' + w_0\right) \tag{5.20}$$

where w_0 is the vertical velocity at the surface of the ice sheet and $w_0 = \frac{\rho_i A}{\rho_0}$ according to the steady state condition. Letting ρ_0 be the density at the surface of the ice sheet; substituting the horizontal velocity $u = U \cdot x$ for $z \leq H - h$, the depth-density relation $\frac{\mathrm{d}\rho}{\mathrm{d}z} = K\rho(\rho_i - \rho)$, $K = k_0, k_1 A^{-\frac{1}{2}}$, we will have w expressed in term of density ρ:

$$
\begin{aligned}
w(\rho) &= \frac{\rho_0}{\rho}\left(\int_{\rho_0}^{\rho} -\frac{U}{K\rho_0(\rho_i - \rho')}\mathrm{d}\rho' + w_0\right) \\
&= \begin{cases} \dfrac{U}{k_0\rho} ln\left(\dfrac{\rho - \rho_i}{\rho_0 - \rho_i}\right) + \dfrac{\rho_i A}{\rho}, & \rho \leq \rho_c \\ \dfrac{UA^{\frac{1}{2}}}{k_1\rho} ln\left(\dfrac{\rho - \rho_i}{\rho_c - \rho_i}\right) + \dfrac{U}{k_0\rho} ln\left(\dfrac{\rho_c - \rho_i}{\rho_0 - \rho_i}\right) + \dfrac{\rho_i A}{\rho}, & \rho > \rho_c \end{cases}
\end{aligned}
\tag{5.21}
$$

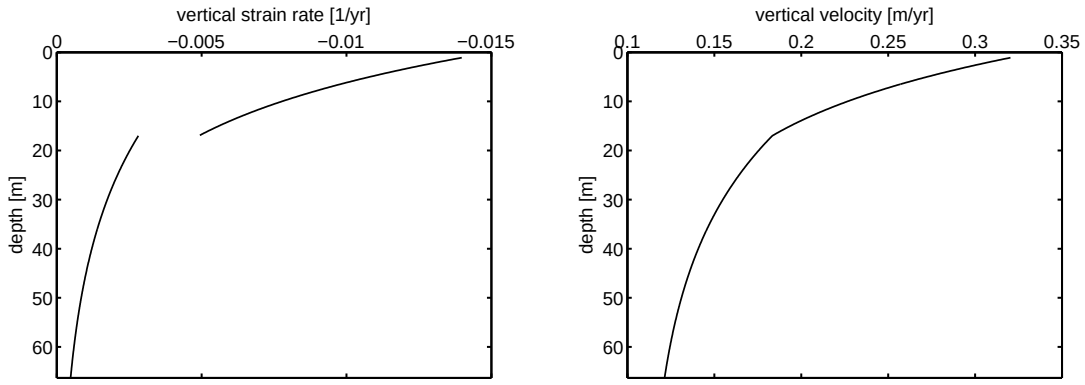

Figure 5.4: Profile of vertical strain rate ($\dot{\varepsilon}_z$) and vertical velocity (w) of the NEGIS firn core. Data calculated according to the densification model (equation (5.19)) and the ice flow model (equation (5.21)).

Figure 5.4 shows the calculated profile of vertical strain rate and vertical velocity of the NEGIS firn core. $\dot{\varepsilon}_z$ is negative since an annual layer becomes compressed with respect to time; its absolute value indicates the intention of the strain. According to the densification, when the snow is closer to the surface, it is easier to be compressed, and thus will correspond to a larger vertical strain rate and a larger vertical velocity. It can be seen from the profile in Figure 5.4 the densificaton model is able to explain this process. However, there is kink in the modeled profile, especially for the vertical strain rate. It reflects an artifact of the densification model, where the densification process is artificially separated into two stages above and below the point $\rho = \rho_c$. Due to the different empirical parameters of each stage, one may expect different values at the turning point.

5.1.4 Firn diffusivity

After the pores are closed off at a density $\rho_p \approx 804.3$ kg/m^3, diffusion through the interconnected air passages in the firn becomes impossible[5]. Before the pores are closed off, Johnsen et al. (2000) has derived the following expression for the firn diffusivity as a function of temperature and density (the index i hereafter indicates that the parameter is related to either of the heavy molecules $H_2^{18}O$ ($i = 18$) or $HD^{16}O$ ($i = D$)):

$$\Omega_i = \frac{\Omega_{ai}}{\tau} \cdot \frac{1}{\alpha_i} \cdot \frac{mp}{RT} \left(\frac{1}{\rho} - \frac{1}{\rho_i} \right), \quad \rho \leq \rho_p \tag{5.22}$$

Ω_a is the diffusivity of water vapor in air [m^2/yr][6] and is adopted from Hall and Pruppacher (1976):

$$\Omega_a = 665.41 \left(\frac{T}{T_0} \right)^{1.94} \left(\frac{P_0}{P} \right) \tag{5.23}$$

where T is the ambient temperature $[K]$ and P the ambient pressure [atm], $T_0 = 273.15$ K and $P_0 = 1$ atm. For the heavy isotopic water species in air, the diffusivity are given from Merlivat and Jouzel (1979) as: $\begin{cases} \Omega_{a18} = \Omega_a / 1.0251 \\ \Omega_{aD} = \Omega_a / 1.0285 \end{cases}$.

τ is the tortuosity factor accounting for the shape of the open channels in the firn. It is conveniently expressed as a function of density as (Schwander et al. 1988):

$$\frac{1}{\tau} = 1 - b \left(\frac{\rho}{\rho_i} \right)^2, \quad \rho \leq \frac{\rho_i}{\sqrt{b}} \tag{5.24}$$

where $b = 1.30$ and $\frac{1}{\tau} = 0$ for $\rho > 804.3$ kg/m^3, the effective pore-close-off density for diffusive fluxes.

The remaining part of the expression represents the isotopic fractionation in the firn between water vapor and ice assuming an isotopic equilibrium state. The number of molecules in the solid phase and in the vapor phase (using the ideal gas law) of 1 kg firn are:

$$\begin{cases} N_s = \dfrac{1}{m} N_A \\ N_v = \dfrac{pV_p}{RT} N_A \end{cases} \tag{5.25}$$

where $m = 0.018$ kg/mol is the molar mass of water[7], N_A Avogadro's number, $p \approx 37.98$

[5]The effective pore-close-off density $\rho_p = 804.3$ kg/m^3 is determined from the tortuosity factor τ. See the description of term τ in the following part of this section.

[6]The unit of [m^2/yr] is here used to keep consistent with the units of $\dot{\varepsilon}_z$ and w: [1/yr] and [m/yr], respectively. The original value for the constant in Ω_a in Hall and Pruppacher (1976) is 0.211 in unit of [cm^2/s].

[7]Usually, unit for molar mass is [g/mol]. Here [kg/mol] is used only for simplifying the note.

[Pa] the saturation vapor pressure over ice[8], T the absolute temperature [K], $R = 8.314$ [J·mol^{-1}K^{-1}] the gas constant, and $V_p = \frac{1}{\rho} - \frac{1}{\rho_i}$ [m^3] the pore space volume.

α_i is the fractionation factor for the isotopic ratios in water vapor over ice. α_{18} and α_D are given from Majoube (1971) and Melivat and Nief (1967) respectively:

$$\begin{cases} \alpha_{18} = 0.9722 \cdot e^{\frac{11.839}{T}} \\ \alpha_D = 0.9098 \cdot e^{\frac{16288}{T^2}} \end{cases} \tag{5.26}$$

which shows that α_D dominates and is highly temperature dependent, implying that the δD profile has less firn smoothing than the δ^{18}O profile. At last, the isotopic fractionation between water vapor and ice will become: $\frac{1}{\alpha_i} \cdot \frac{N_v}{N_s} = \frac{1}{\alpha_i} \cdot \frac{mp}{RT} \left(\frac{1}{\rho} - \frac{1}{\rho_i} \right)$, which forms the rest part of the expression on the right side of equation (5.22).

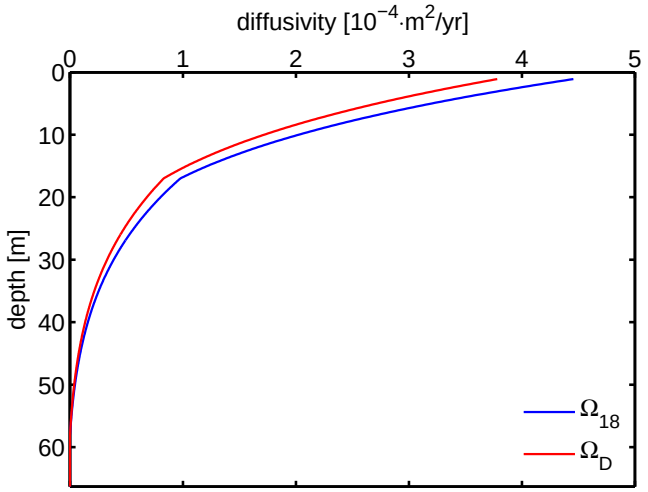

Figure 5.5: Profile of diffusivity (Ω_{18}, Ω_D) for the NEGIS firn core. Data calculated according to equation (5.22).

The profile of diffusivity (Ω_{18}, Ω_D) for the NEGIS firn core is shown in Figure 5.5. The diffusivity of $H_2^{18}O$ is larger than that of $HD^{16}O$ due to the larger value of Ω_{a18} and the smaller value of α_{18}. The diffusivity decreases with respect to depth, and rapidly drops to zero due to $\frac{1}{\tau} \to 0$ when $\rho \to 804.3$ kg/m^3, where the pores in the firn are closed off.

[8]Calculated according to Magnus' formula in Iribarne and Godson (1981):

$$\log P = 10.5553 - 2667/(T - 0.16).$$

5.1.5 Diffusion length solution

Since the data of density, vertical strain rate, and diffusivity are all obtained through the (semi-empirical) models introduced in the previous sections 5.1.1, 5.1.2, 5.1.3, and 5.1.4, the diffusion lengths down through the firn layers are ready to be acquired according to equation (5.1).

A substitution $\frac{\mathrm{d}\sigma^2}{\mathrm{d}t} = \frac{\mathrm{d}\sigma^2}{\mathrm{d}z}\frac{\mathrm{d}z}{\mathrm{d}t} = \frac{\mathrm{d}\sigma^2}{\mathrm{d}z}w$ is introduced to express equation (5.3) as:

$$\frac{\mathrm{d}\sigma^2}{\mathrm{d}z}w - 2\dot{\varepsilon}_z\sigma^2 = 2\Omega \tag{5.27}$$

In the previous sections, all the terms $w(\rho), \dot{\varepsilon}_z(\rho)$, and $\Omega(\rho)$ are derived with density ρ as the independent variable. They can be expressed as a function of depth z, since $\rho(z)$ itself is a function of depth z (equation (5.8)) by the density model of Herron and Langway (1980). Equation(5.27) is simply a first order linear differential equation expressed as:

$$\frac{\mathrm{d}\sigma^2}{\mathrm{d}z} + f(z)\sigma^2 = g(z), \qquad \begin{cases} f(z) = -\dfrac{2\dot{\varepsilon}_z(z)}{w(z)} \\ g(z) = \dfrac{2\Omega(z)}{w(z)} \end{cases} \tag{5.28}$$

According to the general solution of the first order linear differential equation, $\sigma^2(z)$ is given as:

$$\sigma^2(z) = \begin{cases} e^{-\int_0^z f(z'')\mathrm{d}z''}\left(\int_0^z g(z')e^{\int_0^z f(z'')\mathrm{d}z''}\mathrm{d}z' + C1\right), & \rho \le \rho_c \\ e^{-\int_{z_c}^z f(z'')\mathrm{d}z''}\left(\int_{z_c}^z g(z')e^{\int_{z_c}^z f(z'')\mathrm{d}z''}\mathrm{d}z' + C2\right), & \rho_c < \rho < \rho_p \\ e^{-\int_{z_p}^z f(z'')\mathrm{d}z''}\left(\int_{z_p}^z g(z')e^{\int_{z_p}^z f(z'')\mathrm{d}z''}\mathrm{d}z' + C3\right), & \rho \ge \rho_p \end{cases} \tag{5.29}$$

$$\text{with} \begin{cases} C1 = 0, \\ C2 = \sigma_c^2 = e^{-\int_0^{z_c} f(z'')\mathrm{d}z''}\int_0^{z_c} g(z')e^{\int_0^{z_c} f(z'')\mathrm{d}z''}\mathrm{d}z', \\ C3 = \sigma_p^2 = e^{-\int_{z_c}^{z_p} f(z'')\mathrm{d}z''}\left(\int_{z_c}^{z_p} g(z')e^{\int_{z_c}^{z_p} f(z'')\mathrm{d}z''}\mathrm{d}z' + \sigma_c^2\right), \end{cases}$$

where constant $C1 = 0$ is determined by the boundary condition that there is no diffusion at surface ($\sigma = 0$ for $z = 0$); $C2 = \sigma_c^2$ and $C3 = \sigma_p^2$ determined by the consistency of the diffusion lengths at the critical depth (σ_c) and the pore-close-off depth (σ_p). The diffusivity of ice Ω_{ice} will be used below the pore-close-off depth ρ_p.[9] The solution of $\sigma^2(z)$ can be obtained by numerical integration.

[9]The diffusion in the ice is not the point of the thesis. The diffusivity in the solid ice Ω_{ice} is believed to be very small and is experimentally measured by Ramseier (1967) to be $\Omega_{ice} = \Omega_0 e^{-\frac{Q}{RT}}$, where $\Omega_0 = 10$ cm^2/s and Q is the activation energy for diffusion found to be 0.62 eV.

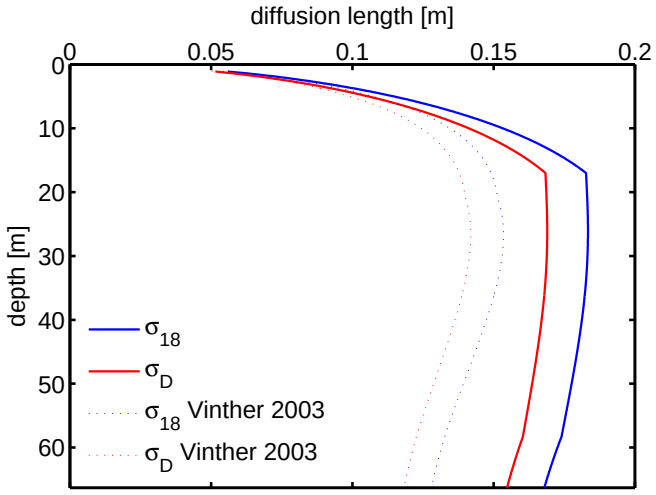

Figure 5.6: Profile of diffusion length (σ_{18}, σ_D) of the NEGIS firn core. Data calculated according to equation (5.29).

According to equation (5.3), the diffusion length is affected by two factors: the vertical velocity term $w(z)$ (reflected also on vertical strain rate $\dot{\varepsilon_z}(z)$), which accounts for the densification and ice flow; and the diffusivity term $\Omega(t)$, which accounts for the diffusive abilities in the firn pores. Diffusion length decreases as the layer goes deeper due to the layer thinning caused by densification and ice flow and also due to the decreased diffusivity which damps with respect to depth. But for the top part of the firn, where the diffusivity is still big enough and dominates the diffusion process, diffusion length increases rapidly due to the large pore space in the newly deposited snow. As the diffusivity continues damping, the decreasing effect from densification and ice flow becomes relatively larger and begins to balance the increasing effect caused by the large diffusivity. At the last stage, where the diffusivity is very small and can be neglected, diffusion length only slowly decreases corresponding to the slow densification rate and the small thinning caused by ice flow. It closes to be constant

The calculated diffusion lengths of ^{18}O and deuterium for the NEGIS firn core are shown in Figure 5.6, which shows the change of diffusion length that has been explained above. The diffusion length of ^{18}O is longer than that of deuterium due to the higher diffusivity of ^{18}O (Figure 5.5). Another approximate analytical approach has been demonstrated by Vinther (2003). Same parameters of NEGIS firn core are applied to the analytical solution and the results are plotted as an comparison. It seems the solution in this thesis somehow overestimated the diffusion lengths.

5.2 Stable isotope diffusion in the NEGIS firn core

The diffusion length can be estimated based on δ^{18}O and δD data. As indicated by the solution (equation (5.2)) of the diffusion equation, the diffusion effect can be approximated by a Gaussian filter, of which the transfer function is equal to $e^{-\frac{k^2\sigma^2}{2}}$ (Abramowitz and Stegun 1964) with $k = 2\pi f$ and σ introduced as the diffusion length. That means, the power spectra density of a diffused isotopic signal (Appendix B) will be:

$$P_s(f) = P_0 e^{-(2\pi f)^2\sigma^2} \tag{5.30}$$

where P_0 is the original power spectral density, $0 < f < \frac{1}{2\Delta x}$ the Nyquist frequency interval (only the positive half) for a sampling resolution equal to Δx.

Noise is unavoidable during all the measurements and it also affects the power spectral density. For the water isotope time series, the power spectral density of the noise can be approximated by a 1st order autoregressive model (AR-1) (Gkinis 2011):

$$P_\eta(f) = \frac{\sigma_\eta^2 \Delta x}{\left|1 - a_1 e^{-2\pi i f \Delta x}\right|^2} \tag{5.31}$$

with σ_η^2 being the variance and a_1 the coefficient of the autoregressive filter.

Thus, the total power spectral density will be represented by the sum of the power spectral density of the signal and that of the noise:

$$P(f) = P_s(f) + P_\eta(f) = P_0 e^{-k^2\sigma^2} + \frac{\sigma_\eta^2 \Delta x}{\left|1 - a_1 e^{-2\pi i f \Delta x}\right|^2} \tag{5.32}$$

The parameters $P_0, \sigma, \sigma_\eta, a_1$ can be found by fitting the model to the spectrum estimation from the MEM (Appendix A).

The diffusion length σ estimated here is the total diffusion length, which includes both in-situ firn diffusion and sampling or measuring smoothing:

$$\sigma^2 = \sigma_{firn}^2 + \sigma_{meas}^2 \tag{5.33}$$

where σ_{meas} is the smoothing effect caused by sampling for discrete measurements (σ_{dis}) or by the CFA analytical system for the continuous flow measurements (σ_{cfa}), accordingly.

$\sigma_{cfa} \approx 1.36$ cm is obtained from analyzing the stepwise response of the cfa system (Section 4.2). For the discrete sampling, σ_{dis} can be estimated as the diffusion length of a Gaussian filter which results in the same diffusion effect as a rectangular function of a window width Δ (Oppenheim et al. 1999):

$$e^{-(2\pi f)^2\sigma_{dis}^2} = \hat{\Pi}(f) = \int_{-\frac{\Delta}{2}}^{\frac{\Delta}{2}} e^{-2\pi i f t} \mathrm{d}t \tag{5.34}$$

where Δ is the resolution of the discrete sampling which determines the Nyquist frequency $f_c = \frac{1}{2\Delta}$ and $\hat{\Pi}(f)$ the Fourier transform of the rectangular function. The solution of the equation gives:

$$\sigma_{dis}^2 = \frac{2\Delta^2}{\pi^2} \log\left(\frac{\pi}{2}\right) \tag{5.35}$$

With $\Delta = 5$ cm, the diffusion length caused by discrete sampling is estimated to be $\sigma_{dis} \approx 1$ cm. Thus, the in-situ firn diffusion length σ_{firn} can be obtained by:

$$\sigma_{firn} = \sqrt{\sigma^2 - \sigma_{meas}^2} \tag{5.36}$$

It is interesting to observe that, even though the discrete samples are cut into 5 cm and all the firn/ice within this interval is totally mixed, its diffusion effect as measured by diffusion length is actually less than that of the continuous flow analytical system. That means, the discrete measurements is more accuracy, even though it samples in a lower resolution.

The diffusion lengths estimated by means of MEM spectral analysis are shown in Figure 5.7 and 5.8, according to the discrete measurements and the continuous flow measurements, respectively. The values for the diffusion lengths are estimated from the fitting of equation (5.32) to the estimated power spectrum by means of MEM. One should be reminded that the fitting is not always optimum. Several times of tuning are usually necessary. One possible shortcut is to first obtain an approximate power spectral density P_0. Once P_0 is fixed around the reasonable value, an optimum fit can be easily found. Thus, the obtained diffusion length from MEM spectra analysis can only be regarded as an general estimate.

Diffusion lengths calculated in 10 m intervals according to each measurement are compared to the models (Figure 5.9). The diffusion length of the NEGIS firn core is estimated overall at range of 10-15 cm. As shown in Figure 5.9, the diffusion length becomes comparable to the annual thickness at the depth of $\sim$10 m and from there below. That explains why it is available only for the top $\sim$8 m to use the water isotope signals for dating purpose.

In order to obtain a higher resolution of the climate signal or to help dating, the original signals are in need to be retrieved. This is typically done by a restoration of the diffused signals. The restoration is usually done by deconvolution in the spectral domain. By Fourier transformation, the isotopic signal can be transferred from the time domain to the spectral (frequency) domain. The Fourier transform of the Gaussian filter gives the transfer function (Appendix B), which illustrates the smoothing effect as a spectral filter. An optimum restoration filter can be designed to amplify the power of signal spectra as much as possible without amplifying the power of the high-frequency noise too much. By applying the restoration filter and the inverse Fourier transformation, the best possible estimate of the original isotopic profile will be obtained. The restoration is not included in this thesis. One can refer to Rasmussen et al. (2005) for an example of application.

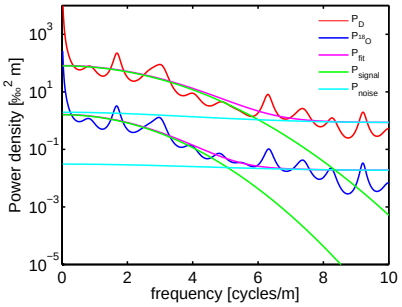

(a) NEGIS: 0-10 m, m = 30
δ^{18}O: $P_0 = 1.6, a_1 = 0.12$;
$\sigma_\eta = 0.69, \sigma_{18} \approx 6.38$ cm
δD: $P_0 = 80, a_1 = 0.2$;
$\sigma_\eta = 5, \sigma_D \approx 5.41$ cm

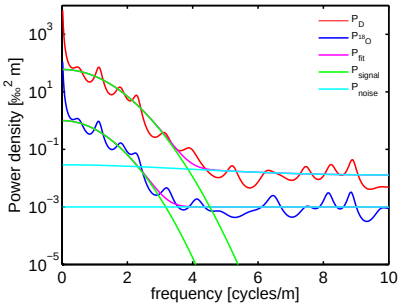

(b) NEGIS: 10-20 m, m = 30
δ^{18}O: $P_0 = 1, a_1 \approx 0$;
$\sigma_\eta = 0.14, \sigma_{18} \approx 13.15$ cm
δD: $P_0 = 60, a_1 = 0.2$;
$\sigma_\eta = 0.61, \sigma_D \approx 11.63$ cm

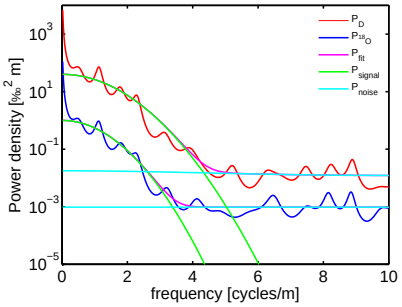

(c) NEGIS: 20-30 m, m = 30
δ^{18}O: $P_0 = 0.65, a_1 \approx 0$;
$\sigma_\eta = 0.14, \sigma_{18} \approx 12.33$ cm
δD: $P_0 = 40, a_1 = 0.09$;
$\sigma_\eta = 0.54, \sigma_D \approx 10.26$ cm

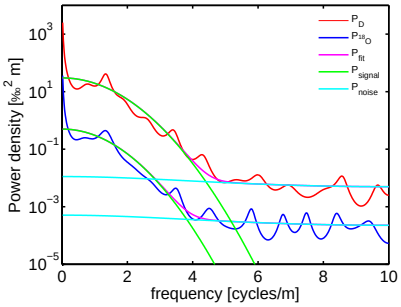

(d) NEGIS: 30-40 m, m = 30
δ^{18}O: $P_0 = 0.5, a_1 = 0.2$;
$\sigma_\eta = 0.08, \sigma_{18} \approx 11.16$ cm
δD: $P_0 = 30, a_1 = 0.2$;
$\sigma_\eta = 0.38, \sigma_D \approx 10.37$ cm

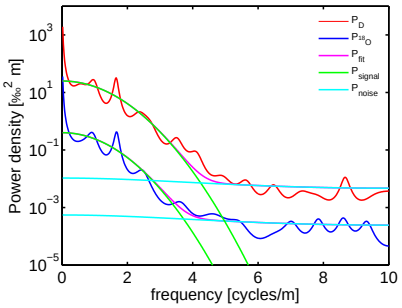

(e) NEGIS: 40-50 m, m = 30
δ^{18}O: $P_0 = 0.4, a_1 = 0.2$;
$\sigma_\eta = 0.08, \sigma_{18} \approx 11.20$ cm
δD: $P_0 = 25, a_1 = 0.2$;
$\sigma_\eta = 0.37, \sigma_D \approx 10.67$ cm

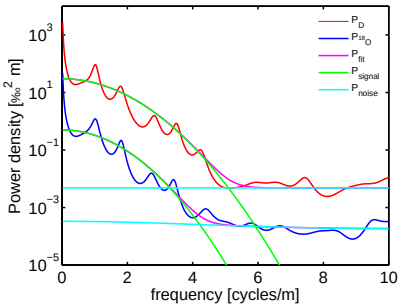

(f) NEGIS: 50-60 m, m = 30
δ^{18}O: $P_0 = 0.5, a_1 = 0.14$;
$\sigma_\eta = 0.07, \sigma_{18} \approx 10.35$ cm
δD: $P_0 = 30, a_1 \approx 0$;
$\sigma_\eta = 0.3, \sigma_D \approx 9.18$ cm

Figure 5.7: Diffusion lengths estimated from discrete measurements by fitting MEM power spectral density.

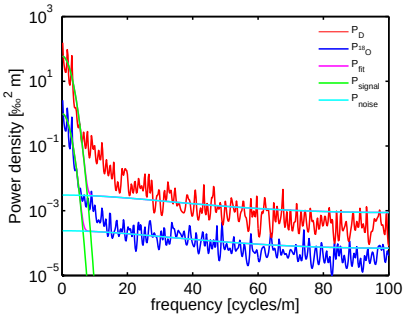

(a) NEGIS: 0-10 m, m = 200
δ^{18}O: $P_0 = 1, a_1 = 0.3$;
$\sigma_\eta = 0.15, \sigma_{18} \approx 7.04$ cm
δD: $P_0 = 60, a_1 = 0.3$;
$\sigma_\eta = 0.55, \sigma_D \approx 6.33$ cm

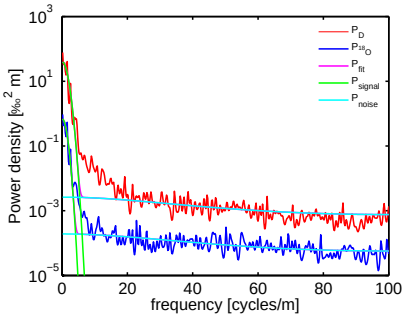

(b) NEGIS: 10-20 m, m = 200
δ^{18}O: $P_0 = 0.8, a_1 = 0.3$;
$\sigma_\eta = 0.14, \sigma_{18} \approx 10.89$ cm
δD: $P_0 = 40, a_1 = 0.3$;
$\sigma_\eta = 0.51, \sigma_D \approx 8.98$ cm

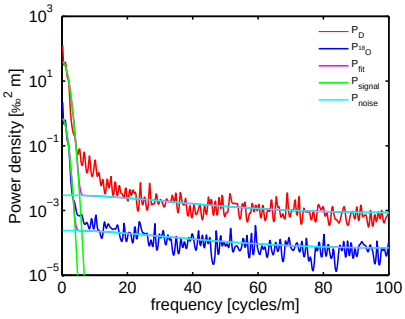

(c) NEGIS: 20-30 m, m = 200
δ^{18}O: $P_0 = 0.8, a_1 = 0.3$;
$\sigma_\eta = 0.15, \sigma_{18} \approx 11.06$ cm
δD: $P_0 = 40, a_1 = 0.3$;
$\sigma_\eta = 0.54, \sigma_D \approx 9.04$ cm

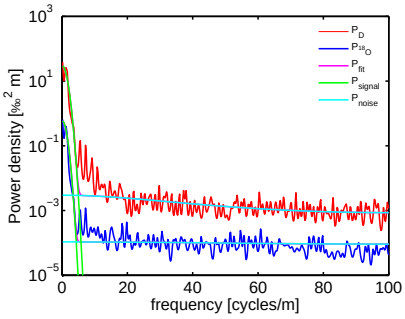

(d) NEGIS: 30-40 m, m = 200
δ^{18}O: $P_0 = 0.6, a_1 = 0.04$;
$\sigma_\eta = 0.14, \sigma_{18} \approx 10.68$ cm
δD: $P_0 = 30, a_1 = 0.3$;
$\sigma_\eta = 0.54, \sigma_D \approx 9.60$ cm

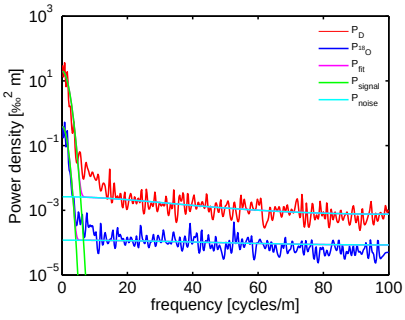

(e) NEGIS: 40-50 m, m = 200
δ^{18}O: $P_0 = 0.4, a_1 = 0.08$;
$\sigma_\eta = 0.14, \sigma_{18} \approx 10.65$ cm
δD: $P_0 = 20, a_1 = 0.3$;
$\sigma_\eta = 0.5, \sigma_D \approx 8.31$ cm

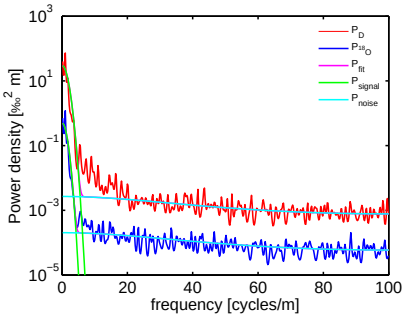

(f) NEGIS: 50-60 m, m = 200
δ^{18}O: $P_0 = 0.5, a_1 = 0.3$;
$\sigma_\eta = 0.14, \sigma_{18} \approx 10.27$ cm
δD: $P_0 = 30, a_1 = 0.3$;
$\sigma_\eta = 0.51, \sigma_D \approx 8.66$ cm

Figure 5.8: Diffusion lengths estimated from continuous flow measurements by fitting MEM power spectral density.

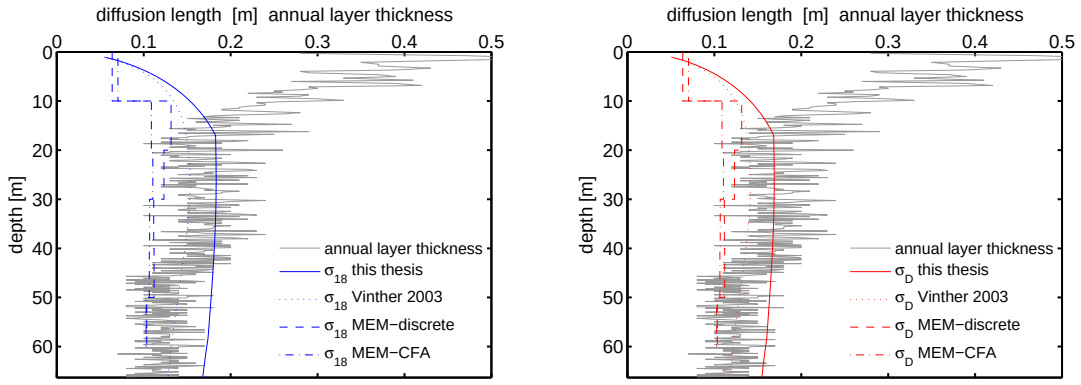

Figure 5.9: Calculated and MEM estimated diffusion length profiles (σ_{18}, σ_D) of the NEGIS firn core. Annual layer thicknesses are also presented.

Chapter 6

Discussion and Conclusions

This thesis has presented both continuous flow and discrete measurements of the water isotopes in the NEGIS firn core, with a main purpose to compare the quality of the results from continuous flow approach with that of the discrete samples. The discrete approach has long been a typical way of measuring firn/ice core water isotopes. However, there is always compromise between a desired resolution and the accomplishing time, since both the preparation and measurements of the discrete samples demand elaborate labor work. A development of the continuous melting system has made an on-line analysis of the firn/ice core available. In addition to the efficient time-saving, it also provides an opportunity to obtain higher resolution signals. At the same time, the precision, exact resolution, and the results reliability of this new approach needs to be demonstrated with comparison of the discrete one. A 66.3 m long firn core drilled from Northeast Greenland has provided such a chance to do the comparison through the whole firn records.

The discrete measurements have been carried out in the typical 5 cm resolution, with samples being measured on a NIR Cavity Ring-Down spectrometer. The water concentration level in the cavity is kept in an optimum range. Results have been calibrated with respect to the VSMOW standard water. For the discrete measurements, the calibration is performed each time the spectrometer conducts a measurement run, which typically consists of 39 samples. That means, the whole firn core has been calibrated about every 2 meters of measurement. In this way, the effect of the instrumental drifts will be negligible after duly calibrations.

The continuous flow measurements have been performed by coupling a NIR Cavity Ring-Down spectrometer with the continuous melting system (CFA). Due to the more unstable conditions, the water concentration level in the cavity needs to be calibrated for the continuous flow measurements. The final results are reported with respect to VSMOW scale as well. However, only two times of calibration are available for the 28 days of continuous flow measurements. In this case, the lack of frequent calibrations may induce an error caused by the instrumental drifts. This is confirmed in the comparison with the discrete measurements, where an discrepancy arises after a long term of measuring.

Because background water is used between the shifts of the consecutive core samples, the useful isotope signals need to be extracted. An automatic method combining with visual inspection is developed. Another critical processing is to generate the depth scale. The time and length of the melting recorded by an optical encoder as well as the cutting records during preparing the core samples are combined to accomplish this procedure. Both the extractions and the calculated depth scale are verified to be reliable by comparing with the discrete measurements.

The precision and resolution of the continuous flow measurements are quantified and compared to that of the discrete measurements. Precision is estimated as the noise level of the measurements by means of spectral methods. The uncertainty of the continuous flow measurements is evaluated to be about 0.07% and 0.25% for δ^{18}O and δ D, respectively. It is comparable to the precision of the discrete measurements, which is determined to be better than 0.05% (δ^{18}O) and 0.23% (δ D).

The resolution of the continuous flow measurements are estimated based on the isotopic signal step at the switch between each firn core samples and the background water. The smoothing effect of the CFA analytial system can be expressed as an Gaussian filter with a diffusion length of at least 1.36 cm. It is higher than the smoothing effect caused by the 5 cm discrete sampling, which is approximate to the effect of an Gaussian filter with a diffusion length of 1 cm. That is to say, the continuous flow measurements have a higher resolution but based on a slightly more diffused signal. The discrete measurements have a lower resolution but the results of the sampling points are a bit more accurate.

Regardless of the drift effects, which can be most reduced by duly calibrations during the measurements, results of the continuous flow measurements show a good agreement with the discrete measurements. The precision is at a comparable level and the resolution is much higher ($\sim$5 mm for NEGIS, depending on the melting speed). Given that the continuous flow measurements are time-saving, low power consumption and allow multiple analysis on the same sample, it has great potential in the firn/ice core studies.

The high resolution obtained by the continuous flow approach can be useful for reconstructions of climate change in the past. However, both the natural diffusion process imposed in the snow and firn layers of the ice sheet and the smoothing effects during the measurements will limit the available resolution. The study of a firn diffusion model developed by Johnsen (1977, 2000) is carried out in the last part of the thesis to address the diffusion process in the NEGIS firn core. The diffusion length in the NEGIS firn layers is estimated to be at a range of 10-15 cm. Due to the low accumulation rate in the Northeast Greenland, the annual signals of the water isotopes are strongly attenuated and are recognizable only for the top $\sim$ 8m.

Appendix A

Maximum Entropy Method

The Maximum Entropy Method (MEM) is developed by Burg (1975). The power spectral density estimator is given by:

$$P(f) = \frac{P_m \Delta t}{\left| 1 - \sum_{n=1}^{m} a_{mn} e^{-2\pi i f n \Delta t} \right|^2} \tag{A.1}$$

The time series is sampled at a uniform period of Δt, the frequency f is limited to the Nyquist fold-over frequency, $\frac{-1}{2\Delta t} \leq f \leq \frac{1}{2\Delta t}$. P_m is the output power of the $m+1$ long prediction error filter $(1, -a_{m1}, -a_{m2}, \cdots, -a_{mm})$.

MEM can be seen as a sophisticated procedure to estimate parameters for an autoregressive (AR) model (Vinther 2003). For a time series of length M, the model tries to use the m preceding values weighted by m parameters $(-a_{m1}, -a_{m2}, \cdots, -a_{mm})$ to predict the given value in the series. This will define a mean forward prediction error for the $M-m$ long values in the series as:

$$\frac{1}{M-m} \sum_{t=1}^{M-m} \left(x_{t+m} - \sum_{n=1}^{m} a_{mn} x_{t+m-n} \right) \tag{A.2}$$

The same procedure should also be applied to the series backwards, which will correspondingly define a mean backward prediction error. The averaged prediction error will be given as:

$$\frac{1}{2(M-m)} \sum_{t=1}^{M-m} \left[\left(x_{t+m} - \sum_{n=1}^{m} a_{mn} x_{t+m-n} \right) + \left(x_t - \sum_{n=1}^{m} a_{mn} x_{t+n} \right) \right] \tag{A.3}$$

By minimizing this averaged prediction error, the parameters a_{mn} of $m+1$ long prediction error filter can be determined.

Then equation (A.1) can be applied to calculate the power spectrum of the time series. Given a certain frequency f, along the change of n, $e^{-2\pi i f n \Delta t}$ will generate a series of waves with different dominating frequencies. On the other hand, by minimizing the averaged prediction error, the parameters a_{mn} have at the same time captured the variance

informations from the time series. $\sum_{n=1}^{m} a_{mn} e^{-2\pi i f n \Delta t}$ will somehow be close to 1 when these two variations are relatively in phase and thus yields a peak power density $P(f)$ for the corresponding frequency (Vinther B. M., personal communication, 2014).

m is the order of the AR model, and it shows that the power spectrum is able to resolve more and more details by increasing m while it turns to be more and more smooth by decreasing m.

Appendix B

Transfer Function

The transfer function of the Gaussian type filter will be given by its Fourier transform, which is itself a Gaussian function and is equal to (Abramowitz and Stegun 1964):

$$\hat{G}(f) = \int_{-\infty}^{\infty} \frac{1}{\sigma\sqrt{2\pi}} e^{-\frac{t^2}{2\sigma^2}} e^{-2\pi i f t} \mathrm{d}t = e^{-\frac{k^2\sigma^2}{2}} \tag{B.1}$$

where $k = 2\pi f$ is the wavenumber.

The magnitude of the transfer function describes how the amplitude of a periodic input signal of wavenumber k is damped when analyzed by the system. A cycle with an initial amplitude A_0 will be damped to a final amplitude A, which is equal to:

$$A = A_0 e^{-\frac{k^2\sigma^2}{2}} \tag{B.2}$$

Since the power of a wave is proportional to the square of its amplitude, $P \propto A^2$, the attenuation of power spectral density of the signals will be described as:

$$P = P_0 e^{-k^2\sigma^2} \tag{B.3}$$

where P and P_0 are the final and initial power spectral density for a cycle of wavenumber k, respectively.

The smoothing filter of the CFA system is a Gaussian type filter as described in equation (4.6), where the diffusion length term is σ_{cfa}. Considering the nature of the diffusion can be generally represented by a Gaussian function, the same deviation above will be valid for the smoothing filter of the in-situ diffusion (σ_{firn}), and thus the total smoothing filter for the on-line CFA analysis (σ_{on}) and off-line discrete analysis (σ_{off}).

Bibliography

Abramowitz, M. and Stegun, I. A. (1964). *Handbook of Mathematical Functions with Formulas, Graphs, and Mathematical Tables*. Dover, New York, ninth dover printing, tenth gpo printing edition.

Allan, D. W. (1966). Statistics of atomic frequency standards. *Proceedings of the IEEE*, 54(2):221–230.

Andersen, K., Ditlevsen, P., and Steffensen, J. (2001). Ice cores and palaeoclimate.

Andersen, N. (1974). Calculation of filter coefficients for maximum entropy spectral analysis. *Geophysics*, 39(1):69–72.

Bales, R. C., Guo, Q., Shen, D., McConnell, J. R., Du, G., Burkhart, J. F., Spikes, V. B., Hanna, E., and Cappelen, J. (2009). Annual accumulation for greenland updated using ice core data developed during 2000-2006 and analysis of daily coastal meteorological data. *Journal of Geophysical Research-atmospheres*, 114:D06116.

Bales, R. C., McConnell, J. R., Mosley-Thompson, E., and Csatho, B. (2001). Accumulation over the greenland ice sheet from historical and recent records. *J. Geophys. Res.*, 106(D24):33813–33825.

Begley, I. S. and Scrimgeour, C. M. (1997). High-precision δ^2H and δ^{18}O measurement for water and volatile organic compounds by continuous-flow pyrolysis isotope ratio mass spectrometry. *Analytical Chemistry*, 69(8):1530–1535.

Bigeleisen, J., Perlman, M. L., and Prosser, H. C. (1952). Conversion of hydrogenic materials to hydrogen for isotopic analysis. *Analytical Chemistry*, 24(8):1356–1357.

Bigler, M., Svensson, A., Kettner, E., Vallelonga, P., Nielsen, M. E., and Steffensen, J. P. (2011). Optimization of high-resolution continuous flow analysis for transient climate signals in ice cores. *Environmental Science & Technology*, 45(10):4483–4489.

Brand, W. A., Geilmann, H., Crosson, E. R., and Rella, C. W. (2009). Cavity ring-down spectroscopy versus high-temperature conversion isotope ratio mass spectrometry; a case study on δ^2H and δ^{18}O of pure water samples and alcohol/water mixtures. *Rapid Communications in Mass Spectrometry*, 23(12):1879–1884.

Burg, J. P. (1975). *Maximum entropy spectral analysis*. PhD thesis, Stanford University.

Busenberg, E. and Langway, C. C. (1979). Levels of ammonium, sulfate, chloride, calcium, and sodium in snow and ice from southern greenland. *J. Geophys. Res.*, 84(C4):1705–1709.

Chappellaz, J., Stowasser, C., Blunier, T., Baslev-Clausen, D., Brook, E. J., Dallmayr, R., Faïn, X., Lee, J. E., Mitchell, L. E., Pascual, O., Romanini, D., Rosen, J., and Schüpbach, S. (2013). High-resolution glacial and deglacial record of atmospheric methane by continuous-flow and laser spectrometer analysis along the neem ice core. *Climate of the Past*, 9(6):2579–2593.

Clark, I. D. and Fritz, P. (1997). *Environmental isotopes in hydrogeology*. CRC press.

Clausen, H., Gundestrup, N., Johnsen, S., Bindschadler, R., and Zwally, J. (1988). Glaciological investigations in the crete area, central greenland: A search for a new deep-drilling site. *Ann. Glaciol*, 10:10–15.

Clausen, H. and Hammer, C. (1988). The laki and tambora eruptions as revealed in greenland ice cores from 11 locations. *Ann. Glaciol*, 10:16–22.

Craig, H. (1961). Isotopic variations in meteoric waters. *Science*, 133(3465):1702–1703.

Crosson, E. R. (2008). A cavity ring-down analyzer for measuring atmospheric levels of methane, carbon dioxide, and water vapor. *Applied Physics B-Lasers And Optics*, 92(3):403–408.

Cuffey, K. and Steig, E. (1998). Isotopic diffusion in polar firn: implications for interpretation of seasonal climate parameters in ice-core records, with emphasis on central greenland. *Journal of Glaciology*, 44(147):273–284.

Dansgaard, W. (1953). The abundance of o18 in atmospheric water and water vapour. *Tellus*, 5(4):461–469.

Dansgaard, W. (1954). The o18-abundance in fresh water. *Geochimica et Cosmochimica Acta*, 6(5-6):241–260.

Dansgaard, W. (1964). Stable isotopes in precipitation. *Tellus*, 16(4):436–468.

Dansgaard, W., Clausen, H., Gundestrup, N., Hammer, C., Johnsen, S., Kristinsdottir, P., and Reeh, N. (1982). A new greenland deep ice core. *Science*, 218(4579):1273–1277.

Dansgaard, W., Johnsen, S., Clausen, H., Dahl-Jensen, D., Gundestrup, N., Hammer, C., Hvidberg, C., Steffensen, J., Sveinbjornsdottir, A., and Jouzel, J. (1993). Evidence for general instability of past climate from a 250-kyr ice-core record. *Nature*, 364(6434):218–220.

Dansgaard, W. and Johnsen, S. J. (1969). A flow model and a time scale for the ice core from camp century, greenland. *Journal of Glaciology*, 8(53):215–223.

Epstein, S. Mayeda, T. (1953). Variations of ^{18}O content of waters from natural sources. *Geochimica Cosmochimica Acta*, 4:213–224.

Fahnestock, M., Bindschadler, R., Kwok, R., and Jezek, K. (1993). Greenland ice sheet surface properties and ice dynamics from ERS-1 SAR imagery. *Science*, 262(5139):1530–1534.

Fahnestock, M., Joughin, I., Scambos, T., Kwok, R., Krabill, W., and Gogineni, S. (2001). Ice-stream-related patterns of ice flow in the interior of northeast greenland. *Journal of Geophysical Research: Atmospheres (1984-2012)*, 106(D24):34035–34045.

Fuhrer, K., Neftel, A., Anklin, M., Staffelbach, T., and Legrand, M. (1996). High-resolution ammonium ice core record covering a complete glacial-interglacial cycle. *J. Geophys. Res.*, 101(D2):4147–4164.

Gehre, M., Geilmann, H., Richter, J., Werner, R. A., and Brand, W. A. (2004). Continuous flow h-2/h-1 and and(18)o/o-16 analysis of water samples with dual inlet precision. *Rapid Communications In Mass Spectrometry*, 18(22):2650–2660.

Gehre, M., Hoefling, R., Kowski, P., and Strauch, G. (1996). Sample preparation device for quantitative hydrogen isotope analysis using chromium metal. *Analytical Chemistry*, 68(24):4414–4417.

Gkinis, V. (2011). *High resolution water isotope data from ice cores*. PhD thesis, Niels Bohr Institute, University of Copenhagen.

Gkinis, V., Popp, T. J., Blunier, T., Bigler, M., Schupbach, S., Kettner, E., and Johnsen, S. J. (2011). Water isotopic ratios from a continuously melted ice core sample. *Atmospheric Measurement Techniques*, 4(11):2531–2542.

Gkinis, V., Popp, T. J., Johnsen, S. J., and Blunier, T. (2010). A continuous stream flash evaporator for the calibration of an ir cavity ring-down spectrometer for the isotopic analysis of water. *Isotopes In Environmental and Health Studies*, 46(4):463–475.

GRIP members (1993). Climate instability during the last interglacial period recorded in the GRIP ice core. *Nature*, 364(6434):203–207.

Grootes, P. and Stuiver, M. (1993). Comparison of oxygen isotope records from GISP2 and GRIP Greenland ice cores. *Nature: International weekly journal of science*, 366(6455):552–554.

Gupta, P., Noone, D., Galewsky, J., Sweeney, C., and Vaughn, B. H. (2009). Demonstration of high-precision continuous measurements of water vapor isotopologues in laboratory and remote field deployments using wavelength-scanned cavity ring-down spectroscopy

(ws-crds) technology. *Rapid Communications In Mass Spectrometry*, 23(16):2534–2542.

Hall, W. D. and Pruppacher, H. R. (1976). Survival of ice particles falling from cirrus clouds in subsaturated air. *Journal of the Atmospheric Sciences*, 33(10):1995–2006.

Hammer, C. (1980). Acidity of polar ice cores in relation to absolute dating, past volcanism, and radio-echoes. *Journal of Glaciology*, 25(93):359–372.

Herron, M. M. and Langway, C. C. (1980). Firn densification - an empirical-model. *Journal Of Glaciology*, 25(93):373–385.

Iannone, R. Q., Kassi, S., Jost, H.-J., Chenevier, M., Romanini, D., Meijer, H. A. J., Dhaniyala, S., Snels, M., and Kerstel, E. R. T. (2009). Development and airborne operation of a compact water isotope ratio infrared spectrometer. *Isotopes in Environmental and Health Studies*, pages –.

Iribarne, J. and Godson, W. (1981). *Atmospheric Thermodynamics*. Springer.

Johnsen, S. J. (1977). Stable isotope homogenization of polar firn and ice. *Isotopes and impurities in snow and ice*, pages 210–219.

Johnsen, S. J., Clausen, H. B., Cuffey, K. M., Hoffmann, G., Schwander, J., and Creyts, T. (2000). Diffusion of stable isotopes in polar firn and ice. the isotope effect in firn diffusion. In Hondoh, T., editor, *Physics of Ice Core Records*, pages 121–140, Sapporo. Hokkaido University Press.

Johnsen, S. J., Clausen, H. B., Jouzel, J., Schwander, J., Sveinbjornsdottir, A. E., and White, J. (1999). Stable isotope records from greenland deep ice cores: The climate signal and the role of diffusion. *Ice Physics and the Natural Environment*, 56:NATO, Adv Res Inst.

Johnsen, S. J., Dansgaard, W., Clausen, H. B., and Langway, C. C. (1972). Oxygen isotope profiles through the antarctic and greenland ice sheets. *Nature*, 235(5339):429–434.

Johnsen, S. J., Dansgaard, W., and White, J. W. C. (1989). The origin of arctic precipitation under present and glacial conditions. *Tellus*, 41B:452–468.

Joughin, I., Fahnestock, M., MacAyeal, D., Bamber, J. L., and Gogineni, P. (2001). Observation and analysis of ice flow in the largest Greenland ice stream. *J. Geophys. Res.*, 106(D24):34021–34034.

Joughin, I., Smith, B. E., and Holland, D. M. (2010). Sensitivity of 21st century sea level to ocean-induced thinning of pine island glacier, antarctica. *Geophys. Res. Lett.*, 37(20):L20502–.

Kaufmann, P. R., Federer, U., Hutterli, M. A., Bigler, M., Schüpbach, S., Ruth, U., Schmitt, J., and Stocker, T. F. (2008). An improved continuous flow analysis system for high-resolution field measurements on ice cores. *Environmental Science & Technology*, 42(21):8044–8050.

Kerstel, E. R. T., Iannone, R. Q., Chenevier, M., Kassi, S., Jost, H. J., and Romanini, D. (2006). A water isotope (^{2}H,^{17} O,^{18} O) spectrometer based on optical feedback cavity-enhanced absorption for in situ airborne applications. *Applied Physics B-Lasers And Optics*, 85(2-3):397–406.

Kerstel, E. R. T., van der Wel, L. G., and Meijer, H. A. J. (2005). First real-time measurement of the evolving h-2/h-1 ratio during water evaporation from plant leaves. *Isotopes In Environmental And Health Studies*, 41(3):207–216.

Kerstel, E. R. T., van Trigt, R., Dam, N., Reuss, J., and Meijer, H. A. J. (1999). Simultaneous determination of the ^{2}H/^{1}H, ^{17}O/^{16}O and ^{18}O/^{16}O isotope abundance ratios in water by means of laser spectrometry. *Analytical Chemistry*, 71(23):5297–5303.

Kjær, H. A., Vallelonga, P., Svensson, A., Kristensen, M. E. L., Tibuleac, C., and Bigler, M. (2013). Continuous flow analysis method for determination of dissolved reactive phosphorus in ice cores. *Environmental science & technology*, 47(21):12325–12332.

Langway, C. C., J., Oeschger, H., and Dansgaard, W., J. (1985). The greenland ice sheet program in perspective. In *Geophys. Monogr. Ser.*, volume 33, pages 1–8. AGU, Washington, DC.

Majoube, M. (1971). Fractionation in o-18 between ice and water vapor. *Journal De Chimie Physique Et De Physico-Chimie Biologique*, 68(4):625–&.

Melivat, L. and Nief, G. (1967). Fractionnement isotopique lors des changements detat solide-vapeur et liquide-vapeur de leau a des temperatures inferieures a 0 degrees c. *Tellus*, 19(1):122–&.

Merlivat, L. and Jouzel, J. (1979). Global climatic interpretation of the deuterium-oxygen 18 relationship for precipitation. *J. Geophys. Res.*, 84(C8):5029–5033.

Moore, J. and Maeno, N. (1991). Application of the dielectric profiling technique to ice core studies. *Proceedings of the NIPR Symposium on Polar Meteorology and Glaciology*, 4:81–92.

Moore, J. and Paren, J. (1987). A new technique for dielectric logging of antarctic ice cores. *Le Journal de Physique Colloques*, 48(C1):C1–155.

NEEM members (2013). Eemian interglacial reconstructed from a greenland folded ice core. *Nature*, 493(7433):489–494.

NGRIP members (2004). High-resolution record of northern hemisphere climate extending into the last interglacial period. *Nature*, 431(7005):147–151.

Nye, J. F. (1963). Correction factor for accumulation measured by the thickness of the annual layers in an ice sheet. *Journal of Glaciology*, 4:785–788.

Oppenheim, A. V., Schafer, R. W., and Buck, J. R. (1999). Discrete time signal processing.

Petrunin, A., Rogozhina, I., Vaughan, A. P. M., Kukkonen, I. T., Kaban, M., Koulakov, I., and Thomas, M. (2013). Heat flux variations beneath central greenland's ice due to anomalously thin lithosphere. *Nature Geoscience*, 6:746–750.

Ramseier, R. O. (1967). Self-diffusion of tritium in natural and synthetic ice monocrystals. *Journal Of Applied Physics*, 38(6):2553–&.

Rasmussen, S. (2006). *Improvement, Dating and Analysis of Greenland Ice Core Stratigraphies*. PhD thesis, Niels Borh Institute, University of Copenhagen.

Rasmussen, S. O., Andersen, K. K., Johnsen, S. J., Bigler, M., and McCormack, T. (2005). Deconvolution-based resolution enhancement of chemical ice core records obtained by continuous flow analysis. *Journal Of Geophysical Research-Atmospheres*, 110(D17):doi:10.1029/2004JD005717.

Reeh, N., S. Johnsen, J., and Dahl-Jensen, D. (1985). Dating the dye 3 deep ice core by flow model calculations. In *Greenland Ice Cores: Geophysics, Geochemistry and the Environment*, volume 33 of *Geophysical Monograph*, pages 57–65.

Röthlisberger, R., Bigler, M., Hutterli, M., Sommer, S., Stauffer, B., Junghans, H. G., and Wagenbach, D. (2000). Technique for continuous high-resolution analysis of trace substances in firn and ice cores. *Environmental Science & Technology*, 34(2):338–342.

Schüpbach, S., Federer, U., Kaufmann, P. R., Hutterli, M. A., Buiron, D., Blunier, T., Fischer, H., and Stocker, T. F. (2009). A new method for high-resolution methane measurements on polar ice cores using continuous flow analysis. *Environmental Science & Technology*, 43(14):5371–5376.

Schwander, J., Stauffer, B., and Sigg, A. (1988). Air mixing in firn and the age of air at pore close-off. *Annals Of Glaciology*, 10:141–145.

Schytt, V. (1958). *The inner structure of the ice shelf at Maudheim as shown by core drilling*. Norsk Polarinstitutt.

Sigg, A., Fuhrer, K., Anklin, M., Staffelbach, T., and Zurmuhle, D. (1994). A continuous analysis technique for trace species in ice cores. *Environmental Science & Technology*, 28(2):204–209.

Stowasser, C., Buizert, C., Gkinis, V., Chappellaz, J., Schüpbach, S., Bigler, M., Faïn, X., Sperlich, P., Baumgartner, M., Schilt, A., and Blunier, T. (2012). Continuous measurements of methane mixing ratios from ice cores. *Atmospheric Measurement Techniques*, 5(5):999–1013.

Svensson, A., Biscaye, P. E., and Grousset, F. E. (2000). Characterization of late glacial continental dust in the greenland ice core project ice core. *J. Geophys. Res.*, 105(D4):4637–4656.

Vallelonga, P., Christianson, K., Alley, R. B., Anandakrishnan, S., Christian, J. E. M., Dahl-Jensen, D., Gkinis, V., Holme, C., Jacobel, R. W., Karlsson, N., Keisling, B. A., Kipfstuhl, S., Kjær, H. A., Kristensen, M. E. L., Muto, A., Peters, L. E., Popp, T., Riverman, K. L., Svensson, A. M., Tibuleac, C., Vinther, B. M., Weng, Y., and Winstrup, M. (2014). Initial results from geophysical surveys and shallow coring of the northeast greenland ice stream (negis). *The Cryosphere Discussions*, 8(1):691–719.

van den Broeke, M., Bamber, J., Ettema, J., Rignot, E., Schrama, E., van de Berg, W. J., van Meijgaard, E., Velicogna, I., and Wouters, B. (2009). Partitioning recent greenland mass loss. *science*, 326(5955):984–986.

Vinther, B. M. (2003). Seasonal δ^{18}O signals in greenland ice cores. Master's thesis, Center for Ice and Climate, NBI, University of Copenhagen.

Werle, P. (2011). Accuracy and precision of laser spectrometers for trace gas sensing in the presence of optical fringes and atmospheric turbulence. *Applied Physics B-lasers and Optics*, 102(2):313–329.

Whillans, I. and Grootes, P. (1985). Isotopic diffusion in cold snow and firn. *Journal of Geophysical Research*, 90:3910–3918.